Title: Type 1 interferon perturbates clonal competition by reshaping human blood development

Authors: Chhiring Lama[1#], Danielle Isakov[1,2#], Shira Rosenberg[1], Miguel Quijada-Álamo[3], Mirca S. Saurty-Seerunghen[1], Sara Moein[1], Tsega-Ab Abera[1], Olivia Sakaguchi[1], Mansi Totwani[1], Grace Freed[3], Chi-Lam Poon[4], Neelang Parghi[1], Andrea Kubas-Meyer[1], Amy X. Xie[5,6], Mohamed Omar[1], Daniel Choi[7], Franco Castillo-Tokumori[7], Ghaith Abu-Zeinah[7], Alicia Dillard[1], Nathaniel D. Omans[7,8,9], Neville Dusaj[2,7,8], Paulina Chamely[7,8], Eleni Mimitou[10], Peter Smibert[11], Heidi E. Kosiorek[12], Amylou C. Dueck[13], Rona Weinberg[14], Ronan Chaligne[6], Bridget Marcellino[16], Luigi Marchionni[1], Sanjay Patel[1], Paul Simonson[1], Dan A. Landau[7,8,9], Elvin Wagenblast[3], Ronald Hoffman[15,16‡], Anna S. Nam[1,5,9‡*]

Affiliations:

[1]Department of Pathology and Laboratory Medicine, Weill Cornell Medicine; New York, NY, USA.
[2]Tri-Institutional MD-PhD Program, Weill Cornell Medicine, Rockefeller University, Memorial Sloan Kettering Cancer Center; New York, NY, USA.
[3]Department of Oncological Sciences, Icahn School of Medicine at Mount Sinai; New York, NY, USA
[4]Department of Physiology, Biophysics & Systems Biology, Weill Cornell Medicine; New York, NY, USA.
[5]Biochemistry, Structural Biology, Cell Biology, Developmental Biology and Molecular Biology Graduate Programs, Weill Cornell Medicine; New York, NY, USA.
[6]Computational Oncology Service, Memorial Sloan Kettering Cancer Center; New York, NY, USA.
[7]Division of Hematology and Medical Oncology, Department of Medicine and Meyer Cancer Center, Weill Cornell Medicine; New York, NY, USA.
[8]New York Genome Center; New York, NY, USA.
[9]Tri-Institutional Training Program in Computational Biology and Medicine, Memorial Sloan Kettering Cancer Center, Cornell University, Weill Cornell Medicine, New York, NY, USA.
[10]Immunai; New York, NY, USA.
[11]10x Genomics; Pleasanton, CA, USA.
[12]Department of Biostatistics, Mayo Clinic Arizona; Scottsdale, AZ, USA.
[13]Department of Quantitative Health Sciences and Alliance Statistics and Data Management Center, Mayo Clinic, Rochester, MN, USA.
[14]New York Blood Center; New York, NY, USA.
[15]Myeloproliferative Neoplasms Research Consortium; New York, NY, USA.
[16]Tisch Cancer Institute, Icahn School of Medicine at Mount Sinai; New York, NY, USA.

[#]Authors contributed equally to the work
[‡]Jointly supervised this work
*Corresponding author. Email: shn9035@med.cornell.edu

Abstract

Inflammation perturbs evolutionary dynamics of hematopoietic stem cell (HSC) clones in clonal hematopoiesis and myeloid neoplasms. We studied HSCs, progenitors and immune cells from patients with myeloproliferative neoplasm (MPN) at baseline and following interferon-α (IFNα) treatment, the only MPN therapy to deplete clonal stem cells. We focused on essential thrombocythemia, an informative model of early-phase neoplastic hematopoiesis. We integrated somatic genotyping, transcriptomes, immunophenotyping, and chromatin accessibility across single cells. IFNα simultaneously activated HSCs into two polarized states, a lymphoid progenitor expansion associated with an anti-inflammatory state and an IFNα-specific inflammatory granulocytic progenitor (IGP) state derived directly from HSCs. The augmented lymphoid differentiation balanced the typical MPN-induced myeloid bias, associated with normalized blood counts. Clonal fitness upon IFNα exposure was due to resistance of clonal stem cells to differentiate into IGPs. These results support a paradigm wherein inflammation perturbs clonal dynamics by HSC induction into the precipitous IGP differentiation program.

58 **One-Sentence Summary**

59 Inflammation accelerates clonal evolution by driving stem cell differentiation into an alternate
60 interferon-α-induced progenitor state.

61

Introduction

Systemic inflammation increases with aging and is implicated in accelerating the development of clonal hematopoiesis (CH) and myeloid neoplasms (*1-8*). Clonal stem cells may be resistant to inflammatory signaling that leads to functional defects in hematopoietic stem cells (HSC) (*4, 6-8*). On the other hand, inflammatory cytokines, such as interferon-α (IFNα), directly activate HSCs into cell cycle entry in mice (*9-11*), an observation that has been proposed to undergird both enhanced clonal expansion upon inflammation (*5*) and clonal depletion in the setting of IFNα therapy for myeloproliferative neoplasms (MPN) (*9, 12, 13*). Indeed, the ability of IFNα to modulate clonal dynamics in patients with MPN presents a unique opportunity to assess the effects of chronic IFNα signaling on clonal HSC fitness in human.

MPNs are driven by somatic mutations in *CALR*, *JAK2* or *MPL* that override the highly regulated process of hematopoiesis resulting in an overproduction of one or more myeloid lineages, such as increased platelet production in essential thrombocythemia (ET) (*14*). IFNα is the only clonally selective MPN treatment, often effecting molecular response (*12, 13, 15*). Even in the absence of molecular response, IFNα treatment frequently induces normalization of the patients' blood counts (*12, 13, 15*). To define the downstream effects of IFNα therapy that undergird the phenotypic response and clonal dynamics in human, we require methods that can isolate the differential IFNα effects on mutated stem cells from the wildtype. However, as clonal cells cannot be distinguished from the admixed wildtype cells via cell surface markers, we leveraged single-cell multi-omics platforms that detect the mutational status and whole transcriptomes (*16*) with immunophenotyping or chromatin accessibility data, within thousands of individual cells. These methods allowed us to overlay two hematopoietic differentiation landscapes—one mutated and the other wildtype—from the same individual, thus facilitating a direct comparison between mutated and wildtype cells both at baseline and following treatment. We focused on *CALR*-mutated ET due to the heterogeneous molecular response despite clinical response in most patients (*13, 17*) and applied these multi-modality single-cell methods to $CD34^+$ hematopoietic stem and progenitor cells (HSPC) and immune cells from serial bone marrow sampling from patients treated with IFNα for at least one year. This approach enabled us to assess the phenotypic and epigenetic alterations, jointly together with clonal dynamics, induced by IFNα in human neoplasm.

Results

IFNα paves an alternate route of granulocytic differentiation

To define the effects of IFNα on wildtype and neoplastic hematopoiesis in human, we leveraged the Genotyping of Transcriptomes (GoT) technology that simultaneously captures the mutation status and whole transcriptomes in thousands of single cells (*16*). To overcome inter-patient variability in baseline hematopoiesis, we applied GoT to FACS-isolated $CD34^+$ cells from serial (i.e., baseline and treated) bone marrow from individuals who were diagnosed with *CALR*-mutated ET (*18*) (**Fig. 1A**). As serial bone marrow biopsies are not typically performed in the absence of suspected disease progression, we utilized cryopreserved specimens from the MPN-RC-111 and -112 clinical trials wherein patients were treated weekly with a pegylated form of IFNα (*19, 20*) (**Fig. 1A**, n = 10 individuals, 8 baseline samples, 13 treated samples; additional 3 baseline samples included from our previous work (*16*); see **table S1** for patient and sample information). Patients with samples available for this study exhibited partial or complete clinical response (i.e.,

104 improvement in platelet counts) and were representative of the other patients with *CALR* mutations
105 in these clinical trials (**fig. S1A**, **table S1**). We incorporated time-point specifying barcoded
106 antibodies (*21*) that enabled multiplexing baseline and IFNα-treated samples into the same GoT
107 experiments, in order to obviate technical batch effects (e.g., sequencing depth) between serial
108 samples (**Fig. 1B**). We also advanced the GoT method by incorporating immunophenotyping (*22*)
109 (GoT-IM) to link transcriptional and immunophenotypic cell identities (**Fig. 1B**). GoT-IM
110 provided genotyping data for the canonical *CALR* frameshift mutations for 72% of $CD34^+$ HSPCs
111 (n = 46,883 cells of total 65,452 cells), consistent with our previously reported genotyping rates
112 (*16*). In this way, we obtained somatic genotyping, whole transcriptomes, immunophenotyping
113 and treatment status for thousands of cells from the same GoT-IM experiment.

114 We hypothesized that IFNα may alter cell states but not induce novel cellular identities. We
115 integrated across the individual 24 samples to define the cell identities of the $CD34^+$ HSPCs
116 consistently across individual sampling (after analytically segregating the cells by time-point from
117 the same experiments, **Fig. 1C, fig. S1B-F, methods**) (*23*). As single-cell gene expression provides
118 high-resolution mapping of the HSPC identities, we clustered the cells based on gene expression
119 data and annotated the clusters based on canonical cell markers (**fig. S2A-C**, see **table S2** for cell
120 numbers)(*16, 24-26*). To identify HSCs, we leveraged the jointly captured immunophenotyping to
121 identify the $CD38^-$, $CD45RA^-$, $CD90^+$ HSCs (with high RNA expression of the HSC marker *AVP*
122 *(27)*, **Fig. 1D, fig. S2D**). We observed the expected cell types, such as megakaryocytic progenitors
123 (MkP) and immature myeloid progenitors (IMP, consisting predominantly of phenotypically
124 defined common myeloid progenitors (CMP) and granulo-monocytic progenitors (GMP) (*24*), **Fig.**
125 **1C, fig. S2A-C**).

126 Contrary to our hypothesis that IFNα may not induce novel cellular identities, we identified an
127 unknown cluster (Cluster X), previously not described in studies of normal or MPN bone marrow
128 $CD34^+$ cells (*16, 24-26, 28-30*) (**Fig. 1C**). Cluster X was immunophenotypically similar to the
129 IMPs based on $CD38^{mid}$, $CD45RA^{mid}$, and $CD90^-$ expression (**Fig. 1D**). To elucidate the identity
130 of Cluster X, we performed differential expression analysis between Cluster X and IMPs (**Fig. 1E,**
131 **left, table S3,** linear mixed model that explicitly models the effects of patient batch and treatment
132 status, see **methods**). We observed a striking upregulation of the immediate early response
133 transcription factors (TF) of the AP-1 (*JUN, FOS, JUNB, FOSB, ATF3, FOSL1, MAFF*), KLF
134 (*KLF2, KLF4, KLF6*), and NR4A (*NR4A1, NR4A2*) families (**Fig. 1E, left, table S3**). Other TFs
135 included interferon regulatory factor 1 (*IRF1*), indicating an inflammatory response. In addition,
136 we observed a robust upregulation of *RFX2* and *RFX3* TFs. While the *RFX2/3* factors are not well
137 characterized in HSPCs, RFX2 activity was identified as one of the key pro-survival transcription
138 factors activated in neutrophils during an inflammatory challenge in mice, particularly in the
139 transition from bone marrow to blood (*31*). Upregulation of *CEBPB* and *CEBPD*, implicated in
140 emergency granulopoiesis (*32*) and granulopoiesis under cellular stress (*33*), respectively, further
141 suggested a neutrophilic differentiation trajectory. Gene set enrichment analysis identified the
142 upregulation of TNFα signaling via NF-κB pathway (Adj. P-val = 1.6×10^{-4}), and downregulation
143 of the MYC targets (Adj. P-val = 1.6×10^{-4}, **Fig. 1E, right, table S4**). Incorporation of other HSPC
144 immunophenotypic markers revealed that these cells were also positive for CD44, CD117, dim
145 CD66b, and negative for HLA-DR, similar to IMPs and neutrophil progenitors (**fig. S2B)**. Based
146 on the transcription factors, immunophenotypes and pathways activated in Cluster X, we termed
147 these cells inflammatory granulocytic progenitors (IGP). Consistent with the identification of the
148 IGPs in this cohort of patients, the IGPs derived predominately from the IFNα-treated samples

149 with elevated frequencies in the IFNα-treated versus baseline CD34$^+$ cells (**Fig. 1F, fig. S2E**). As
150 the frequencies of IGPs were low, we confirmed that the elevated IGP frequencies in the IFNα
151 treatment samples were not simply due to a greater number of total CD34$^+$ cells captured in the
152 treated samples (**fig. S2E-F**). Separately integrating the samples based on treatment status also
153 confirmed the specificity of the IGPs to IFNα-treated bone marrow (**fig. S2G**). The presence of a
154 distinct IGP cluster in dimensional reduction of cells from individual experiments without any
155 batch correction reassured that IGPs were not a technical artifact of integration (**fig. S2H**).
156 Altogether, these data revealed that IFNα induces an alternate IGP state.

157 The differentially upregulated TFs in the IGPs were also highly enriched in a subset of quiescent
158 HSCs with elevated *AVP (27)* and CD90 expression, we labeled HSC-IG (**Fig. 1G, fig. S2D, S3A**).
159 The transcriptional similarities of the IGPs and HSC-IG (as revealed by their proximity on the
160 UMAP space) suggested that the IGPs may derive from HSC-IG. RNA velocity measurements
161 (*34, 35*) combined with partition-based graph abstraction (*36*) predicted cell state transitions from
162 HSC-IG to IGPs (**Fig. 1G, left, table S5**). To define the transcriptional state transitions from HSC-
163 IG to IGPs, we compared IGPs to HSC-IG and identified a reinforcement of the RFX3, AP-1,
164 CEBPB/D, and KLF family TF expressions and downregulation of NR4A2 (**Fig. 1G, right, fig.
165 S3B, table S3;** only IFNα-treated cells included in the differential expression analysis). As
166 NR4A1/2 have been reported to maintain HSC quiescence (*37, 38*), their downregulation in IGPs
167 relative to HSC-IG was consistent with the upregulation of differentiation and cell cycle-related
168 genes in the IGPs (**Fig. 1G, right, fig. S3B-D, table S4**). Upregulation of *MPO* (encoding
169 myeloperoxidase in primary granules) and *CSF3R* (encoding the G-CSF receptor), and
170 downregulation of the MHC class II genes (*CD74, HLA-DPA1, HLA-DRB1, HLA-DPB1*) further
171 provided evidence for its differentiation into the neutrophil lineage (**fig. S3B, table S4**).

172 To test the ability of HSCs to directly give rise to neutrophils, bypassing the conventional CMP
173 and GMP oligo-potent progenitor states, we utilized a similar strategy by which the direct
174 derivation of MkPs from HSCs (without traversing through the megakaryocytic-erythroid
175 progenitor state) was demonstrated in human cells (*39*). We performed single cell colony forming
176 unit assays by which we could track the differentiation of individual CD34$^+$, CD90^{high} bone
177 marrow HSCs from MPN patients at baseline and on IFNα therapy (**Fig. 1H, fig. S3E, methods**).
178 We identified that HSCs gave rise to mixed multilineage and monocyte-neutrophil colonies,
179 consistent with a passage through the oligo-potent progenitor states, but HSCs from IFNα-treated
180 patients also frequently gave rise to neutrophil-only colonies (CD66b$^+$, CD16$^+$, CD14$^-$), supporting
181 a direct passage to neutrophil development (**Fig. 1H, fig. S3E**). These data suggested that IFNα
182 induces an alternate and precipitous neutrophil developmental pathway that bypasses the typical
183 granulo-monocytic bi-potent progenitor states.

184 **Inflammatory neutrophils are enriched in IFNα-treated bone marrow**

185 To determine the identity of the immune cells that are downstream of the IGPs in an unbiased
186 manner, we performed GoT-IM on the CD34$^-$ compartments of the serial IFNα-treated samples
187 (**Fig. 2A, fig. S4A-B**, see **table S6** for cell numbers, **methods**). Similar to the CD34$^+$ cells, we
188 clustered the cells based on gene expression and annotated the cell types based on canonical gene
189 and protein markers (**Fig. 2B**, **fig. S4C**). We identified that the IGP gene signature was the highest
190 in a distinct group of neutrophils (Neu1, **Fig. 2C**). Consistently, unsupervised co-embedding of
191 the myeloid progenitors with the mature myeloid compartment revealed that the IGPs clustered

192 with the Neu1 subset of 'inflammatory' neutrophils (**fig. S4D**). Comparison of the gene expression
193 of the Neu1 subset to the other neutrophil group, Neu2 (at an equivalent stage of maturation based
194 on the expression level of CD66b, CD11b, CD16, **Fig. 2B**) revealed that Neu1 expressed
195 inflammatory cytokines such as *CXCL8* and *CXCL2* and the transcription factors observed in the
196 IGPs including *RFX2/3*, *AP-1*, *KLF2/4/6*, and *CEBPB/D* (**Fig. 2D, left, table S7**). Gene set
197 enrichment of the differentially expressed genes also highlighted TNFα signaling via NF-κB and
198 inflammatory pathways in the Neu1 subset (**Fig. 2D, right, table S7**), suggesting the propagation
199 of the inflammatory state of the IGPs to the mature progeny. These inflammatory neutrophils
200 derived predominantly from the IFNα-treated samples (**Fig. 2E**). Overall, these data demonstrated
201 that IFNα induced the development of inflammatory neutrophils.

202 **IFNα concurrently coordinates anti- and pro-inflammatory programs**

203 To assess the global transcriptional impact of IFNα, we examined the transcriptional distance of
204 HSCs between treatment time-points for individual patients. In an example case of patient IFN04
205 who showed partial clinical response (without evidence of disease progression, **table S1**), samples
206 from three timepoints were available – (1) baseline, (2) at one year on active treatment, and (3) at
207 four years but off therapy for 3 weeks at the time of collection. HSCs at year 1 displayed a
208 strikingly distinct transcriptional profile compared to baseline cells, whereas cells that had been
209 collected following discontinuation of therapy at year 4 were more similar to baseline HSCs (**Fig.
210 3A**), consistent with clearance of pegylated-IFNα at ~2-3 weeks (*40*). This contrasted with HSCs
211 from samples with two timepoints under active IFNα therapy (at years 1 and 2), which were
212 similarly distinct from the baseline HSCs (**fig. S5A**). Projection of the progenitor identity
213 assignments revealed that the HSPCs clustered based on cell identity as well as treatment status
214 (**Fig. 3A**, **fig. S2H**). The magnitude of the transcriptional impact of IFNα was in contrast to the
215 subtler effects of somatic mutations, such as those in *CALR (16), JAK2 (29, 41)*, and *DNMT3A
216 (42)*, resulting in co-mingling of mutated and wildtype cells, which could not be distinguished by
217 scRNA-seq data alone, as revealed by methods that incorporate genotyping and scRNA-seq (*16,
218 29, 42, 43*). Thus, we first examined the impact of IFNα on the overall hematopoiesis agnostic to
219 genotype status.

220 To define the transcriptional perturbations by IFNα, differential expression analyses were
221 performed between baseline and treated $CD34^+$ cells, as a function of cell identity. We identified
222 genes commonly regulated across multiple progenitor subsets upon IFNα administration,
223 including the canonical IFNα genes, such as *ISG15, IFITM3, IFI6* and *EPSTI1* (**Fig. 3B, fig. S5B,
224 table S8**). To test whether IFNα induces human HSCs into cell cycle entry, as reported in mice
225 (*9*), we examined the gene signatures for cell cycle phases shown to be an accurate assessment of
226 cell cycle status (*44*). Indeed, HSC rates of cell cycle entry were enhanced upon IFNα treatment
227 (**Fig. 3C, fig. S5C-D)**. A positive regulator of HSC quiescence (*45*), *CXCR4*, was downregulated
228 upon IFNα therapy, suggesting that *CXCR4* downregulation may help coordinate HSC activation
229 (**Fig. 3B**). We incorporated protein detection for CXCR4 (CD184) via GoT-IM and identified that
230 IFNα reduced surface CD184 expression (**fig. S5E)**. Consistently, CD184 downregulation was
231 observed in HSCs in cell cycle and enriched in IFNα-treated populations and, conversely, HSCs
232 with elevated CD184 expression were less likely to be in cell cycle and enriched in baseline
233 samples ($P = 1.5 \times 10^{-9}$, Fisher's exact test, **Fig. 3D**). In light of enhanced rates cell cycle entry of
234 HSCs with abrogation of *Cxcr4* in mice (*45*), these data suggested that CXCR4 downregulation
235 may play a role in permitting HSC cell cycle entry upon IFNα exposure.

236 In the treated MkPs, *CD9* and *VWF*, closely associated with MkP differentiation (*46-49*), were
237 downregulated (**fig. S5B, table S8**). We also observed a downregulation of *TGFB1* (**fig. S5B**),
238 which encodes the pro-fibrotic cytokine TGFβ established as one of the main inducers of marrow
239 fibrosis in patients with myelofibrosis (*50, 51*). We and others have shown that MPN
240 megakaryocytes exhibit increased *TGFB1* expression (*16, 50, 52*), and thus downregulation of
241 *TGFB1* by IFNα indicates a potential mechanism of disease amelioration by IFNα. To ensure that
242 the transcriptional changes we observed were specific to IFNα therapy, we performed scRNA-seq
243 on $CD34^+$ HSPCs from individuals with *CALR*-mutated ET who were treated with hydroxyurea,
244 at baseline and at one year of treatment, and observed no significant overlap between the genes
245 differentially regulated by IFNα and hydroxyurea (P = 0.599, Fisher's exact test, **fig. S5F-G**).

246 To determine which canonical pathways may be modulated by IFNα, we performed gene set
247 enrichment analysis using the Hallmark gene sets in the IFNα-treated versus baseline cells and
248 identified an upregulation of the IFNα signaling pathway across the cell subsets as expected (**Fig.
249 3E, table S9**). The analysis also confirmed the upregulation of cell cycle-related pathways (G2M
250 check point and E2F targets) as well as MYC targets (**Fig. 3E, table S9**), corroborating a previous
251 study that reported enhanced MYC protein expression during IFNα-induced cell cycle entry of
252 mouse HSCs (*53*). Consistent with the downregulation of *TGFB1* gene itself, gene set enrichment
253 analysis between baseline and IFNα-treated cells revealed a decrease in TGFβ signaling across
254 several HSPCs, including downregulation of *THBS1* and *SERPINE1* (**Fig. 3E, fig. S5B, table
255 S8,9)**. TGFβ signaling was particularly downregulated in the HSCs (**Fig. 3E**), as was observed in
256 mice and associated with HSC exit from quiescence (*10*).

257 Furthermore, in contrast to the pro-inflammatory state of the IFNα-associated IGPs, we observed
258 a downregulation of pro-inflammatory pathways, including the TNFα signaling via NF-κB and
259 inflammatory response pathways, across the stem and progenitor cells and especially pronounced
260 in the cDCPs (**Fig. 3E-F, table S9)**. Downregulated genes in the TNFα signaling via NF-κB
261 pathway included AP-1 subunits, an NF-κB subunit *NFKB1*, and *IL1B*, which encodes the pro-
262 inflammatory cytokine IL-1b (**Fig. 3F, table S8,9)**. Expression of *IL1R1* and *CXCL8* genes from
263 the inflammatory response pathway were also downregulated (**table S8)**. Previously, IFNα
264 treatment in mice has yielded mixed results demonstrating either an upregulation (*10*) or
265 downregulation (*54*) of TNFα by IFNα. Our findings indicated that in human, isolated IFNα exerts
266 an overall anti-inflammatory response, consistent with a previous report demonstrating decreased
267 *TNF* mRNA levels following IFNα therapy in patient samples (*55*).

268 To determine whether the IFNα-regulated pathways may be partially retained in the HSCs after
269 discontinuation of therapy, we compared HSCs from baseline to post-treated samples (IFN04,
270 IFN05, IFN06) not on active IFNα therapy (off therapy for ~3-4 weeks). We observed a residual
271 IFNα response signature and a slight downregulation of the TNFα signaling via NF-κB pathway
272 in the post-therapy samples compared to the baseline, but intriguingly, the TGFβ signaling was
273 upregulated in the post-treated HSCs compared to both baseline and actively treated HSCs (**Fig.
274 3G, fig. S5H**). These data suggested that following IFNα exposure, HSCs actively upregulate the
275 quiescence program, consistent with the report in mice that HSCs re-enter quiescence following
276 activation by type 1 IFN (*10*). Furthermore, post-therapy HSC-IG upregulated the gene expression
277 program that defined HSC-IG (versus HSC1, **Fig. 3G, fig. S5H**), suggesting the reinforcement of
278 the inflammatory signature with prior inflammatory exposure. Consistently, the HSC-IG and IGP
279 frequencies at baseline showed a trending increase with age (**fig. S5I**), and HSC-IGs exhibited a

280 higher aging gene signature compared to the other HSCs (**fig. S5J**) (*56*). Altogether, these data
281 implicated inflammatory neutrophil development as a feature of HSC memory – i.e., trained
282 immunity, a field that has largely focused on monocyte development thus far (*57*).

283 We next determined whether the anti-inflammatory state propagated to the mature immune cells
284 upon IFNα therapy. The mature immune cells displayed a greater degree of heterogeneity in their
285 response to IFNα compared to stem and progenitors, indicating a cell type-specific response to
286 IFNα (**fig. S5K, table S10,11**). Notably, IFNα did not induce cell cycle entry of mature immune
287 cells (**fig. S5K-L**). Nonetheless, IFNα therapy downregulated TNFα signaling in innate immune
288 cells, specifically classic dendritic cells and natural killer cells (**Fig. 3H, fig. S5K**). Immune cell
289 composition also reflected this shift to an anti-inflammatory condition, with the expansion of
290 regulatory T (Treg) cells (relative to other T-cell subsets), as well as a diminution of the pro-
291 inflammatory $CD16^+$ monocytes (within the monocytic compartment, **fig. S5M-N**) (*58, 59*). These
292 data indicated that the anti-inflammatory effects of IFNα on the stem and progenitor cells are likely
293 compounded by the anti-inflammatory state of the bone marrow immune microenvironment.

294 Given the induction of IGP differentiation and inflammatory neutrophils with upregulation of AP-
295 1 and NF-κB targets, these findings suggest that isolated IFNα initiates both *anti-inflammatory*
296 and *pro-inflammatory* states – both occurring in parallel within the same individual's
297 hematopoiesis. Consistently, we observed a significant overlap between the IFNα-downregulated
298 ($IFN\alpha^{DN}$) genes and genes upregulated in the IGPs (IGP^{UP}, **Fig. 1E, 3B, table S3,8,** $P = 1.6 \times 10^{-}$
299 ^{5}, hypergeometric test). The inverse, i.e., a significant intersection of $IFN\alpha^{UP}$ genes and IGP^{DN}
300 genes, was also observed ($P = 1.73 \times 10^{-69}$, hypergeometric test, **table S3,8**). Coherently, the HSC-
301 specific $IFN\alpha^{UP}$ gene signature (displayed in **Fig. 3B**) was significantly downregulated in the IGPs
302 compared to the HSCs while the $IFN\alpha^{DN}$ genes were upregulated in the IGPs (with both cell groups
303 under IFNα treatment; **Fig. 3I**). Altogether these data indicated that IFNα can precipitate opposing
304 cell states within the same HSC population. While previously the heterogeneity of HSC cell states
305 was linked with lineage outputs (*60, 61*), these data revealed that HSC heterogeneity may also
306 mediate polarized anti- and pro-inflammatory responses to regulate specialized immune function.

307 **IFNα potentiates lymphoid differentiation shift**

308 To determine how the transcriptional remodeling by IFNα may impact the hematopoietic
309 differentiation trajectories, we computed the proportion of stem and progenitor subsets within the
310 $CD34^+$ compartment before and following IFNα therapy. In addition to the expansion of the
311 alternate IGP state, IFNα also paradoxically induced a significant expansion of the lymphoid
312 progenitors (**Fig. 4A-B, fig. S6A**). While the expansion of lymphoid progenitors was an
313 unexpected finding as inflammatory cytokines have been demonstrated to induce myeloid priming
314 (*62-64*), it was consistent with the downregulation of pro-inflammatory pathways, including those
315 of the AP-1 subunits, associated with myeloid differentiation (*65*). In congruence with
316 downregulation of *VWF* and *CD9* expressions, we observed diminutions of the megakaryocytic-
317 erythroid lineage progenitors, including MkPs and erythroid progenitors (EP, **Fig. 4A-B**; paired
318 analyses from serial samples in **fig. S6A**).

319 To validate the generalizability of the lymphoid expansion, we analyzed clinical multi-parametric
320 flow cytometry data of bone marrow aspirates from patients with early-phase MPN with *JAK2* or
321 *CALR* mutations (n = 33 samples without IFNα exposure; n = 9 samples with IFNα therapy).

322 Indeed, we identified that the proportion of TdT$^+$, CD19$^+$ B-lymphoid progenitors within CD34$^+$
323 HSPCs increased in IFNα-treated bone marrow compared to control (**Fig. 4C, S6B, table S12)**.
324 We also observed an increased proportion of CD34$^+$, TdT$^+$, CD19$^+$ cells of all viable cells
325 analyzed, as well as an increase in the CD34$^-$, TdT$^-$, CD19$^+$ B-lymphocytes (**Fig. 4C)**, providing
326 evidence for an active lymphoid priming of HSCs leading to an expansion of the lymphoid
327 progenitors. These findings were specific to IFNα, and not observed upon hydroxyurea therapies
328 (**fig. S6B, table S12**). In support of lymphoid priming, HSCs exhibited an increased protein
329 expression of CD45RA (used to identify multipotent lymphoid progenitors, MLP) after IFNα
330 treatment (**Fig. 4D**). CD90 was downregulated, consistent with the IFNα effect of driving cell
331 cycle entry and differentiation (**Fig. 4D**). Importantly, CD90, CD38 and CD45RA expressions
332 were coherent with the transcriptional signature of HSCs following IFNα treatment (**fig. S6C**), in
333 contrast to mice progenitors that upregulate an HSC marker Sca-1 upon type 1 IFN treatment (*10*).
334 Consistent with active differentiation bias toward B-lymphoid progenitors, the mature B cell
335 compartment from IFNα-treated samples revealed a more immature B cell state compared to the
336 baseline B cells (**Fig. 4E)**, in the absence of proliferation of the CD34$^-$ B cell compartment (**fig.
337 S5K, S6D**). The major shifts in progenitor output by the HSCs suggested that the clinical
338 improvement in the patients' platelet count (despite variable molecular responses) may be due to
339 the differentiation skewing away from the megakaryocytic to the lymphoid lineage. Consistent
340 with this model, the proportions of MEPs and MkPs in CD34$^+$ cells could help predict the patient's
341 platelet counts (P = 0.0063, generalized linear model, **Fig. 4F**). These data thus supported a model
342 wherein the imbalance of hematopoietic differentiation landscape caused by somatic mutations in
343 HSCs may be corrected by IFNα, as a mode of therapeutic efficacy in hematopoietic neoplasms.

344 **GoT-ATAC identifies transcription factor regulatory networks that govern IGP**
345 **differentiation**

346 Chromatin accessibility enables approximation of TF activity based on accessibility of the TF
347 binding sites (*66-70*). Thus, to determine the regulatory networks that govern IFNα-induced
348 modulation of inflammatory and differentiation states, we expanded upon GoT to capture somatic
349 mutational status, chromatin accessibility and whole transcriptomes. We adapted the 10x
350 Multiome platform that captures single-nuclei RNA-seq (snRNA-seq) and chromatin accessibility
351 (snATAC-seq) to include somatic genotyping, i.e., GoT-ATAC (**Fig. 5A**). We applied GoT-ATAC
352 to serial bone marrow CD34$^+$ cells (n = 23,137 cells) from the clinical trial cohorts (n = 4 baseline,
353 3 IFNα-treated samples). As in GoT-IM, we incorporated time-point specifying barcoded
354 antibodies (*71*) to combine serial samples from the same individuals into a single experiment to
355 remove technical batch effects (**Fig. 5A, fig. S7A-E**). After we analytically segregated the baseline
356 and IFNα-treated samples (**fig. S7E**), we clustered the cells across samples based on the
357 transcriptomic and chromatin accessibility data and identified the same cell states identified by
358 GoT-IM, including the IGPs (**fig. S8A-E, table S13**).

359 As the IGPs were defined by a robust upregulation in gene expression of immediate early factors
360 and RFX2/3, we determined whether these TFs showed increased activity based on chromatin
361 accessibility of their binding sites. A differential TF motif enrichment analysis between IGPs and
362 HSCs revealed that the same TFs showed enhanced accessibility, including the motifs of the AP-
363 1 family (FOS, JUN, JUND, JUNB, FOSL1, FOSL2), CEBPB/D, and RFX2/3 (**Fig. 5B, fig. S8F,**
364 **table S14**). Consistent with the overexpression of *IRF1* in IGPs, differential motif enrichment
365 analysis also isolated IRF1 as the main interferon regulatory factor active in the IGPs. The

differential motif analysis further revealed an upregulation of STAT2 and the proinflammatory REL of the NF-κB complex (**Fig. 5B, fig. S8F, table S14**), consistent with the observed gene expression upregulation of the NF-κB pathway (**Fig. 1E, fig. S3B**). While TF expression data are often sparse in scRNA-seq, these data demonstrated a high concordance of TF gene expression and their binding motif accessibility, suggesting a rapid induction of the IFNα transcriptional regulatory program.

To determine which TFs upregulated the gene expressions of RFX2/3, we determined TF motifs present in the regulatory peaks that correlated with their gene expression (i.e., linked peaks analysis) (*72*). In the cis-regulatory region of RFX3, we identified the binding motifs of STAT2 and IRF1, as well as FOSB and PU.1, which were upregulated at the gene expression level in IGPs **(fig. S9A-B, table S15**). Likewise, the most significant regulatory regions for RFX2 included motifs for PU.1, KLF factors, NR4A1/2 and AP-1 subunit factors (**fig. S9A,C, table S15**). To determine the regulatory networks that govern the robust upregulation of the AP-1 subunits in the IGPs, we assessed for motif enrichment in the positive regulatory peaks for the AP-1 TFs in aggregate and identified RFX2-4 (which have the same binding motifs) as among the most significant TFs (**Fig. 5C, table S16**). Thus, RFX2/3 and AP-1 TF groups positively regulated the expression of the other, synergizing IGP development. These data provided evidence for a model wherein HSC-IG with elevated expression of RFX2/3 and AP-1 subunits and other immediate early response factors were primed toward a robust transcriptional program for IGP differentiation upon IFNα signaling.

Furthermore, as other RFX members (i.e., RFX1 and RFX8) play key regulatory roles in MHC class II expression (*73-75*), we hypothesized that RFX2/3 may downregulate MHC class II in the IGPs. To test this, we determined the significantly linked peaks that negatively regulated *HLA-DRA* expression (**fig. S10A, bottom**) (*72*). We identified a distal regulatory region with four negative regulatory loci (**fig. S10A, inset**). These peaks included motifs for IRF1 and STAT2 as well as immediate response factors including AP-1 and KLF families, but not RFX2/3 (**fig. S10A, inset, table S17**). However, within the same negative regulatory region, we identified an IGP-specific peak that included the binding motif for RFX1-4, KLF factors and IRF1 (**fig. S10A, top, table S17**). These findings identified the immediate response factors, IRF1 and STAT2 as negative regulators of MHC class II genes across cell types, while RFX2/3 binding was specific for MHC class II downregulation during IGP differentiation. Consistently, surface HLA-DR was suppressed in the IGPs in the GoT-IM data (**fig. S10B**). Genes positively regulated by RFX2/3 included *MPO* and genes involved in cell cycle entry (**table S18**), suggesting that these factors play an essential role in activating the IGPs.

As *RFX3* was upregulated in the HSC-IG to IGP transition, we overexpressed *RFX3* in primary cord blood $CD34^+$ cells via lentiviral transduction to determine whether RFX3 may regulate granulocytic differentiation. Methylcellulose-based colony forming unit assays of *RFX3* overexpressing (RFX3-OE) $CD34^+$ cells revealed that *RFX3* overexpression expanded the granulocytic colonies (CFU-G) and diminished the erythroid colonies (CFU-E) compared to control-vector transduced $CD34^+$ cells (**Fig. 5D, fig. S10C-D)**. To determine whether RFX3 may regulate neutrophil differentiation at the $CD34^+$ HSPC stage, we performed single-cell RNA-seq of RFX3-OE $CD34^+$ cells with control-vector cells and non-transduced cells. We identified an IGP-like progenitor state that was highly enriched for the RFX3-OE HSPCs (**Fig. 5E, fig. S10E-I**). Compared to the IMPs, this IGP-like progenitor state recapitulated the IGP signature including

410 upregulation of AP-1 subunit TFs and *CEBPD* among other TNFα signaling via NF-κB pathway
411 genes, and downregulation of the MYC pathway (**Fig. 5F, table S19**). These data highlighted
412 RFX3 as a key transcription factor regulator of IGP development.

413 **PU.1 underlies hematopoietic differentiation remodeling by IFNα**

414 Furthermore, the GoT-ATAC data also confirmed the expansion of the lymphoid progenitors upon
415 IFNα treatment (**fig. S11A**). To determine the regulatory networks that governed the
416 differentiation skewing by IFNα, we performed differential motif enrichment analysis between
417 IFNα-treated and baseline HSCs. IFNα enhanced the activities of STAT2 and several interferon
418 regulatory factors in HSCs, in contrast to the specific activity of IRF1 in IGPs (**Fig. 5G, table**
419 **S20**). IFNα downregulated the motif accessibility of AP-1 TFs (**Fig. 5G**), consistent with the
420 downregulation of AP-1 TF gene expression associated with TNFα signaling via NF-κB (**Fig. 3B**).
421 Moreover, the accessibility of the TWIST1 motif was enhanced after treatment (**Fig. 5G**),
422 consistent with a previous report that identified TWIST1 as mediating the downregulation of
423 TNFα upon type 1 IFN treatment (*54*). Furthermore, the activity of TGFβ induced factor
424 homeobox 2 (TGIF2), which inhibits TGFβ response genes, was also enhanced (**Fig. 5G, table**
425 **S20**), highlighting TGIF2 as another key factor involved in the downregulation of the observed
426 TGFβ signaling after IFNα treatment.

427 Importantly, critical TFs involved in hematopoietic differentiation (*76*) were differentially
428 regulated. Notably, motif accessibilities of PU.1 and RUNX1, essential for early lymphoid and
429 granulo-monocytic differentiation (*76*), were enhanced by IFNα (**Fig. 5G, table S20**). The
430 activities of GATA1/2, reported to be negatively regulated by PU.1 (*76*), were downregulated as
431 well as those of another critical megakaryocytic-erythroid lineage factor, TAL1 (*77*). These
432 findings were consistent with the differentiation away from the megakaryocytic-erythroid lineages
433 upon IFNα treatment. Furthermore, the accessibilities of the motifs of the critical early B-lymphoid
434 differentiation factors TCF3/4 were enhanced (*71, 78, 79*), highlighting TCF3/4 as TFs that govern
435 the differentiation toward lymphoid progenitors by IFNα. CEBPA/B/D, essential for granulo-
436 monocytic development (*80, 81*), were also upregulated in its motif accessibility (**Fig. 5G, table**
437 **S20**). Importantly, the IRFs (*82, 83*), RUNX1 (*84*), CEBPA (*85*) and TCF3 (*86*) have been
438 demonstrated to co-regulate target gene expression with PU.1, suggesting that enhanced PU.1
439 activities may have enhanced the activities of its co-regulating TFs, such as CEBPA and TCF3.
440 To confirm these co-regulations in IFNα-remodeled hematopoiesis, we examined the synergistic
441 activities of the different combinatorial TFs by measuring the excess variability of accessibility
442 for peaks with both TF motifs (compared to peaks with one motif) (*69*). Indeed, PU.1 exhibited
443 synergistic activities with IRF1, RUNX1, CEBPA and TCF3, while displaying antagonism with
444 GATA1 and TAL1 (**Fig. 5H**). To determine the activities of these TFs upon lymphoid
445 differentiation, we assessed the motif accessibilities of the TFs across the early and late
446 progenitors. The activities of PU.1, RUNX1 and CEBPA were enhanced upon IFNα signaling
447 during the early stages of hematopoiesis and diminished with lymphoid development, whereas the
448 activities of TCF3 were more pronounced in the later stages of development (**Fig. 5I**). These data
449 highlighted PU.1 as a master regulator of IFNα-induced differentiation.

450 To determine whether IFNα may directly upregulate the expression of PU.1, we assessed the
451 regulatory peaks of PU.1 gene itself and identified the binding motifs of interferon regulatory
452 factors (**fig. S11B, table S16**). Consistently, PU.1 gene expression increased upon IFNα treatment

453 in stem and early progenitor cells (**fig. S11C**). IFNα treatment of a hematopoietic cell line (K562)
454 in vitro upregulated PU.1 gene and protein expression (**fig. S11D-E**), consistent with a previous
455 report (*87*), demonstrating that IFNα directly upregulates the expression of PU.1. As PU.1
456 regulatory peaks also included CEBPA binding motifs, we overexpressed CEBPA in K562 cells
457 and observed enhanced expression of PU.1 (**fig. S11F**). We further tested whether enhanced PU.1
458 may, in turn, co-regulate the expressions of canonical type 1 IFN targets. Overexpression of PU.1
459 in K562 cells with or without IFNα treatment revealed that PU.1 overexpression led to
460 upregulation of *IRF1* and *B2M* and downregulation of *ISG20* and *IFIH1*, as examples (**fig. S11G-**
461 **H**). Altogether, these studies revealed that IFNα signaling caused a global rewiring of TF
462 regulatory activities, particularly through PU.1 for both lymphoid and IGP expansion, that
463 underpinned the concerted transcriptional and differentiation remodeling.

464 **Somatic mutations modify the downstream effects of IFNα**

465 Having established the overall effects of IFNα on hematopoiesis, we next determined the
466 differential effects of IFNα on *CALR*-mutated versus wildtype stem and progenitor cells,
467 specifically in relation to the effects of IFNα on the clonal fitness of HSCs (**Fig. 6A, fig. S12A**).
468 The high genotyping efficiency of GoT-IM enabled us to track the clone size precisely within the
469 HSCs, revealing that IFNα caused variable changes to the *CALR*-mutated clone size (**Fig. 6B, fig.**
470 **S12B**), consistent with previous reports of bulk sequencing on peripheral blood samples (*12, 13,*
471 *15, 17*). Current models of inflammation-induced perturbation to clonal evolution build on the
472 induction of cell cycle entry of clonal HSCs for enhanced fitness (*5*) or differentiation and
473 depletion (*9, 12, 13*). We therefore determined whether differential upregulation of HSC cell cycle
474 entry might predict clonal dynamics. Across the patients regardless of clonal dynamics, IFNα
475 induced greater rates of cell cycle entry of *CALR*-mutated HSCs compared to the wildtype
476 counterparts (**Fig. 6C, fig. S12C**). These results indicated that the mutated HSCs were likely
477 primed for a more robust proliferative response, compared to the wildtype counterparts, potentially
478 due to the baseline cell cycle activity enhanced by the *CALR* mutations. In support of this model,
479 IFNα boosted the proliferation to a greater degree in the mutated cells compared to wildtype within
480 the myeloid lineages, especially those of the megakaryocytic-erythroid, but not the lymphoid
481 progenitor compartment—that is, restricted to the progenitor subsets in which the *CALR*-mutation
482 caused enhanced proliferation at baseline (*16*) (**fig. S12C**). We orthogonally validated that IFNα
483 effected greater proliferative rates in the myeloid HSPCs by performing multiplexed *in situ*
484 fluorescent imaging of bone marrow paraffin-embedded sections from patients with *CALR*-
485 mutated MPN with or without IFNα treatment (n = 5 without IFNα, n = 4 with IFNα, **Fig. 6D, fig.**
486 **S12D**). We determined the protein expression of CD34, CD117, CD38, Ki67 and mutated CALR
487 (*88*) to assess the frequencies of $CD34^+$, $CD38^+$, $CD117^+$ myeloid progenitors that express Ki67,
488 a gold standard of cell cycle entry (*89*). The availability of a mutated CALR-specific antibody
489 enabled us to identify that the frequency of cycling mutated myeloid progenitors was higher
490 compared to that of wildtype with or without IFNα exposure (**Fig. 6D**). Overall, these findings
491 provided evidence that IFNα enhanced the cell cycle entry of the HSPCs to the degree
492 predetermined by baseline priming. Thus, while enhancing absolute rates of cell cycle entry across
493 the stem cells, the relative difference in cell cycle rates between mutated and wildtype HSCs at
494 baseline were preserved upon IFNα exposure. These data indicated that inflammation-induced cell
495 cycle entry rates may be decoupled from clonal dynamics.

496 To determine whether IFNα exposure may preserve other key features of *CALR*-mutation effects,
497 we compared the gene expression profiles between wildtype and mutated cells, at baseline and
498 following IFNα therapy. Intriguingly, we observed the same differentially expressed pathways
499 between the IFNα-treated mutated and wildtype HSCs, including the unfolded protein response
500 (UPR) (*16, 90, 91*), likely due to a heterozygous loss of the wildtype *CALR* that encodes a critical
501 chaperone protein (**fig. S12E-F, table S21-24**). IFNα globally remodeled the differentiation
502 toward lymphoid development, reducing the overall megakaryocytic bias in the mutated cells (**Fig.
503 6E**). Indeed, the frequencies of mutated MkPs and MEPs better predicted the patients' platelet
504 counts compared to overall frequencies of MkPs and MEPs (**fig. S12G**). However, the lymphoid
505 expansion was constrained in the mutated compartment due to the relative expansion of the
506 granulo-monocytic and megakaryocytic-erythroid progenitors compared to wildtype HSPCs
507 (consistent with the differential upregulation of cell cycle entry in the mutated myeloid
508 progenitors, **Fig. 6E-F, fig. S12C**). Furthermore, computation of the mutant cell frequency across
509 the progenitor subsets before and after treatment revealed that the enrichment of the mutated cells
510 in the myeloid compartments did not change following IFNα treatment (**fig. S12H**). Altogether,
511 these data revealed that phenotypic responses to IFNα are constrained (e.g. lymphoid
512 differentiation) or amplified (e.g. cell cycle entry) by somatic mutations, such that cell state
513 distinctions between the mutated and wildtype cells are preserved upon IFNα signaling.

514 We therefore hypothesized that *CALR*-mutations may alter the chromatin state of the binding sites
515 of IFNα-regulated TFs and thereby modulate their activities following therapy. We tested
516 differential TF motif enrichment via GoT-ATAC between the mutated versus wildtype stem and
517 early progenitors at baseline (**Fig. 5A**). The binding sites of NFKB1/2 were enhanced in the
518 mutated cells, consistent with our previous report of the gene set enrichment of the NF-κB pathway
519 in the *CALR*-mutated early HSPCs (*16*). We also identified that the chromatin accessibility of PU.1
520 and CEBPA were increased in the mutated cells (**Fig. 6G, table S25**). These data suggested that
521 *CALR* mutations alter the chromatin state of key lineage specifying TF binding sites, skewing the
522 lineage-modulating activities of IFNα. Specifically, these data indicated that IFNα-induced PU.1
523 activities may be skewed toward granulo-monocytic (versus lymphoid) development via enhanced
524 PU.1 and CEBPA co-activity in the mutated HSPCs.

525 To directly assess the impact of differential PU.1 activity due to the mutation status on modulating
526 the effects of IFNα, we performed a chromatin binding assay (CUT&RUN) (*92*) for PU.1 in UT7
527 cell lines expressing MPL (thrombopoietin receptor) and either the mutant *CALR* (type 1,
528 L367Tfs*46) or wildtype *CALR* transgene (*93*) treated with IFNα (**fig. S13A, table S26**). We
529 observed that PU.1 binding sites were enriched in the mutated cells compared to wildtype,
530 consistent with the GoT-ATAC data and the myeloid bias induced by the *CALR* mutation (**Fig.
531 6H, left**). Following IFNα treatment in vitro, we observed co-enrichment of PU.1-bound peaks
532 with IFNα-specific transcription factor motifs, including IRF4/8, which are known to cooperate
533 with PU.1 in the Ets-IRF composite elements (EICE) to mediate lymphoid and myeloid
534 differentiation (**fig. S13B, table S27**) (*83, 94, 95*). We observed that IFNα enhanced PU.1 binding
535 at distal regulatory regions (**fig. S13C**), the regions that regulate the differential commitment to
536 the lymphoid versus monocytic lineages by PU.1 (*96*). In these distal peaks, PU.1 binding sites
537 were enriched for CEBPA/B co-binding sites in the *CALR* mutated cells compared to the wildtype
538 (**Fig. 6H, right, fig. S13D, table S28**). These data demonstrated that *CALR* mutations enhance
539 PU.1 binding activities and alter the preferential cooperating TF partners of PU.1. Overall, these

540 results suggested that somatic mutations may alter the chromatin state of TF regulatory regions,
541 which in turn modulate the downstream effects of inflammatory activation.

542 **IFNα regulates clonal fitness of HSCs via IGP development**

543 While IFNα induced cycling of *CALR*-mutated HSCs at a higher frequency than wildtype HSCs
544 consistently across patient samples, clonal dynamics following therapy was heterogeneous (**Fig.**
545 **6B**). To investigate other factors that may contribute to the effects of IFNα on clonal dynamics,
546 we examined an unusual case in which the mutated clone expanded substantially with IFNα
547 therapy in patient IFN02 (**Fig. 6B**). Interestingly, the HSPCs from patient IFN02 harbored a
548 subclone with another mutation in *CALR*, a single nucleotide variant in the *CALR* allele (M131I,
549 predicted to impact protein structure (*97*)) which is trans to the MPN-causing frameshift mutation
550 (**fig. S14A**). At baseline, the double mutant clone remained subclonal to the dominant clone with
551 the single canonical *CALR* mutation (**Fig. 6I, fig. S14B**). Upon IFNα therapy, the double mutant
552 clone overtook the neoplasm and the overall stem cell population, even though the double mutant
553 clone did not exhibit significant difference in cell-cycle entry rates compared to single mutant
554 HSCs at baseline (**Fig. 6I, fig. S14C**). The additional insult to CALR activities in the double mutant
555 clone effected a greater UPR activation compared to single mutant HSCs, as expected (**fig. S14D-**
556 **E, table S29-30**). Surprisingly, however, the predominant signatures of the double mutant HSCs
557 compared to other HSCs at baseline were an upregulation of IFN response genes and decreased
558 TNFα and TGFβ signaling (**fig. S14D-E, table S29-30**), thus recapitulating the HSC response to
559 extrinsic IFNα and supporting a potential causal link between UPR and IFN activation (*98*).
560 Consistently, the double mutant HSCs exhibited increased expression of the HSC-specific $IFN\alpha^{UP}$
561 gene signature (**Fig. 3B**) at baseline and even higher expression upon IFNα therapy (**Fig. 6J, left**).
562 Similarly, the $IFN\alpha^{DN}$ gene signature was downregulated in the double mutant clone at baseline
563 and to a greater degree following treatment (**fig. 6J, right**). Further, unbiased clustering and
564 dimensional reduction revealed that the double mutant clone at baseline clustered with the treated
565 HSCs rather than with the other baseline HSCs (**fig. S14F-G**). As the double mutant HSCs share
566 the same microenvironment as the wildtype and single mutant HSCs, the striking similarity of the
567 intrinsically activated IFNα signaling in the double mutant cells at baseline to the extrinsic IFNα
568 effects indicated that the predominant IFNα signaling signatures observed in the IFNα-treated
569 HSCs may be largely direct rather than secondarily mediated by the effects of IFNα on other cell
570 types. These findings also highlighted a genotype-specific modulation of HSC fitness by IFNα.

571 As the IGP^{UP} signature has a significant overlap with the $IFN\alpha^{DN}$ gene signature (including the
572 immediate early response TFs), the significant downregulation of the $IFN\alpha^{DN}$ gene signature of
573 the double mutant cells suggested that the double mutant HSCs may be resistant to IGP
574 development. Consistent with this hypothesis, the double mutant HSCs expressed lower IGP^{UP}
575 and higher IGP^{DN} signatures (**fig. S14H**). Altogether, these data raised the hypothesis that the
576 resistance of clonal stem cells to differentiate into the IGPs may dictate its clonal fitness upon
577 IFNα signaling. We therefore computed the fold change in clone size as a function of the difference
578 in the frequencies of mutant cell frequency within the HSC-IG and IGPs relative to that of the total
579 $CD34^+$ compartment (**Fig. 6K**). Indeed, the propensity of clonal HSCs to differentiate into IGPs
580 could model clonal dynamics (**Fig. 6K**). These findings identified the alternate IFNα-specific route
581 of differentiation into IGPs as an avenue to perturb clonal dynamics, while perturbations to the
582 existing programs did not lead to a net difference in fitness between mutated and wildtype HSCs.
583 To test the generalizability of this model, we examined the IGP^{DN} gene signatures in *DNMT3A*-

584 mutated HSCs from individuals with clonal hematopoiesis (*42*), as *DNMT3A*-mutated clones are
585 resistant to IFNα, frequently expanding upon treatment (*15*). Consistently, the *DNMT3A*-mutated
586 HSCs demonstrated increased expression of the IGP^{DN} gene signature compared to the admixed
587 wildtype HSCs (**Fig. 6L**), suggesting that the *DNMT3A*-mutated HSCs may be resistant to IGP
588 development. These results therefore support a unified model of clonal dynamics wherein the
589 differential propensity of HSC clones to differentiate into the IGPs determines the clonal
590 composition of the stem cell niche under inflammation.

591 **Discussion**

592 Here, our studies deconvoluted the pleotropic effects of IFNα in reshaping the differentiation
593 trajectories of human HSCs for normalization of blood counts and modulation of clonal dynamics
594 in myeloproliferative neoplasms. The single-cell multi-omics methods applied to serial sampling
595 enabled us to track clonal evolution over a treatment period together with differential phenotypic
596 remodeling of mutated versus wildtype stem and progenitor cells. We identified that the underlying
597 somatic mutations both amplified the IFNα effects (e.g., cell cycle entry) and constrained others
598 (e.g., lineage skewing). In this way, the relative distinctions between the mutated and wildtype
599 HSPCs were preserved, despite the global remodeling of hematopoiesis. These findings suggested
600 that the relative fitness of clonal HSCs via programs already activated at baseline also remained
601 constant. Thus, differential HSC activation into cell cycle entry alone could not fully explicate the
602 inflammation-induced changes in clonal dynamics.

603 Instead, we identified an IFNα-specific alternate route of differentiation directly from HSCs that
604 predicted clonal dynamics based on priming of clonal stem cells to differentiate into the IGP state,
605 enabling resisting HSC clones to dominate the stem cell niche. Furthermore, identification of the
606 IGP population highlighted an intriguing phenomenon in human HSCs: induction of the IGP
607 differentiation through upregulation of the pro-inflammatory AP-1 and NF-κB activities indicated
608 that IFNα potentiates a pro-inflammatory as well as an overall anti-inflammatory cell states with
609 downregulation of the same AP-1 and NF-κB activities within the same hematopoietic
610 differentiation program. Differential expression levels of *RFX2/3* and immediate early response
611 programs within the HSC populations were highlighted in our data as mediating the polarized
612 response to IFNα, revealing a key functional relevance of HSC heterogeneity. These data
613 suggested that HSC-IG with elevated *RFX2/3* and immediate early response gene expressions were
614 poised to a precipitous pro-inflammatory response to stimuli, implicating these HSCs in innate
615 immune memory or trained immunity, i.e. an adapted innate immune response due to a prior
616 inflammatory activation of HSCs (*99, 100*). Trained immunity may thus serve as a non-genetic
617 modifier of IGP priming, reflecting the interpatient variabilities in the rates of IGP development
618 by the *CALR*-mutated stem cells. Notably, these results were highly concordant with a recent report
619 of inflammatory memory HSCs that have significant overlaps with HSC-IG in gene expression
620 and a similar retention of the inflammatory phenotype following resolution of active inflammatory
621 stimulation (*56*). In this study, downregulation of the inflammatory signature by clonal stem cells
622 in the context of CH was also associated with clonal fitness (*56*). These findings therefore
623 highlighted a novel connection between trained immunity and clonal dynamics, further shedding
624 insights into the impact of age-related inflammation to clonal expansion and malignant
625 transformation.

626 Furthermore, Type 1 IFN, the first FDA-approved immunotherapy (*101*), remains an effective
627 treatment and is being tested across various autoimmune (*102, 103*), cancer (*104*) and infectious
628 disease contexts (*105, 106*), including COVID-19 (*107, 108*). In the context of MPN, IFNα is the
629 only agent to consistently to deplete clonal stem cells. While previous studies have not detected
630 improvement in disease progression in patients treated with IFNα (*20, 109*), large clinical trial cohorts
631 would be required to detect significant differences between the IFNα and control arms, as the rates of
632 disease progression are low in patients with ET. Moreover, our identification of the HSC-specific IFNα
633 response, which includes IFNα/γ response upregulation and downregulation of the targets of TNFα
634 and TGFβ signaling pathways, may help clarify its therapeutic efficacy in other disease contexts
635 beyond MPN. In mouse studies, IFNα has been demonstrated to modulate TNFα expression (*110*)
636 with data suggesting either an upregulation (*10*) or downregulation (*54*) of TNFα by IFNα. Thus,
637 our studies clarify that the predominant effect of IFNα in human HSPCs is the downregulation of
638 downstream pathways involved in TNFα signaling via AP-1 and NF-κB, consistent with
639 amelioration of the inflammatory state in MPN and multiple sclerosis upon type 1 IFN
640 administration (*17, 107*). It also suggested that individuals with deficiencies in type 1 IFN may
641 have exhibited exaggerated response to COVID-19 infections (*111, 112*) due to the inability to
642 counterbalance the pro-inflammatory effects of the other cytokines. Coherently, *TNF* expression
643 was demonstrated to be decreased in patients with MPN who received IFNα treatment (*55*). The
644 pro-fibrotic TGFβ signaling was also broadly downregulated across progenitor subsets, through a
645 coordinated downregulation of the *TGFB1* gene itself and upregulation of the TGFβ signal
646 inhibiting TGIF2 activity. In this way, IFNα downregulated two key cellular programs involved
647 in the MPN-associated pathology, potentially underlying improved disease states. Moreover, as
648 NF-κB and TGFβ signaling are both implicated in HSC quiescence (*113-116*), the anti-
649 inflammatory effects of IFNα were also linked with HSC exit from quiescence. The robust
650 upregulation of TGFβ signaling in the HSCs following resolution of an acute IFNα exposure
651 supported data in mice of re-entry into quiescence to protect from HSC depletion following
652 inflammation-induced cell cycle entry (*10*).

653 Another major finding in our work was the remodeling of hematopoietic differentiation toward the
654 lymphoid lineage by IFNα. While various differentiation skewing by IFNα has been reported in
655 mice (*117-119*), the interpretation of the results is complicated by the alteration of the HSC-marker
656 Sca-1 upon IFNα exposure in mice (i.e. induction of Sca-1 in the CMPs, GMPs and MEPs,
657 resulting in their inclusion within the Sca-1$^+$, Kit$^+$ HSC/multipotent progenitor compartment) (*10*).
658 As other inflammatory cytokines, such as TNFα, IL-1, and IFNγ, have been demonstrated to
659 induce granulo-monocytic differentiation (*62-64, 120, 121*), IFNα presents as a unique cytokine
660 among the inflammatory milieu to balance the granulo-monocytic differentiation with its positive
661 regulation of B-lymphoid differentiation as another mode of dampening the pro-inflammatory
662 response.

663 The reshaping of the differentiation landscape by IFNα provided a novel model of therapeutic
664 efficacy in patients with myeloid neoplasms. As MPNs are primarily the result of a defect in
665 homeostatic hematopoietic development, due to an abnormal differentiation skewing and
666 proliferation of the myeloid lineages, IFNα-induced lymphoid differentiation may serve to balance
667 the differentiation landscape. IFNα reshaped the major bifurcation divide in MPN, that is, from
668 the JAK2/STAT5-mediated bifurcation at the myeloid (i.e., granulo-monocytic and
669 megakaryocytic-erythroid) versus lymphoid commitment, to the PU.1-mediated bifurcation at
670 granulo-monocytic and lymphoid versus megakaryocytic-erythroid commitments. These two

models have been described based on the identification of stem progenitor cells that produce myeloid (*122*) or lymphoid lineages (*123*) versus granulo-monocytic-lymphoid lineages (*124*). Our data provide evidence for a plastic differentiation hierarchy in which PU.1-mediated production of granulo-monocytic and lymphoid lineages at the expense of megakaryocytic-erythroid lineages are prioritized in perturbed settings, such as infection. The ability of IFNα to directly upregulate PU.1 expression suggested that the differentiation modulating effects of IFNα may be largely direct. These findings are consistent with the landmark study from Essers *et al.* that elegantly demonstrated the ability of IFNα to directly activate HSCs into cell cycle entry, via an in vivo cell mixing study in which only a small minority of the bone marrow cells harbored intact IFNα receptors (*9*). The cell cycle entry rate was further enhanced with increasing frequency of bone marrow cells with intact IFNα signaling, suggesting that IFNα effects are both directly and indirectly mediated.

Overall, these studies revealed the pleiotropic modes of therapeutic efficacy of IFNα and principles of clonal dynamics upon inflammatory activation. Importantly, our work motivates the development of novel therapeutic strategies to deplete clonal stem cells by enhancing their differentiation rates into the IGP state upon IFNα therapy, a strategy that may be generalizable across myeloid neoplasms and clonal hematopoiesis.

688 **References**

689 1. S. Jaiswal *et al.*, Clonal Hematopoiesis and Risk of Atherosclerotic Cardiovascular
690 Disease. *N Engl J Med* **377**, 111-121 (2017).
691 2. S. Jaiswal *et al.*, Age-related clonal hematopoiesis associated with adverse outcomes. *N*
692 *Engl J Med* **371**, 2488-2498 (2014).
693 3. L. Busque *et al.*, Recurrent somatic TET2 mutations in normal elderly individuals with
694 clonal hematopoiesis. *Nat Genet* **44**, 1179-1181 (2012).
695 4. S. Avagyan *et al.*, Resistance to inflammation underlies enhanced fitness in clonal
696 hematopoiesis. *Science* **374**, 768-772 (2021).
697 5. A. Heyde *et al.*, Increased stem cell proliferation in atherosclerosis accelerates clonal
698 hematopoiesis. *Cell* **184**, 1348-1361.e1322 (2021).
699 6. M. Meisel *et al.*, Microbial signals drive pre-leukaemic myeloproliferation in a Tet2-
700 deficient host. *Nature* **557**, 580-584 (2018).
701 7. Z. Cai *et al.*, Inhibition of Inflammatory Signaling in Tet2 Mutant Preleukemic Cells
702 Mitigates Stress-Induced Abnormalities and Clonal Hematopoiesis. *Cell Stem Cell* **23**, 833-
703 849.e835 (2018).
704 8. J. J. Trowbridge, D. T. Starczynowski, Innate immune pathways and inflammation in
705 hematopoietic aging, clonal hematopoiesis, and MDS. *J Exp Med* **218**, (2021).
706 9. M. A. Essers *et al.*, IFNalpha activates dormant haematopoietic stem cells in vivo. *Nature*
707 **458**, 904-908 (2009).
708 10. E. M. Pietras *et al.*, Re-entry into quiescence protects hematopoietic stem cells from the
709 killing effect of chronic exposure to type I interferonsIFN-1 effects on HSC function. *J Exp*
710 *Medicine* **211**, 245-262 (2014).
711 11. M. T. Baldridge, K. Y. King, N. C. Boles, D. C. Weksberg, M. A. Goodell, Quiescent
712 haematopoietic stem cells are activated by IFN-gamma in response to chronic infection.
713 *Nature* **465**, 793-797 (2010).
714 12. T. N. Rao *et al.*, JAK2-V617F and interferon-α induce megakaryocyte-biased stem cells
715 characterized by decreased long-term functionality. *Blood* **137**, 2139-2151 (2021).
716 13. M. Mosca *et al.*, Inferring the dynamics of mutated hematopoietic stem and progenitor cells
717 induced by IFNα in myeloproliferative neoplasms. *Blood* **138**, 2231-2243 (2021).
718 14. J. L. Spivak, Myeloproliferative Neoplasms. *N Engl J Med* **377**, 895-896 (2017).
719 15. T. A. Knudsen *et al.*, Genomic profiling of a randomized trial of interferon-α vs
720 hydroxyurea in MPN reveals mutation-specific responses. *Blood Adv* **6**, 2107-2119 (2022).
721 16. A. S. Nam *et al.*, Somatic mutations and cell identity linked by Genotyping of
722 Transcriptomes. *Nature* **571**, 355-360 (2019).
723 17. J. Czech *et al.*, JAK2V617F but not CALR mutations confer increased molecular responses
724 to interferon-α via JAK1/STAT1 activation. *Leukemia* **33**, 995-1010 (2019).
725 18. T. Klampfl *et al.*, Somatic mutations of calreticulin in myeloproliferative neoplasms. *N*
726 *Engl J Med* **369**, 2379-2390 (2013).
727 19. A. Yacoub *et al.*, Pegylated interferon alfa-2a for polycythemia vera or essential
728 thrombocythemia resistant or intolerant to hydroxyurea. *Blood* **134**, 1498-1509 (2019).
729 20. J. Mascarenhas *et al.*, A randomized phase 3 trial of interferon-α vs hydroxyurea in
730 polycythemia vera and essential thrombocythemia. *Blood* **139**, 2931-2941 (2022).
731 21. M. Stoeckius *et al.*, Cell Hashing with barcoded antibodies enables multiplexing and
732 doublet detection for single cell genomics. *Genome Biol* **19**, 224 (2018).

733 22. M. Stoeckius *et al.*, Simultaneous epitope and transcriptome measurement in single cells.
734 *Nat Methods* **14**, 865-868 (2017).
735 23. A. Butler, P. Hoffman, P. Smibert, E. Papalexi, R. Satija, Integrating single-cell
736 transcriptomic data across different conditions, technologies, and species. *Nat Biotechnol*
737 **36**, 411-420 (2018).
738 24. L. Velten *et al.*, Human haematopoietic stem cell lineage commitment is a continuous
739 process. *Nat Cell Biol* **19**, 271-281 (2017).
740 25. D. M. Popescu *et al.*, Decoding human fetal liver haematopoiesis. *Nature* **574**, 365-371
741 (2019).
742 26. S. Triana *et al.*, Single-cell proteo-genomic reference maps of the hematopoietic system
743 enable the purification and massive profiling of precisely defined cell states. *Nat Immunol*
744 **22**, 1577-1589 (2021).
745 27. S. B. Hay, K. Ferchen, K. Chetal, H. L. Grimes, N. Salomonis, The Human Cell Atlas bone
746 marrow single-cell interactive web portal. *Exp Hematol* **68**, 51-61 (2018).
747 28. B. Psaila *et al.*, Single-Cell Analyses Reveal Megakaryocyte-Biased Hematopoiesis in
748 Myelofibrosis and Identify Mutant Clone-Specific Targets. *Mol Cell* **78**, 477-492.e478
749 (2020).
750 29. A. Rodriguez-Meira *et al.*, Unravelling Intratumoral Heterogeneity through High-
751 Sensitivity Single-Cell Mutational Analysis and Parallel RNA Sequencing. *Mol Cell* **73**,
752 1292-1305.e1298 (2019).
753 30. D. Van Egeren *et al.*, Reconstructing the Lineage Histories and Differentiation Trajectories
754 of Individual Cancer Cells in Myeloproliferative Neoplasms. *Cell Stem Cell* **28**, 514-
755 523.e519 (2021).
756 31. T. E. Khoyratty *et al.*, Distinct transcription factor networks control neutrophil-driven
757 inflammation. *Nat Immunol* **22**, 1093-1106 (2021).
758 32. H. Hirai *et al.*, C/EBPbeta is required for 'emergency' granulopoiesis. *Nat Immunol* **7**, 732-
759 739 (2006).
760 33. S. A. Pawar *et al.*, C/EBPδ deficiency sensitizes mice to ionizing radiation-induced
761 hematopoietic and intestinal injury. *PLoS One* **9**, e94967 (2014).
762 34. V. Bergen, M. Lange, S. Peidli, F. A. Wolf, F. J. Theis, Generalizing RNA velocity to
763 transient cell states through dynamical modeling. *Nat Biotechnol* **38**, 1408-1414 (2020).
764 35. G. La Manno *et al.*, RNA velocity of single cells. *Nature* **560**, 494-498 (2018).
765 36. F. A. Wolf *et al.*, PAGA: graph abstraction reconciles clustering with trajectory inference
766 through a topology preserving map of single cells. *Genome Biol* **20**, 59 (2019).
767 37. R. H. Land *et al.*, The orphan nuclear receptor NR4A1 specifies a distinct subpopulation
768 of quiescent myeloid-biased long-term HSCs. *Stem Cells* **33**, 278-288 (2015).
769 38. P. R. Freire, O. M. Conneely, NR4A1 and NR4A3 restrict HSC proliferation via reciprocal
770 regulation of C/EBPα and inflammatory signaling. *Blood* **131**, 1081-1093 (2018).
771 39. F. Notta *et al.*, Distinct routes of lineage development reshape the human blood hierarchy
772 across ontogeny. *Science* **351**, aab2116 (2016).
773 40. I. García-García *et al.*, Pharmacokinetic and pharmacodynamic comparison of two
774 "pegylated" interferon alpha-2 formulations in healthy male volunteers: a randomized,
775 crossover, double-blind study. *BMC Pharmacol* **10**, 15 (2010).
776 41. D. Van Egeren *et al.*, Reconstructing the Lineage Histories and Differentiation Trajectories
777 of Individual Cancer Cells in Myeloproliferative Neoplasms. *Cell Stem Cell* **28**, 514-523
778 e519 (2021).

42. A. S. Nam *et al.*, Single-cell multi-omics of human clonal hematopoiesis reveals that DNMT3A R882 mutations perturb early progenitor states through selective hypomethylation. *Nat Genet*, (2022).
43. P. van Galen *et al.*, Single-Cell RNA-Seq Reveals AML Hierarchies Relevant to Disease Progression and Immunity. *Cell* **176**, 1265-1281.e1224 (2019).
44. I. Tirosh *et al.*, Dissecting the multicellular ecosystem of metastatic melanoma by single-cell RNA-seq. *Science* **352**, 189-196 (2016).
45. Y. Nie, Y. C. Han, Y. R. Zou, CXCR4 is required for the quiescence of primitive hematopoietic cells. *J Exp Med* **205**, 777-783 (2008).
46. F. Le Naour *et al.*, Upregulation of CD9 expression during TPA treatment of K562 cells. *Leukemia* **11**, 1290-1297 (1997).
47. D. Clay *et al.*, CD9 and megakaryocyte differentiation. *Blood* **97**, 1982-1989 (2001).
48. R. Månsson *et al.*, Molecular evidence for hierarchical transcriptional lineage priming in fetal and adult stem cells and multipotent progenitors. *Immunity* **26**, 407-419 (2007).
49. A. Sanjuan-Pla *et al.*, Platelet-biased stem cells reside at the apex of the haematopoietic stem-cell hierarchy. *Nature* **502**, 232-236 (2013).
50. S. O. Ciurea *et al.*, Pivotal contributions of megakaryocytes to the biology of idiopathic myelofibrosis. *Blood* **110**, 986-993 (2007).
51. H. Chagraoui *et al.*, Prominent role of TGF-beta 1 in thrombopoietin-induced myelofibrosis in mice. *Blood* **100**, 3495-3503 (2002).
52. S. Badalucco *et al.*, Involvement of TGFβ1 in autocrine regulation of proplatelet formation in healthy subjects and patients with primary myelofibrosis. *Haematologica* **98**, 514-517 (2013).
53. A. Ehninger *et al.*, Posttranscriptional regulation of c-Myc expression in adult murine HSCs during homeostasis and interferon-α-induced stress response. *Blood* **123**, 3909-3913 (2014).
54. M. N. Sharif *et al.*, Twist mediates suppression of inflammation by type I IFNs and Axl. *J Exp Medicine* **203**, 1891-1901 (2006).
55. T. Tashi *et al.*, Pegylated interferon Alfa-2a and hydroxyurea in polycythemia vera and essential thrombocythemia: differential cellular and molecular responses. *Leukemia* **32**, 1830-1833 (2018).
56. A. G. X. Zeng *et al.*, Identification of a human hematopoietic stem cell subset that retains memory of inflammatory stress. *bioRxiv*, 2023.2009.2011.557271 (2023).
57. S. Saeed *et al.*, Epigenetic programming of monocyte-to-macrophage differentiation and trained innate immunity. *Science* **345**, 1251086 (2014).
58. K. U. Belge *et al.*, The proinflammatory CD14+CD16+DR++ monocytes are a major source of TNF. *J Immunol* **168**, 3536-3542 (2002).
59. M. Frankenberger, T. Sternsdorf, H. Pechumer, A. Pforte, H. W. Ziegler-Heitbrock, Differential cytokine expression in human blood monocyte subpopulations: a polymerase chain reaction analysis. *Blood* **87**, 373-377 (1996).
60. E. M. Fast *et al.*, External signals regulate continuous transcriptional states in hematopoietic stem cells. *Elife* **10**, (2021).
61. A. E. Rodriguez-Fraticelli *et al.*, Clonal analysis of lineage fate in native haematopoiesis. *Nature* **553**, 212-216 (2018).

823 62. E. M. Pietras *et al.*, Chronic interleukin-1 exposure drives haematopoietic stem cells
824 towards precocious myeloid differentiation at the expense of self-renewal. *Nat Cell Biol*
825 **18**, 607-618 (2016).
826 63. K. A. Matatall, C. C. Shen, G. A. Challen, K. Y. King, Type II interferon promotes
827 differentiation of myeloid-biased hematopoietic stem cells. *Stem Cells* **32**, 3023-3030
828 (2014).
829 64. M. Yamashita, E. Passegué, TNF-α Coordinates Hematopoietic Stem Cell Survival and
830 Myeloid Regeneration. *Cell Stem Cell*, (2019).
831 65. K. A. Lord, A. Abdollahi, B. Hoffman-Liebermann, D. A. Liebermann, Proto-oncogenes
832 of the fos/jun family of transcription factors are positive regulators of myeloid
833 differentiation. *Mol Cell Biol* **13**, 841-851 (1993).
834 66. T. I. Lee *et al.*, Transcriptional regulatory networks in Saccharomyces cerevisiae. *Science*
835 **298**, 799-804 (2002).
836 67. X. Y. Li *et al.*, The role of chromatin accessibility in directing the widespread, overlapping
837 patterns of Drosophila transcription factor binding. *Genome Biol* **12**, R34 (2011).
838 68. R. Pique-Regi *et al.*, Accurate inference of transcription factor binding from DNA
839 sequence and chromatin accessibility data. *Genome Res* **21**, 447-455 (2011).
840 69. A. N. Schep, B. Wu, J. D. Buenrostro, W. J. Greenleaf, chromVAR: inferring transcription-
841 factor-associated accessibility from single-cell epigenomic data. *Nat Methods* **14**, 975-978
842 (2017).
843 70. J. D. Buenrostro *et al.*, Single-cell chromatin accessibility reveals principles of regulatory
844 variation. *Nature* **523**, 486-490 (2015).
845 71. J. T. Gaublomme *et al.*, Nuclei multiplexing with barcoded antibodies for single-nucleus
846 genomics. *Nat Commun* **10**, 2907 (2019).
847 72. S. Ma *et al.*, Chromatin Potential Identified by Shared Single-Cell Profiling of RNA and
848 Chromatin. *Cell* **183**, 1103-1116.e1120 (2020).
849 73. W. Reith *et al.*, MHC class II regulatory factor RFX has a novel DNA-binding domain and
850 a functionally independent dimerization domain. *Genes Dev* **4**, 1528-1540 (1990).
851 74. L. Pugliatti *et al.*, The genes for MHC class II regulatory factors RFX1 and RFX2 are
852 located on the short arm of chromosome 19. *Genomics* **13**, 1307-1310 (1992).
853 75. C. A. Siegrist, B. Mach, Antisense oligonucleotides specific for regulatory factor RFX-1
854 inhibit inducible but not constitutive expression of all major histocompatibility complex
855 class II genes. *Eur J Immunol* **23**, 2903-2908 (1993).
856 76. P. Burda, P. Laslo, T. Stopka, The role of PU.1 and GATA-1 transcription factors during
857 normal and leukemogenic hematopoiesis. *Leukemia* **24**, 1249-1257 (2010).
858 77. M. A. Hall *et al.*, The critical regulator of embryonic hematopoiesis, SCL, is vital in the
859 adult for megakaryopoiesis, erythropoiesis, and lineage choice in CFU-S12. *Proc Natl*
860 *Acad Sci U S A* **100**, 992-997 (2003).
861 78. C. L. Semerad, E. M. Mercer, M. A. Inlay, I. L. Weissman, C. Murre, E2A proteins
862 maintain the hematopoietic stem cell pool and promote the maturation of myelolymphoid
863 and myeloerythroid progenitors. *Proc Natl Acad Sci U S A* **106**, 1930-1935 (2009).
864 79. Y. Zhuang, P. Cheng, H. Weintraub, B-lymphocyte development is regulated by the
865 combined dosage of three basic helix-loop-helix genes, E2A, E2-2, and HEB. *Mol Cell*
866 *Biol* **16**, 2898-2905 (1996).

867 80. D. E. Zhang *et al.*, Absence of granulocyte colony-stimulating factor signaling and
868 neutrophil development in CCAAT enhancer binding protein alpha-deficient mice. *Proc*
869 *Natl Acad Sci U S A* **94**, 569-574 (1997).
870 81. H. S. Radomska *et al.*, CCAAT/enhancer binding protein alpha is a regulatory switch
871 sufficient for induction of granulocytic development from bipotential myeloid progenitors.
872 *Mol Cell Biol* **18**, 4301-4314 (1998).
873 82. S. Marecki, C. J. Riendeau, M. D. Liang, M. J. Fenton, PU.1 and multiple IFN regulatory
874 factor proteins synergize to mediate transcriptional activation of the human IL-1 beta gene.
875 *J Immunol* **166**, 6829-6838 (2001).
876 83. W. Huang, E. Horvath, E. A. Eklund, PU.1, interferon regulatory factor (IRF) 2, and the
877 interferon consensus sequence-binding protein (ICSBP/IRF8) cooperate to activate NF1
878 transcription in differentiating myeloid cells. *J Biol Chem* **282**, 6629-6643 (2007).
879 84. M. Hoogenkamp *et al.*, Early chromatin unfolding by RUNX1: a molecular explanation
880 for differential requirements during specification versus maintenance of the hematopoietic
881 gene expression program. *Blood* **114**, 299-309 (2009).
882 85. C. Yeamans *et al.*, C/EBPalpha binds and activates the PU.1 distal enhancer to induce
883 monocyte lineage commitment. *Blood* **110**, 3136-3142 (2007).
884 86. C. Le Coz *et al.*, Constrained chromatin accessibility in PU.1-mutated
885 agammaglobulinemia patients. *J Exp Med* **218**, (2021).
886 87. P. Gutierrez, M. D. Delgado, C. Richard, F. Moreau-Gachelin, J. Leon, Interferon induces
887 up-regulation of Spi-1/PU.1 in human leukemia K562 cells. *Biochem Biophys Res*
888 *Commun* **240**, 862-868 (1997).
889 88. H. Stein *et al.*, A new monoclonal antibody (CAL2) detects CALRETICULIN mutations
890 in formalin-fixed and paraffin-embedded bone marrow biopsies. *Leukemia* **30**, 131-135
891 (2016).
892 89. S. Cuylen *et al.*, Ki-67 acts as a biological surfactant to disperse mitotic chromosomes.
893 *Nature* **535**, 308-312 (2016).
894 90. J. S. Jutzi *et al.*, Whole-genome CRISPR screening identifies N-glycosylation as a genetic
895 and therapeutic vulnerability in CALR-mutant MPNs. *Blood* **140**, 1291-1304 (2022).
896 91. D. Prins *et al.*, The stem/progenitor landscape is reshaped in a mouse model of essential
897 thrombocythemia and causes excess megakaryocyte production. *Sci Adv* **6**, (2020).
898 92. P. J. Skene, S. Henikoff, An efficient targeted nuclease strategy for high-resolution
899 mapping of DNA binding sites. *Elife* **6**, (2017).
900 93. S. Elf *et al.*, Mutant Calreticulin Requires Both Its Mutant C-terminus and the
901 Thrombopoietin Receptor for Oncogenic Transformation. *Cancer Discov* **6**, 368-381
902 (2016).
903 94. A. L. Brass, E. Kehrli, C. F. Eisenbeis, U. Storb, H. Singh, Pip, a lymphoid-restricted IRF,
904 contains a regulatory domain that is important for autoinhibition and ternary complex
905 formation with the Ets factor PU.1. *Genes Dev* **10**, 2335-2347 (1996).
906 95. J. M. Pongubala *et al.*, Effect of PU.1 phosphorylation on interaction with NF-EM5 and
907 transcriptional activation. *Science* **259**, 1622-1625 (1993).
908 96. S. Heinz *et al.*, Simple combinations of lineage-determining transcription factors prime
909 cis-regulatory elements required for macrophage and B cell identities. *Mol Cell* **38**, 576-
910 589 (2010).
911 97. C. Kopanos *et al.*, VarSome: the human genomic variant search engine. *Bioinformatics* **35**,
912 1978-1980 (2019).

913 98. F. Hu *et al.*, ER stress and its regulator X-box-binding protein-1 enhance polyIC-induced
914 innate immune response in dendritic cells. *Eur J Immunol* **41**, 1086-1097 (2011).
915 99. M. G. Netea, J. Quintin, J. W. van der Meer, Trained immunity: a memory for innate host
916 defense. *Cell Host Microbe* **9**, 355-361 (2011).
917 100. S. Naik *et al.*, Inflammatory memory sensitizes skin epithelial stem cells to tissue damage.
918 *Nature* **550**, 475-480 (2017).
919 101. I. Gresser, C. Bourali, Exogenous interferon and inducers of interferon in the treatment
920 Balb-c mice inoculated with RC19 tumour cells. *Nature* **223**, 844-845 (1969).
921 102. N. Tweezer-Zaks, E. Rabinovich, M. Lidar, A. Livneh, Interferon-alpha as a treatment
922 modality for colchicine- resistant familial Mediterranean fever. *J Rheumatol* **35**, 1362-1365
923 (2008).
924 103. S. L. Hauser *et al.*, Ocrelizumab versus Interferon Beta-1a in Relapsing Multiple Sclerosis.
925 *N Engl J Med* **376**, 221-234 (2017).
926 104. E. Aricò, L. Castiello, I. Capone, L. Gabriele, F. Belardelli, Type I Interferons and Cancer:
927 An Evolving Story Demanding Novel Clinical Applications. *Cancers (Basel)* **11**, (2019).
928 105. N. G. Sandler *et al.*, Type I interferon responses in rhesus macaques prevent SIV infection
929 and slow disease progression. *Nature* **511**, 601-605 (2014).
930 106. V. Suppiah *et al.*, IL28B is associated with response to chronic hepatitis C interferon-alpha
931 and ribavirin therapy. *Nat Genet* **41**, 1100-1104 (2009).
932 107. G. Schreiber, The Role of Type I Interferons in the Pathogenesis and Treatment of COVID-
933 19. *Front Immunol* **11**, 595739 (2020).
934 108. I. A. Darazam *et al.*, Role of interferon therapy in severe COVID-19: the COVIFERON
935 randomized controlled trial. *Sci Rep-uk* **11**, 8059 (2021).
936 109. J. J. Kiladjian *et al.*, Long-term outcomes of polycythemia vera patients treated with
937 ropeginterferon Alfa-2b. *Leukemia* **36**, 1408-1411 (2022).
938 110. L. Huys *et al.*, Type I interferon drives tumor necrosis factor-induced lethal shock. *J Exp*
939 *Med* **206**, 1873-1882 (2009).
940 111. J. Hadjadj *et al.*, Impaired type I interferon activity and inflammatory responses in severe
941 COVID-19 patients. *Science* **369**, 718-724 (2020).
942 112. Q. Zhang *et al.*, Inborn errors of type I IFN immunity in patients with life-threatening
943 COVID-19. *Science* **370**, eabd4570 (2020).
944 113. M. Ohta, J. S. Greenberger, P. Anklesaria, A. Bassols, J. Massagué, Two forms of
945 transforming growth factor-beta distinguished by multipotential haematopoietic progenitor
946 cells. *Nature* **329**, 539-541 (1987).
947 114. S. J. Stein, A. S. Baldwin, Deletion of the NF-κB subunit p65/RelA in the hematopoietic
948 compartment leads to defects in hematopoietic stem cell function. *Blood* **121**, 5015-5024
949 (2013).
950 115. M. Zhao *et al.*, Megakaryocytes maintain homeostatic quiescence and promote post-injury
951 regeneration of hematopoietic stem cells. *Nat Med* **20**, 1321-1326 (2014).
952 116. J. M. Scandura, P. Boccuni, J. Massagué, S. D. Nimer, Transforming growth factor beta-
953 induced cell cycle arrest of human hematopoietic cells requires p57KIP2 up-regulation.
954 *Proc Natl Acad Sci U S A* **101**, 15231-15236 (2004).
955 117. A. Mullally *et al.*, Depletion of Jak2V617F myeloproliferative neoplasm-propagating stem
956 cells by interferon-α in a murine model of polycythemia vera. *Blood* **121**, 3692-3702
957 (2013).

958 118. S. Haas *et al.*, Inflammation-Induced Emergency Megakaryopoiesis Driven by
959 Hematopoietic Stem Cell-like Megakaryocyte Progenitors. *Cell Stem Cell* **17**, 422-434
960 (2015).
961 119. N. Khan *et al.*, M. tuberculosis Reprograms Hematopoietic Stem Cells to Limit
962 Myelopoiesis and Impair Trained Immunity. *Cell* **183**, 752-770.e722 (2020).
963 120. Y. Ueda, D. W. Cain, M. Kuraoka, M. Kondo, G. Kelsoe, IL-1R type I-dependent
964 hemopoietic stem cell proliferation is necessary for inflammatory granulopoiesis and
965 reactive neutrophilia. *J Immunol* **182**, 6477-6484 (2009).
966 121. C. Chen, Y. Liu, P. Zheng, Mammalian target of rapamycin activation underlies HSC
967 defects in autoimmune disease and inflammation in mice. *J Clin Invest* **120**, 4091-4101
968 (2010).
969 122. K. Akashi, D. Traver, T. Miyamoto, I. L. Weissman, A clonogenic common myeloid
970 progenitor that gives rise to all myeloid lineages. *Nature* **404**, 193-197 (2000).
971 123. M. Kondo, I. L. Weissman, K. Akashi, Identification of clonogenic common lymphoid
972 progenitors in mouse bone marrow. *Cell* **91**, 661-672 (1997).
973 124. J. Adolfsson *et al.*, Identification of Flt3+ lympho-myeloid stem cells lacking erythro-
974 megakaryocytic potential a revised road map for adult blood lineage commitment. *Cell*
975 **121**, 295-306 (2005).
976 125. J. M. Granja *et al.*, Single-cell multiomic analysis identifies regulatory programs in mixed-
977 phenotype acute leukemia. *Nat Biotechnol* **37**, 1458-1465 (2019).
978 126. Y. Hao *et al.*, Integrated analysis of multimodal single-cell data. *Cell* **184**, 3573-
979 3587.e3529 (2021).
980 127. T. Stuart *et al.*, Comprehensive Integration of Single-Cell Data. *Cell* **177**, 1888-1902.e1821
981 (2019).
982 128. L. McInnes, J. Healy, J. Melville. (Cornell University, UMAP: Uniform Manifold
983 Approximation and Projection for Dimension Reduction. *arXiv preprint*
984 *arXiv:1802.03426*, 2018).
985 129. T. Smith, A. Heger, I. Sudbery, UMI-tools: modeling sequencing errors in Unique
986 Molecular Identifiers to improve quantification accuracy. *Genome Res* **27**, 491-499 (2017).
987 130. B. M. Bolker *et al.*, Generalized linear mixed models: a practical guide for ecology and
988 evolution. *Trends Ecol Evol* **24**, 127-135 (2009).
989 131. V. Ntranos, L. Yi, P. Melsted, L. Pachter, A discriminative learning approach to differential
990 expression analysis for single-cell RNA-seq. *Nat Methods* **16**, 163-166 (2019).
991 132. I. Dolgalev. (msigdbr: MSigDB Gene Sets for Multiple Organisms in a Tidy Data Format.
992 (Manual 2022), https://igordot.github.io/msigdbr/, 2022).
993 133. G. Korotkevich *et al.*, in *Fast gene set enrichment analysis,* bioRxiv, Ed.
994 (doi: https://doi.org/10.1101/060012, 2021).
995 134. A. Liberzon *et al.*, The Molecular Signatures Database (MSigDB) hallmark gene set
996 collection. *Cell Syst* **1**, 417-425 (2015).
997 135. T. Stuart, A. Srivastava, S. Madad, C. A. Lareau, R. Satija, Single-cell chromatin state
998 analysis with Signac. *Nat Methods* **18**, 1333-1341 (2021).
999 136. Y. Zhang *et al.*, Model-based analysis of ChIP-Seq (MACS). *Genome Biol* **9**, R137 (2008).
1000 137. M. T. Weirauch *et al.*, Determination and inference of eukaryotic transcription factor
1001 sequence specificity. *Cell* **158**, 1431-1443 (2014).

138. A. T. Satpathy *et al.*, Massively parallel single-cell chromatin landscapes of human immune cell development and intratumoral T cell exhaustion. *Nat Biotechnol* **37**, 925-936 (2019).
139. X. Qiu *et al.*, Reversed graph embedding resolves complex single-cell trajectories. *Nat Methods* **14**, 979-982 (2017).
140. J. Cao *et al.*, The single-cell transcriptional landscape of mammalian organogenesis. *Nature* **566**, 496-502 (2019).
141. A. P. Masella *et al.*, BAMQL: a query language for extracting reads from BAM files. *BMC Bioinformatics* **17**, 305 (2016).
142. C. E. Grant, T. L. Bailey, W. S. Noble, FIMO: scanning for occurrences of a given motif. *Bioinformatics* **27**, 1017-1018 (2011).
143. A. V. Persikov *et al.*, A systematic survey of the Cys2His2 zinc finger DNA-binding landscape. *Nucleic Acids Res* **43**, 1965-1984 (2015).
144. J. J. van Dongen *et al.*, EuroFlow antibody panels for standardized n-dimensional flow cytometric immunophenotyping of normal, reactive and malignant leukocytes. *Leukemia* **26**, 1908-1975 (2012).
145. T. Kalina *et al.*, EuroFlow standardization of flow cytometer instrument settings and immunophenotyping protocols. *Leukemia* **26**, 1986-2010 (2012).
146. S. White *et al.*, FlowKit: A Python Toolkit for Integrated Manual and Automated Cytometry Analysis Workflows. *Front Immunol* **12**, 768541 (2021).
147. C. D. Carey *et al.*, Topological analysis reveals a PD-L1-associated microenvironmental niche for Reed-Sternberg cells in Hodgkin lymphoma. *Blood* **130**, 2420-2430 (2017).
148. S. S. Patel *et al.*, Multiparametric in situ imaging of NPM1-mutated acute myeloid leukemia reveals prognostically-relevant features of the marrow microenvironment. *Mod Pathol* **33**, 1380-1388 (2020).
149. J. Rosenthal *et al.*, Building Tools for Machine Learning and Artificial Intelligence in Cancer Research: Best Practices and a Case Study with the PathML Toolkit for Computational Pathology. *Mol Cancer Res* **20**, 202-206 (2022).
150. N. F. Greenwald *et al.*, Whole-cell segmentation of tissue images with human-level performance using large-scale data annotation and deep learning. *Nat Biotechnol* **40**, 555-565 (2022).
151. A. M. Bolger, M. Lohse, B. Usadel, Trimmomatic: a flexible trimmer for Illumina sequence data. *Bioinformatics* **30**, 2114-2120 (2014).
152. B. Langmead, S. L. Salzberg, Fast gapped-read alignment with Bowtie 2. *Nat Methods* **9**, 357-359 (2012).
153. H. Li *et al.*, The Sequence Alignment/Map format and SAMtools. *Bioinformatics* **25**, 2078-2079 (2009).
154. M. Bale. (GitHub).
155. T. L. Bailey, C. E. Grant. (BioRxiv, 2021).
156. F. Ramírez *et al.*, deepTools2: a next generation web server for deep-sequencing data analysis. *Nucleic Acids Res* **44**, W160-165 (2016).
157. M. I. Love, W. Huber, S. Anders, Moderated estimation of fold change and dispersion for RNA-seq data with DESeq2. *Genome Biol* **15**, 550 (2014).

Acknowledgments

We thank patients who participated in the MPN-RC-111/2 clinical trials and patients at WCM, who generously donated samples that enabled this research. This work was enabled by the Weill Cornell Epigenomics Core, Genomics Core and Flow Cytometry Core. We thank Dr. Matthew Greenblatt and Dr. Steven Josefowicz (Weill Cornell Medicine) and Dr. Serine Avagyan (University of California, San Francisco) for a critical review of the manuscript. We also thank the funding sources that supported this work:

F30 Predoctoral Fellowship from the NHLBI of the National Institutes of Health (F30HL156496, ND)
Medical Scientist Training Program grant from the National Institute of General Medical Sciences of the National Institutes of Health under award number T32GM152349 to the Weill Cornell/Rockefeller/Sloan Kettering Tri-Institutional MD-PhD Program (DI, ND)
National Institute of Health grant (P01CA108671, RH)
Burroughs Wellcome Fund Career Award for Medical Scientists (ASN)
National Institutes of Health Director's Early Independence Award (DP5 OD029619, ASN)
National Heart Lung and Blood Institute (R01 HL167139, ASN),
Starr Cancer Consortium (ASN)

Author contributions

Conceptualization: ASN, RH
Methodology: ASN, RH, SP, DAL, PS, EW, LM
Experimental investigation: DI, SR, OS, MSS, RC, NO, MT, MQ, GF
Analytical investigation: ASN, CL, AKM, AXX, SM, NP, MO, AD, PS, PC, HEK, ND, TA, ACD
Funding acquisition: ASN, RH
Project administration: ASN, RH
Resources: ASN, RH, RW, DC, FCT, GAZ, EW, BM
Supervision: ASN, RH
Writing – original draft: ASN, CL, DI
Writing – review & editing: ASN, RH, CL, DI, OS, SR, MT, MSS
All authors reviewed and approved the manuscript.

Competing interests

R.H. serves as a consultant to Protagonist, Ionis and Silence Therapeutics and receives research support unrelated to the current study from Dompe, Scholar Rock, Incyte, Novartis, Kartos, Turning Point Therapeutics, Abbvie and Oncomyx. D.A.L. has served as a consultant for Abbvie and Illumina and is on the Scientific Advisory Board of Mission Bio and C2i Genomics; D.A.L. has received prior research funding from BMS and Illumina unrelated to the current manuscript.

Data and Code Availability: Data generated in this study will be available upon publication.

1085 **Corresponding author:** Anna S. Nam.

1086 **Correspondence and requests for materials** should be addressed to A.S.N.

List of Supplementary Materials

Materials and Methods
Figs. S1 to S14
Tables S1 to S31 (Tables S1-S31 provided as xlsx files)
List of references only cited in Supplementary Materials: 131-163

1093 **Figures**

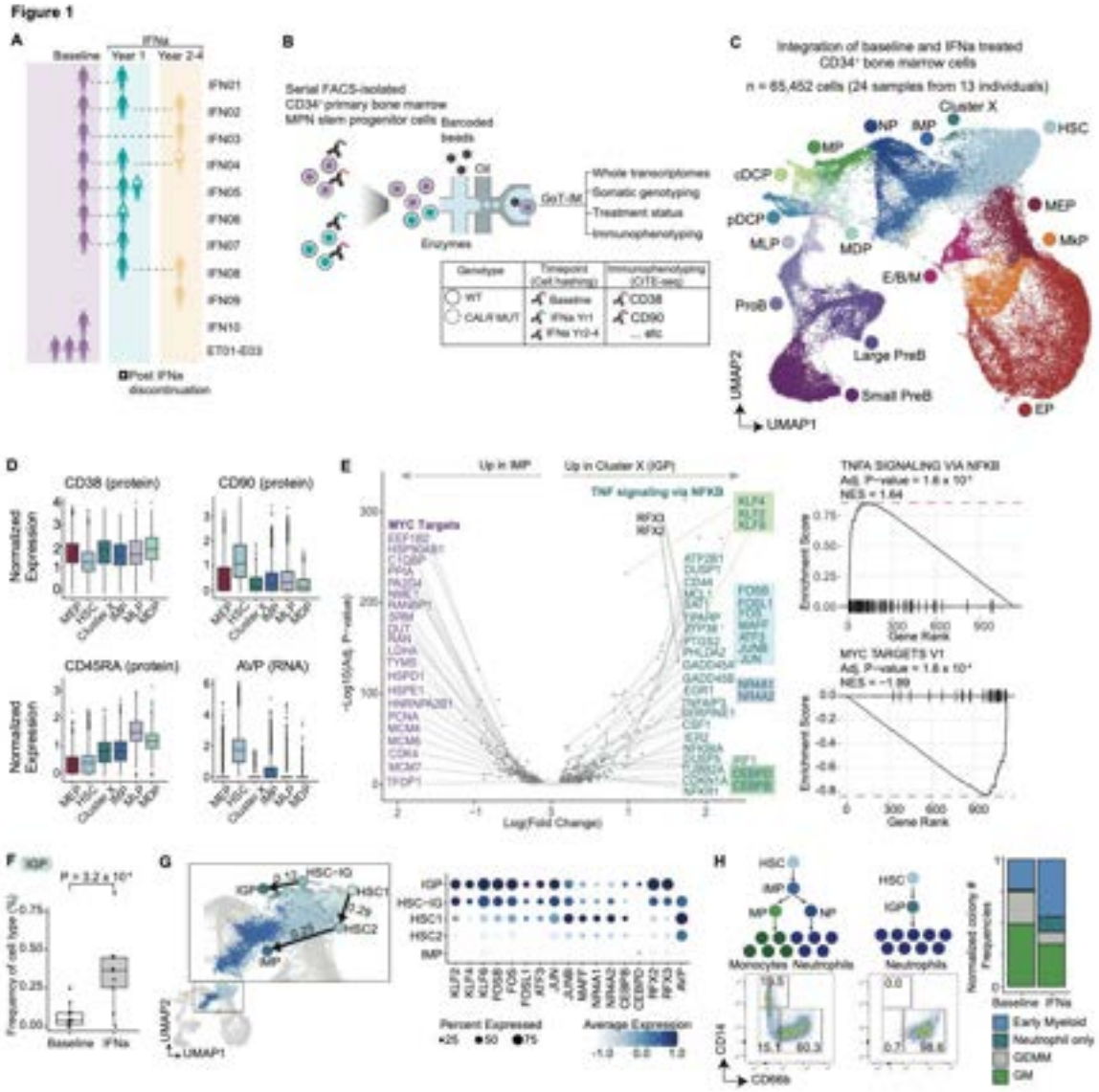

1094

1095 **Figure 1. Integration of Genotyping of Transcriptomes with immunophenotyping and IFNα-**
1096 **treatment status identifies an alternate IFNα-specific cell state in MPN stem and progenitor**
1097 **cells. A.** Primary bone marrow samples at baseline and after IFNα treatment included for
1098 Genotyping of Transcriptomes with Immunophenotyping (GoT-IM) on $CD34^+$ cells. **B.** Schematic
1099 of GoT-IM via CITE-seq and Cell Hashing. MPN, myeloproliferative neoplasms; WT, wildtype;
1100 MUT, mutated. **C.** Uniform manifold approximation and projection (UMAP) of $CD34^+$ cells (n =
1101 65,452 cells) from MPN samples (n = 24 samples from 13 individuals), overlaid with cell type
1102 assignment. HSC, hematopoietic stem cells; IMP, immature myeloid progenitors; NP, neutrophilic
1103 progenitors; MP, monocytic progenitors; cDCP, classic dendritic progenitors; pDCP, plasmacytoid
1104 dendritic progenitors; MDP, monocytic dendritic progenitors; MLP, multipotent lymphoid
1105 progenitors; E/B/M, eosinophil/basophil/mast cell progenitors; MkP, megakaryocytic progenitors;
1106 EP, erythroid progenitors; MEP, megakaryocytic-erythroid progenitors. **D.** Box plots showing
1107 normalized expression of HSC-defining protein and RNA markers. **E.** Volcano plot showing genes

1108 differentially expressed (DE) between Cluster X (i.e., IGPs) and IMPs identified via linear mixed
1109 modeling (LMM) with/without cluster identity (left, **methods**). Highlighted are genes enriched in
1110 the MYC pathway (purple) and TNFα signaling via NF-κB (blue); Boxes represent transcription
1111 factors (TF) of the AP-1 (blue), KLF (light green), NR4A (purple), CEBP (dark green) families.
1112 Pre-ranked gene set enrichment analysis using the MSigDB Hallmark collection (right). **F.** Box
1113 plot showing normalized IGP frequency at baseline and IFNα treatment (n = 11 baseline samples,
1114 n = 9 treated samples). P-values from likelihood ratio test of LMM with/without IFNα treatment
1115 (**methods**). **G.** Integrated UMAP highlighting IGP, IMP and the HSC subclusters with RNA
1116 velocity-based cell state trajectory for IFNα-treated cells (left, trajectory presented corresponds
1117 only to IMP, IGP and the HSC subclusters, see **table S5, methods**). Dot plot showing gene
1118 expression levels of upregulated TFs in IGPs (right). **H.** Representative flow cytometric analysis
1119 of colonies from the single-cell differentiation of individually sorted $CD34^+$, $CD90^+$ HSCs (left).
1120 Normalized colony frequency from HSCs sorted from bone marrow samples from patients at
1121 baseline and following IFNα (right, n = 2 baseline; n = 3 IFNα-treated). The number of colonies
1122 were down-sampled to the same minimum count for each replicate for equal representation.
1123 GEMM, granulocyte, erythrocyte, monocyte and megakaryocyte; GM, granulocyte-monocyte
1124 colonies .

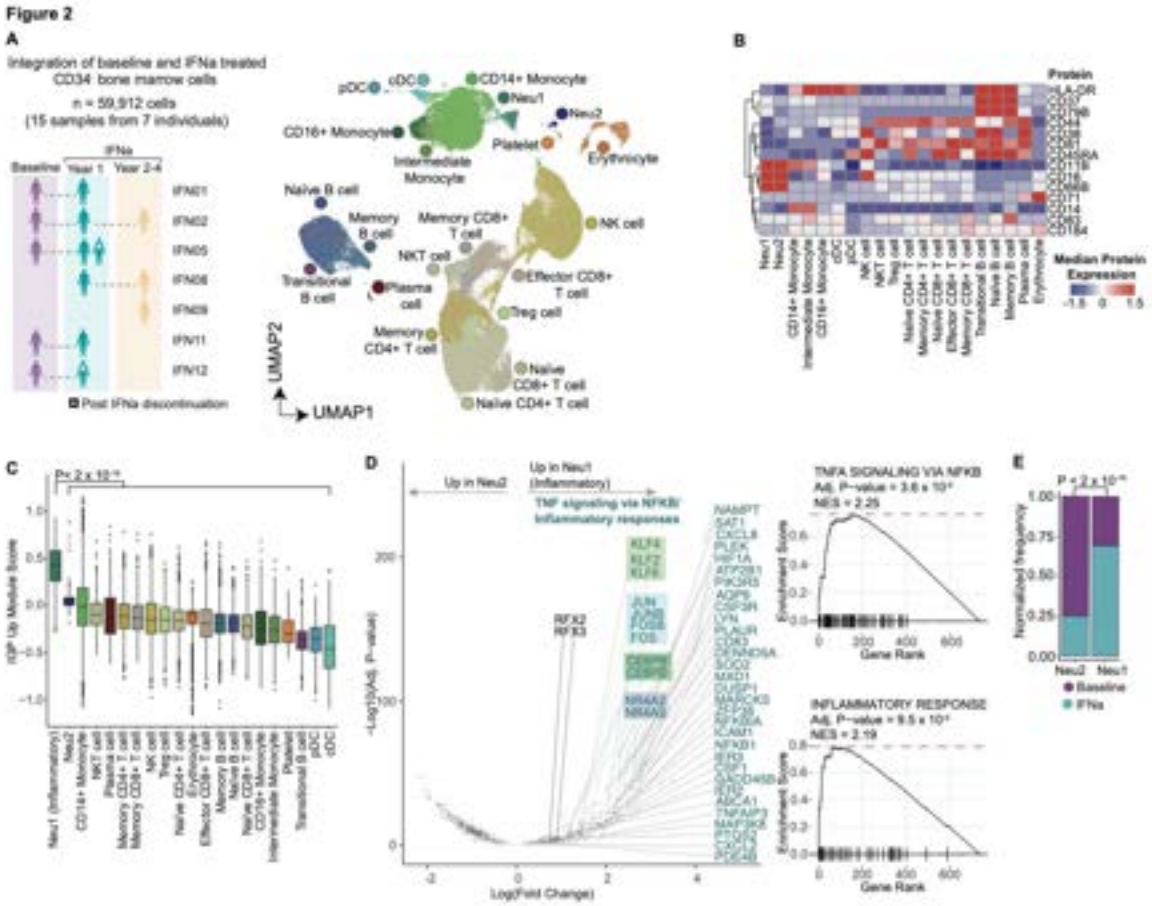

Figure 2. Inflammatory neutrophils are enriched in IFNα-treated bone marrow. A. Primary bone marrow samples at baseline and after IFNα treatment included in GoT-IM on CD34$^-$ cells (left). UMAP of CD34$^-$ cells (n = 59,912 cells; 15 samples from 7 individuals), overlaid with cell type assignment (right). Neu1, Neutrophil subset 1; Neu2, Neutrophil subset 2; cDC, classic dendritic cells; pDC, plasmacytoid dendritic cells, Treg cell; Regulatory T cells, NKT cells; Natural Killer T cells. **B.** Heatmap showing median scaled expression of canonical immune cell protein markers from a representative patient IFN12. **C.** Box plots showing IGP-specific upregulated signature score (**Fig. 1E, table S3**) in CD34$^-$ cell type clusters. P-value from likelihood ratio test of linear-mixed modeling (LMM) with/without cluster identity (**methods**). **D.** Volcano plot showing genes differentially expressed (DE) between Neu1 and Neu2 identified via LMM with/without cluster identity (left, **methods**). Highlighted are genes enriched in the TNFα signaling via NF-κB (blue, box representation is same as **Fig. 1E**). Pre-ranked gene set enrichment analysis using the MSigDB Hallmark collection (right). **E.** Normalized frequency of baseline and IFNα-treated cells in Neu1 and Neu2 subsets. P-value from Fisher's exact test, two-sided.

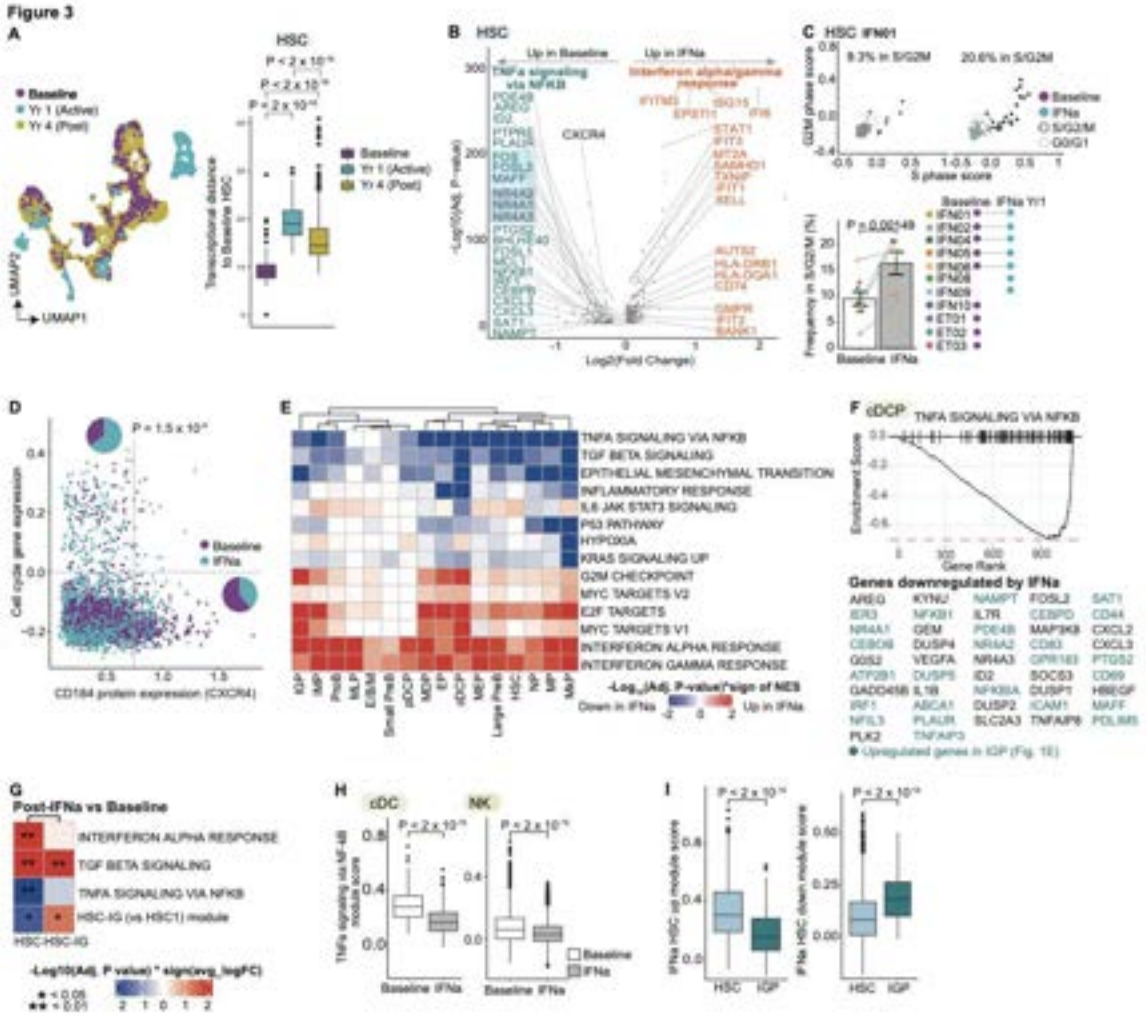

Figure 3. IFNα concurrently regulates anti- and pro-inflammatory programs. A. UMAP showing a representative experiment that includes three time-points from patient IFN04 (n = 7,282 cells, left). Box plot showing transcriptional distance measurements between HSCs from each time-point and HSCs from baseline (right). Transcriptional distance corresponds to Euclidean distance of the first thirty principal components. P-values from Wilcoxon rank sum test, two-sided. **B.** Volcano plot showing genes differentially expressed (DE) between baseline and IFNα-treated HSCs via linear mixed modeling (LMM) with/without treatment status (**methods**). Genes highlighted in blue are those in the TNFα signaling via NF-κB and those in orange enriched in the IFNα/γ response, identified by pre-ranked gene set enrichment analysis using the MSigDB Hallmark collection; box representation is same as **Fig. 1E**. **C.** Cell cycle gene expression (representative patient IFN01, n = 97 baseline and 97 IFNα-treated HSCs, top). Frequencies of cells in S/G2/M phase as assessed in top subpanel at baseline (n = 11 samples) and at year 1 of IFNα treatment (n = 9 samples). For IFN05 which has two IFNα year 1 samples, the active IFNα time-point was selected. P-values from likelihood ratio test of LMM with/without treatment status (**methods**). **D.** CXCR4 vs. cell cycle gene expression in HSCs before and after IFNα treatment. Pie charts show frequencies of baseline versus treated cells in cell cycle-low, CXCR4-high and those in cell cycle-high, CXCR4-low populations. P-value from two-sided Fisher's exact test. **E.**

1158 Heatmap showing results of the pre-ranked gene set enrichment analysis comparing baseline and
1159 during IFNα treatment across HSC and progenitor subsets. Values show the sign of the normalized
1160 enrichment score (NES) multiplied by -log10(Adjusted P-value). **F.** Pre-ranked gene set
1161 enrichment analysis comparing before and after treatment with IFNα in cDCPs, showing
1162 downregulation of TNFα signaling via NF-κB and the leading-edge genes. Genes highlighted in
1163 blue represent those upregulated in the IGP versus IMP (**table S3**, **Fig. 1E**). **G.** Heatmap showing
1164 results of the pre-ranked gene set enrichment analysis comparing baseline and upon IFNα
1165 treatment discontinuation in HSCs (combined HSC1 and HSC2 subsets from **Fig. 1G**) and HSC-
1166 IGs. Values show the sign of the normalized enrichment score (NES) multiplied by -
1167 log10(Adjusted P-value). HSC-IG (vs HSC1) module was calculated using net score of genes
1168 upregulated and downregulated in HSC-IG (**table S3**). **H.** Boxplot showing module expression for
1169 genes involved in TNFα signaling via NF-κB at baseline and during IFNα treatment in cDCs (left)
1170 and NK cells (right). P-value from likelihood ratio test of LMM with/without treatment status. **I.**
1171 Box plots showing HSC-specific IFNα-induced signature score in IFNα-treated HSCs and IGPs
1172 (**methods**). Score calculated using upregulated (left) or downregulated (right) genes (**table S8**). P-
1173 values from likelihood ratio tests of LMM with/without cell type.

1174

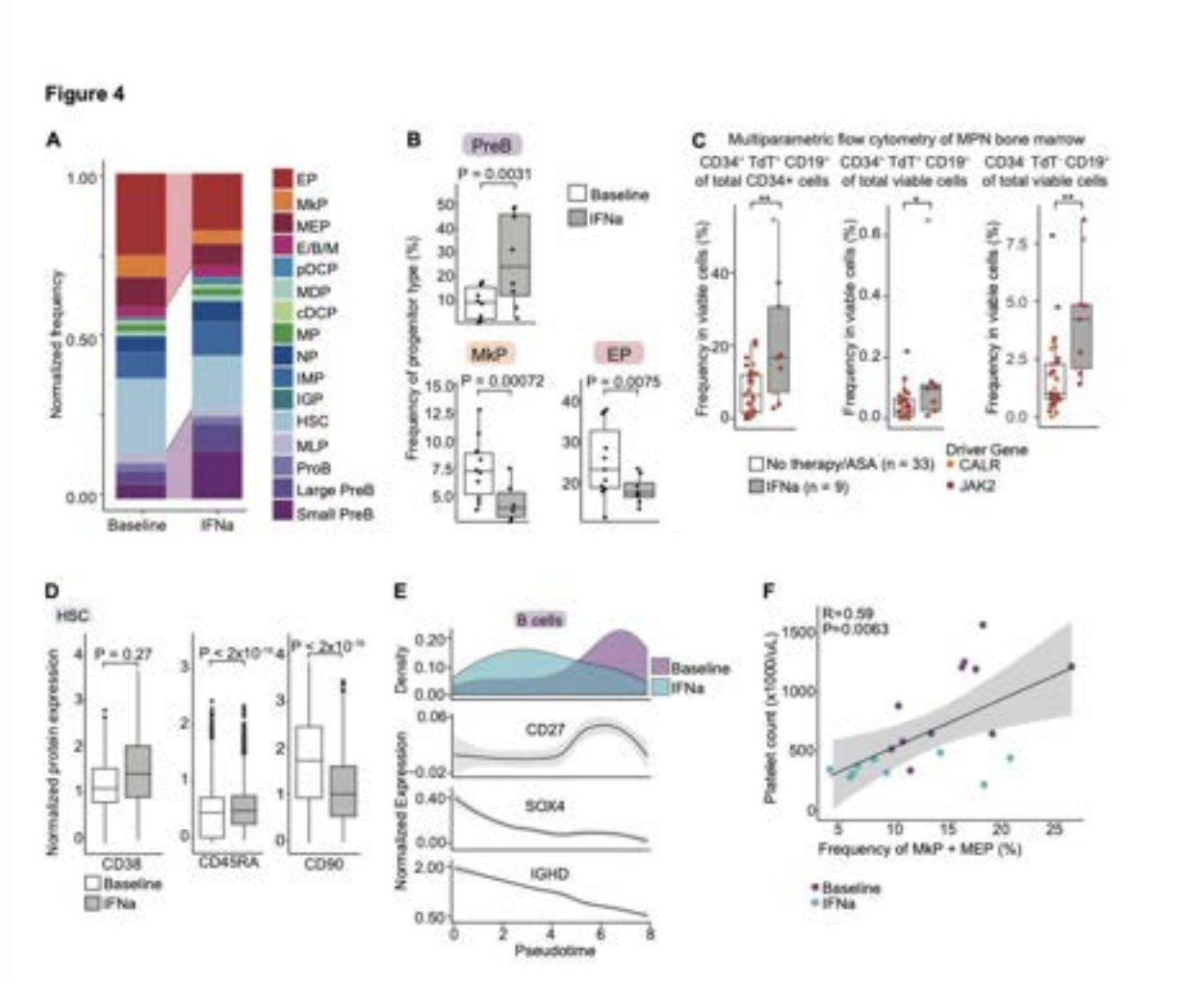

Figure 4. IFNα induces IGP and lymphoid differentiation. A. Normalized cell type frequencies at baseline and IFNα treatment. Cells from each sample were down-sampled to the same number (n = 500 cells from each sample, n = 11 baseline samples, n = 9 treated samples). For IFN02, IFN04, IFN05 and IFN08, which have two treated time-points, the time-point powered with greater number of cells was selected (also for panels **B, D**). **B.** Box plot showing normalized cell type frequencies at baseline and IFNα treatment (n = 11 baseline samples, n = 9 treated samples). P-values from likelihood ratio test of linear-mixed modeling (LMM) with/without treatment status. **C.** Box plots showing cell frequencies of B-lymphoid progenitors and B cells from bone marrow of patients with early stage MPN with no treatment or aspirin only (ASA) or with IFNα therapy (n = 33 and 9 samples, respectively), as determined by multiparametric flow cytometry (**table S12**). P-values from Wilcoxon rank sum test, two-sided. **D.** Box plots showing normalized protein expression in HSCs before and after treatment with IFNα. P-values from likelihood ratio tests of LMM with/without treatment status (**methods**). **E.** Gene expression of canonical B cell differentiation markers across immature and mature B cells in lymphoid development between baseline and IFNα-treated cells. **F.** Platelet counts versus frequencies of MEPs and MkPs. P-value from generalized linear model; Pearson correlation, shading denotes 95% confidence interval.

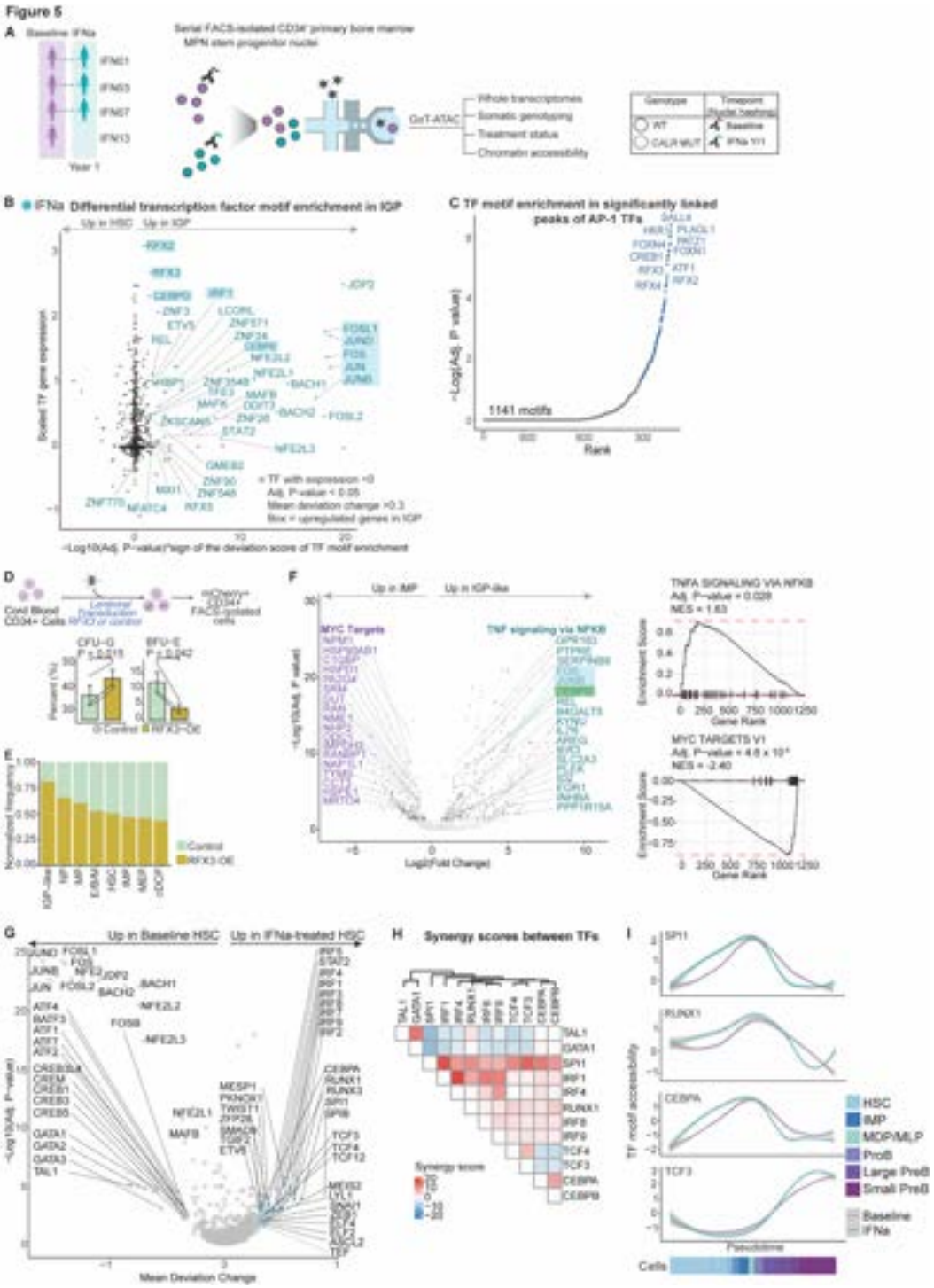

Figure 5. Regulatory networks of IGPs highlight PU.1 as the master regulator of IFNα-mediated remodeling of hematopoiesis. A. Representation of primary bone marrow samples at baseline and after IFNα treatment (left). Schematic of GoT-ATAC (right). **B.** Motif enrichment

1198 and expression of transcription factors (TF) in the IGPs relative to HSCs from IFNα-treated
1199 samples. Normalized gene expression derived from GoT-IM data within HSCs and IGPs. P-values
1200 from Wilcoxon rank sum test, two-sided, with Benjamini-Hochberg FDR-correction (**methods**).
1201 **C.** Ranked TF motif enrichment of all positive regulatory peaks of the AP-1 members, relative to
1202 background peaks using the hypergeometric test (see **methods**). **D.** Schematic of lentiviral RFX3-
1203 overexpression (RFX3-OE) transduction experiment in $CD34^+$ umbilical cord blood cells (UCB)
1204 (top). Normalized frequency of granulocytic (CFU-G) and erythroid (BFU-E) colonies grown via
1205 methylcellulose-based colony-forming unit (CFU) assay compared between control and RFX3-
1206 OE $CD34^+$ UCBs (n = 3 independent experiments, bottom). **E.** Normalized frequency of RFX3-
1207 OE and control cells obtained from scRNA-seq data. **F.** Volcano plot showing genes differentially
1208 expressed (DE) between IMP and IGP-like cells from control and RFX3-OE subsets identified via
1209 linear mixed model (LMM) with/without cluster identity (left, **methods**). Highlighted are genes
1210 enriched in the TNFα signaling via NF-κB (blue) and MYC targets (purple, box representation is
1211 same as **Fig. 1E**). Pre-ranked gene set enrichment analysis of TNFα signaling via NF-κB pathway
1212 and MYC targets comparing control and RFX3-OE UCBs (right). **G.** Volcano plot showing TF
1213 motifs differentially enriched in IFNα-treated versus baseline HSCs (chromVAR). P-values from
1214 Wilcoxon rank sum test, two sided, with Benjamini-Hochberg FDR-correction (n = 6 serial
1215 samples from 3 individuals, see **table S13** for cell numbers, **methods**). **H.** Heatmap showing
1216 synergy scores between TFs as assessed by measuring the excess variability of accessibility for
1217 peaks with both TF motifs (*125*). **I.** TF motif accessibility across stem and progenitor subsets in
1218 lymphoid development between baseline and IFNα-treated cells.

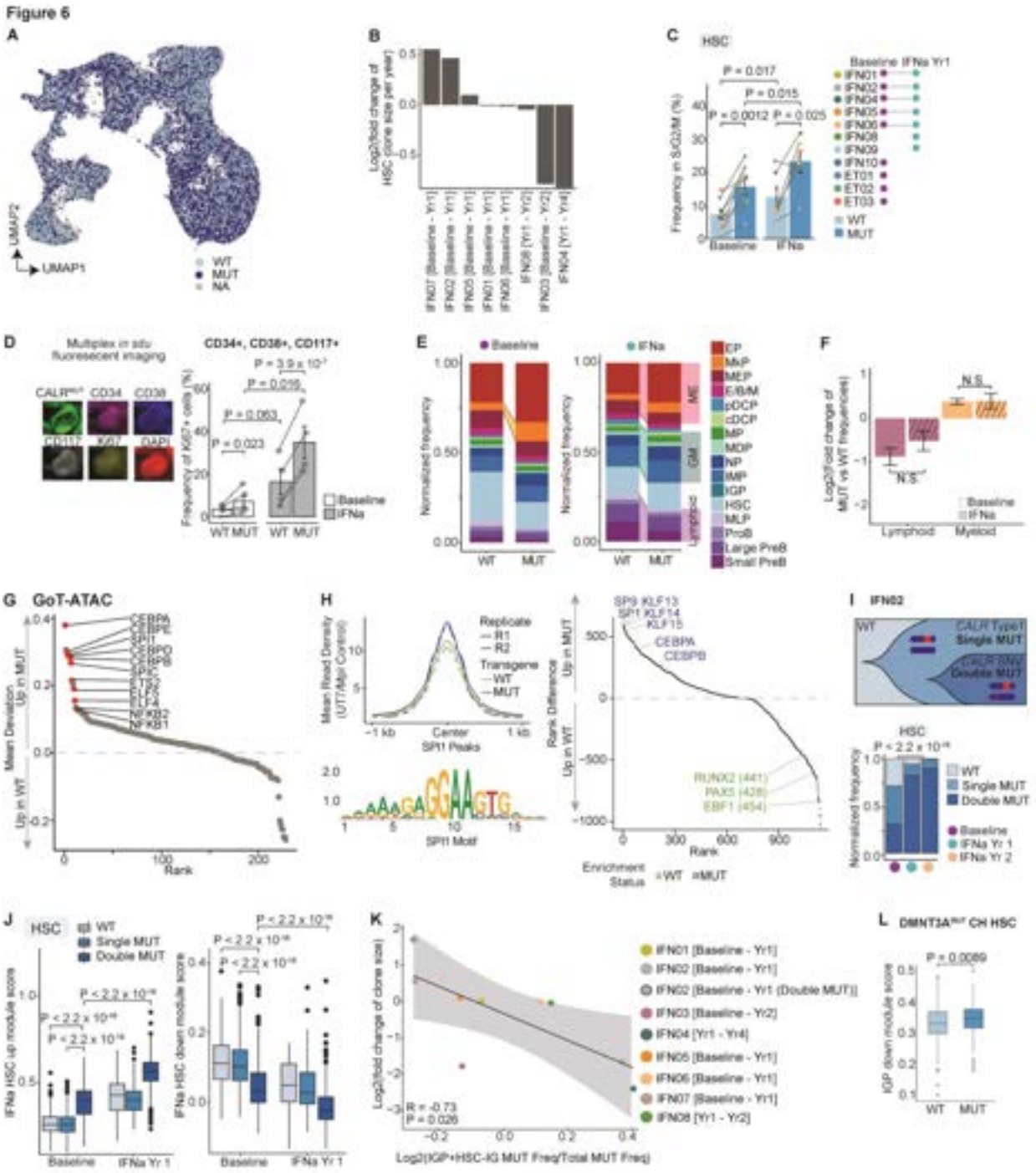

Figure 6. IFNα modulates clonal dynamics via clonal HSC differentiation into IGP differentiation. A. UMAP of CD34$^+$ cells (n = 65,452 cells) with mutation status highlighted for wildtype (WT; n = 21,354), *CALR*-mutant (MUT; n = 25,529) or unassigned (NA; n =18,569) cells. **B**. Bar plot showing HSC clone size changes at baseline and after IFNα treatment. **C.** Bar plots showing frequencies of cells in G2/M/S phase as assessed in **Fig. 3C** (n = 11 baseline and 9 IFNα-treated, year 1 samples). P-values from likelihood ratio tests of linear mixed model (LMM) with/without treatment status (for comparisons between treatment) or mutation status (for

1227 comparisons between genotypes). **D.** Multiplex *in situ* fluorescence imaging of bone marrow
1228 biopsy sections from MPN patients with (n = 4) or without (n = 5) treatment with IFNα (**methods**).
1229 Representative images of protein markers (top). Bar plots showing frequencies of proliferating
1230 myeloid cells as assessed by Ki67 expression (bottom). P-values from likelihood ratio test of LMM
1231 with/without treatment status or mutation status. **E.** Normalized cell type frequencies of WT versus
1232 MUT cells at baseline (n = 11 samples, left) and following IFNα-treatment (n = 9 samples, right).
1233 Cells down-sampled to 500 for each sample. **F.** Fold change of normalized cell frequency of MUT
1234 versus WT cells in the progenitor groups at baseline and following IFNα treatment. **G.**
1235 Transcription factor (TF) motif enrichment in MUT versus WT stem and early progenitor cells
1236 (HSCs, IMPs, MDPs/MLPs and MEPs) at baseline. TFs differentially regulated by IFNα were
1237 tested (**table S20**). Red = $P < 0.05$. P-values combined using Fisher's combined test (**methods**).
1238 **H.** Density plot showing PU.1 peak count in WT and MUT cells from the control group of
1239 megakaryoblastic cell line expressing TPO receptor (UT7-MPL) with wildtype or mutant *CALR*
1240 transgenes (n = 2 independent experiments, left). Differential TF motif enrichment between PU.1
1241 binding sites in WT IFNα-treated and MUT IFNα-treated UT7-MPL cells (right, **methods**).
1242 Analysis conducted with HOMER. TFs enriched in differentially accessible PU.1 peaks for MUT
1243 and WT cells are highlighted in blue and green respectively. **I.** Schematic of clonal structure of
1244 HSCs from patient IFN02 (top). Bar plot of normalized mutant cell frequencies across treatment
1245 time-points (bottom). P-value from pairwise Fisher's exact test. **J.** Box plot showing HSC-specific
1246 IFNα-induced signature score in HSC clones at baseline and after one year of treatment. Scores
1247 calculated using upregulated or downregulated genes (left and right panels, respectively,
1248 **methods**). P-values from Wilcoxon rank sum test, two-sided. **K.** Clone size change with IFNα
1249 treatment versus difference in normalized frequency of MUT HSC-IGs and IGPs out of all MUT
1250 cells. P-value from F-test, Pearson correlation. Shading denotes 95% confidence interval. **L.** Box
1251 plots showing IGP-specific downregulated signature score in wildtype and *DMNT3A*-mutant
1252 HSCs from individuals with clonal hematopoiesis (CH) (n = 4 samples, no. cells = 1316 wildtype,
1253 529 mutated cells) (*42*). P-values from likelihood ratio test of linear mixed model with/without
1254 mutation status.

1255
1256

1257 **Materials and Methods**

1258 **Patient samples**

1259 The study was approved by the local ethics committee and by the Institutional Review Board (IRB)
1260 of Weill Cornell Medicine. The study was conducted in accordance with the Declaration of
1261 Helsinki protocol, and all patients provided informed consent. Cryopreserved bone marrow
1262 mononuclear cells were obtained from patients with *CALR*-mutated essential thrombocythemia
1263 (ET) treated with weekly pegylated IFN-alfa2a during clinical trials MPN-RC-111
1264 (NCT01259817) (*19*) and MPN-RC-112 (NCT01258856) (*20*). Samples used for $CD34^+$ cell
1265 analysis include 8 baseline and 13 treated samples (3 of which were collected post-IFNα
1266 discontinuation) collected from 10 individuals for GoT-IM. Three baseline ET samples (ET01-
1267 ET03) from our previous work (*16*) were included as additional baseline controls with a similar
1268 distribution of age, gender, and disease status for treated samples that did not have a paired baseline
1269 control. For GoT-ATAC, n = 4 baseline and n = 3 treated samples were included from the clinical
1270 trials. For GoT-IM of $CD34^-$ mature cell analysis, 5 baseline and 10 treated samples (2 of which
1271 were collected following IFNα discontinuation) were collected from 7 individuals. Two
1272 hydroxyurea-treated peripheral blood samples from *CALR*-mutated ET patients from MPN-RC-
1273 112 were included for scRNA-seq of $CD34^+$ cells. **Table S1** includes detailed clinical and sample
1274 information collected according to clinical trial protocols.

1275

1276 **Cell preparation**

1277 Cryopreserved bone marrow mononuclear cells were thawed and stained using standard
1278 procedures with the surface antibody CD34-PE (clone AC136, dilution 1:50, Miltenyi Biotec) and
1279 DAPI (Sigma-Aldrich), according to manufacturer's protocol. To eliminate experimental batch
1280 effects, cells were labelled simultaneously with hashing antibodies with time-point-identifying
1281 barcodes as described (*21*) using Hashtag Antibodies 1-6 (TotalSeq-A, clone LNH-94, BioLegend)
1282 for GoT-IM and Anti-Nuclear Pore Hashing Antibodies 9 and 10 (Clone LNH-94, BioLegend) for
1283 GoT-ATAC. To link cell identities to expression of cell surface proteins, cells were also incubated
1284 with CITE-seq antibodies (*22*) according to manufacturer protocol (TotalSeq-A, BioLegend, see
1285 **table S31** for information on antibodies). For IFN01-IFN10 and IFN13, cells were subsequently
1286 sorted for $DAPI^-$ and $CD34^+$ cells to isolate $CD34^+$ populations. For IFN01, IFN02, and IFN09,
1287 we sorted for $DAPI^-$ and $CD34^-$ cells to isolate mature bone marrow cells. For IFN05, IFN08,
1288 IFN11, and IFN12, CD34 expression by side scatter was used to enriched for granulocytes. $CD34^-$,
1289 high side-scatter (SSC) was used to sort for granulocytes, medium SSC to enrich for
1290 monocytes/DCs, and low SSC to enrich for lymphocytes. Mature cell populations were then pooled
1291 at approximately equal ratios for granulocytes, monocytes/DCs, and lymphocytes for each sample.
1292 All FACS sorting was completed using BD Influx at the Weill Cornell Medicine flow cytometry
1293 core.

1294

1295 **GoT-IM**

1296 To simultaneously capture genotyping data and whole transcriptomic data, Genotyping of
1297 Transcriptomes (GoT) was performed by adapting the 10x Genomics platform as previously
1298 described (*16*). FACS-sorted $CD34^+$ cells for each time-point from the same individual were
1299 pooled. The standard 10x Genomics Chromium 3′ (v.3.1 chemistry) was implemented according

1300 to the manufacturer's recommendations up to the cDNA amplification step (10x Genomics,
1301 Pleasanton, CA). After cDNA amplification and SPRI bead (Beckman Coulter) cleanup, 10x
1302 scRNA-seq and ADT/HTO libraries were generated as recommended. A portion of the cDNA was
1303 used for somatic genotyping as previously described (*16*). Briefly, to capture the somatic
1304 genotypes of cells, cDNA was amplified with a locus-specific amplification (10-16 PCR cycles),
1305 using the generic forward SI-PCR primer and a locus-specific reverse primer for the *CALR*
1306 mutations (see **table S31** for primer sequences). The amplified locus-specific cDNAs are then
1307 cleaned using SPRI purification to remove unincorporated primers. Finally, the targeted amplicon
1308 libraries are generated through a PCR performed with a P5 generic forward PCR primer together
1309 with an RPI-x primer (**table S31**). The targeted amplicon libraries were spiked into the remainder
1310 of the gene expression and immunophenotyping libraries to be sequenced together on a NovaSeq
1311 (Illumina, San Diego, CA). The cycle settings were as follows: 28 cycles for Read 1, 90 cycles for
1312 Read 2, 10 cycles for i7 sample index and 10 cycles for i5 sample index.

1313

1314 **GoT-IM scRNA-seq data processing, alignment, cell-type classification and clustering**

1315 For single-cell GoT-IM data from IFN01-IFN10 patient $CD34^+$ samples and from IFN01, IFN02,
1316 IFN05, IFN08, IFN09, IFN11 and IFN12 patient $CD34^-$ samples, the pooled scRNA-seq, CITE-
1317 seq and hashing libraries were processed with Cell Ranger (v6.1.1 and v6.1.2) using cellranger-
1318 multi pipeline (v1). The reads were aligned to the human genome GRCh38 with default
1319 parameters. The Seurat package (*126*) (v4.1.0) was used to perform unbiased clustering of the
1320 $CD34^+$ sorted cells from each patient. In brief, for individual datasets, cells with UMI > or < 3
1321 standard deviations from the mean UMI and mitochondrial gene percentage >10% were filtered
1322 (**fig. S1A, S4A**). The HTO data was normalized with centered log-ratio (CLR) transformation and
1323 used to assign the time-points for each experiment (*21*). The cells from each time-point were
1324 analytically separated into individual datasets based on the HTO counts (**fig. S1B**). These
1325 individual datasets (in case of $CD34^+$ samples, together with the baseline ET samples from our
1326 previous work (*16*)), were integrated and underwent batch-correction within Seurat, which
1327 implements reciprocal principal component analysis (RPCA) and the principles of mutual nearest
1328 neighbor (*127*). Recommended settings were used for the integration (30 principal components for
1329 the anchor determining procedure in IntegrateLayers function). Principal component analysis was
1330 performed using variable genes using recommended settings (i.e., top 2000 variable genes using
1331 variance stabilizing transformation) (*127*). The first 30 statistically significant principal
1332 components were used as inputs to the UMAP algorithm for dimensional reduction and
1333 visualization (*128*). Clusters were manually assigned based on differentially expressed genes using
1334 the FindAllMarkers function using default settings (using top 2000 variable genes, in a minimum
1335 of 10% of cells in either of the two comparison sets as input, and log-transformed fold change of
1336 0.25 as the threshold, using Wilcoxon rank sum test). The clusters were annotated according to
1337 canonical lineage markers identified previously in single-cell RNA-seq data of normal
1338 hematopoietic progenitor cells (*24*) into 16 main progenitor subsets based on expression of levels
1339 of these canonical markers (Fig. 1C, **fig. S2A-C, S4C**). For dimensional reduction and
1340 visualization of individual experiments (e.g., **fig. S1H**), top 3000 variable genes were included for
1341 principal component analysis, and the first 30 statistically significant principal components were
1342 used as inputs to the UMAP algorithm. The CITE-seq data after normalization using the CLR
1343 transformation was used to distinguish cell types (**Fig. 2B, fig. S2B**) and identify HSCs (**fig. S2D**).

1344 Same integration and downstream clustering methods were used to analyze the two hydroxyurea
1345 (HU) samples.

1346

1347 **IronThrone-GoT for processing targeted amplicon sequences and mutation calling**

1348 Analysis of the GoT library was carried out as described previously (*16*) using IronThrone pipeline
1349 V2.1 (*42*). Amplicon reads (Read 2) were screened for the presence of the primer sequence and
1350 the shared sequence (i.e., the expected sequence between the primer sequence and the mutation
1351 locus). Reads (Read 1) from GoT-IM experiments were also assessed for matching to the cell
1352 barcode list of the 10x dataset. A mismatch of 20% was allowed for all sequence matching steps.
1353 Only UMIs with at least 2 or more supporting reads were retained for final genotyping
1354 assignments, after the UMI collapse algorithm, as previously described (*42, 129*). Filtered cells
1355 were then genotyped as follows, as previously described: cells with at least one mutant UMI were
1356 categorized as mutant cells whereas cells with no mutant UMI and at least one wildtype UMI were
1357 identified as wildtype.

1358

1359 **Gene module scoring, differential expression and gene set enrichment analysis**

1360 For statistical analysis, when the variable in question was cell type identity (e.g., IGP vs IMP), cell
1361 type identity was entered as the fixed effect and samples as random effects in a linear mixed model.
1362 For IGP and IMP comparison, treatment status was also included as a fixed effect. When the
1363 variable in question was genotype status (e.g., *CALR* mutant versus wildtype), genotype status was
1364 entered as the fixed effect and samples as random effects in a linear mixed model. P-values were
1365 obtained from likelihood ratio tests of the full model with the effect in question against the model
1366 without the effect in question. Linear mixed effects analysis was performed using the lme4 package
1367 (v.1.2-1) (*130*).

1368 Differential gene expression testing between two groups within an individual experiment (e.g.,
1369 **Fig. 6J**) was performed using the logistic regression framework (*131*) with the FindMarkers
1370 function. The tested genes included the top 2,000 variable genes from the CCA integration, which
1371 were filtered for those expressed in at least 10% of either group. In aggregated differential gene
1372 expression analysis (e.g., treated versus baseline as in **Fig. 3B**), the two groups were compared via
1373 the linear mixed model framework, as previously described (*42*). Among $CD34^+$ cells with GoT-
1374 IM data, IFN01-IFN10 samples at baseline and active treatment were included for the differential
1375 expression analysis. For each gene, the variable in question (i.e., treatment or mutation status) was
1376 entered as the fixed effect and samples as random effects. P-values were obtained from likelihood
1377 ratio tests of the full model with the effect in question against the model without the effect in
1378 question. Individual genes with abs(avg_log2FC)> 0.1 and adjusted p-value <0.05 were significant
1379 for further analysis such as module scoring for HSC-specific IFNα-induced upregulated or
1380 downregulated genes.

1381 Pathway enrichment analysis was performed via a pre-ranked gene set enrichment approach
1382 (ranking based on the sign of the fold change * -log10(adjusted P-value)) using the msigdbr
1383 (v7.2.1) (*132*) and fgsea (v1.12.0) (*133*) R packages, using the canonical Hallmark pathway genes
1384 from MsigDB (*134*).

1385 For examining gene module expression (e.g., HSC-specific IFNα-upregulated or downregulated
1386 gene signature), the function AddModuleScore within the Seurat package (*126*) was used to

1387 calculate the relative expression of the genes (that are significantly upregulated or downregulated,
1388 as described above) for each cell. To calculate the module expression of cell-cycle related genes,
1389 G2M phase and S phase marker genes were used as available in Seurat with CellCycleScoring
1390 function. Briefly, expression of a control gene module was calculated and subtracted from the
1391 average gene module expression of interest, as previously described (*44*). All analyzed genes were
1392 classified based on average expression into 24 bins, and for each gene in the module, 100 control
1393 genes are randomly selected from the same expression bin as the gene of interest (*44*). For the
1394 overall IGP module score (**Fig. 2C**), the cells were first scored for the upregulated and
1395 downregulated genes (**Fig. 1E**); the downregulated gene score was subtracted from the upregulated
1396 gene score to obtain the overall IGP score.

1397

1398 **RNA velocity analysis using scVelo and partition-based graph abstraction**

1399 RNA velocity was assessed from the spliced and unspliced transcript variants using scVelo
1400 (v0.2.5) (*34*). Counts from loom files generated with Velocyto (v0.17.17) (*35*) for each GoT-IM
1401 sample (IFN01-IFN09) were normalized and filtered (UMI counts > 100 and UMI count < 20000).
1402 The annotated data matrices were combined by using anndata.concat() command and cell-specific
1403 annotations such as cell-type, time-point, UMAP and PCA embeddings were imported from the
1404 GoT-IM integrated object. Connectivities between the cell clusters were quantified
1405 using scvelo.tl.paga() within the partition-based graph abstraction (PAGA) framework (*36*).

1406

1407 **GoT-ATAC**

1408 Cryopreserved bone marrow mononuclear cells were thawed and stained using standard
1409 procedures with the surface antibody CD34-PE (clone AC136, dilution 1:50, MACS) and DAPI
1410 (Sigma-Aldrich), according to manufacturer's protocol. Cells were subsequently sorted for $DAPI^{-}$,
1411 $CD34^{+}$ cells using BD Influx at the Weill Cornell Medicine flow cytometry core. Nuclei were
1412 isolated from $DAPI^{-}$, $CD34^{+}$ cells according to 10x Genomics Demonstrated Low Cell Input
1413 Nuclei Isolation protocol. Lysis buffer was prepared following manufacturer's recommendations
1414 and then split into aliquots for each serial sample. Either TotalSeq-A Anti-Nuclei Pore Complex
1415 Proteins Hashtag 9 or 10 Antibody (1µL at 1:5 dilution; BioLegend) was added to each aliquot of
1416 lysis buffer. Low-input nuclei isolation was otherwise performed following manufacturer's
1417 recommendations. Subsequently, nuclei from each time-point were counted and pooled together
1418 at approximately equal proportions. For IFN07, additional nuclei from the IFNα-treated sample
1419 were available to be run on a separate lane. Single-nucleus gene expression (GEX) and chromatin
1420 accessibility libraries were constructed from the pooled nuclei according to the Chromium Next
1421 GEM Single Cell Multiome User Guide (10x Genomics).

1422 Genotyping libraries targeting the *CALR* mutant transcripts were constructed from the remaining
1423 amplified cDNA, similar to the original GoT method. For each PCR, 12.5µL Kapa HiFI HotStart
1424 Ready Mix was mixed with 0.75µL of 10uM forward primer, 0.75µL of 10uM reverse primer, 3µL
1425 cDNA and nuclease-free water for a total reaction volume of 25µL. In the first PCR, 3µL cDNA
1426 was re-amplified with Partial TSO and Partial Read 1 primers (**table S31**), using the following
1427 PCR condition: 98°C for 3min; 3 cycles of 98°C for 15sec, 67°C for 20sec and 72°C for 1min;
1428 72°C for 1min. The re-amplified sample was purified and concentrated via 0.7X SPRI cleanup,
1429 eluting it into 10µL Buffer EB. To pre-enrich the *CALR* mutation locus, a gene-specific PCR was

1430 performed with 3µL of cleaned re-amplified cDNA and Partial Read 1 and gene-specific primers
1431 (**table S31**). The following PCR condition was used: 98°C for 3min; 11 cycles of 98°C for 20sec,
1432 60°C for 20sec, and 72°C for 2min; 72°C for 2min. After 0.7X SPRI cleanup, cDNA was eluted
1433 into 10µL Buffer EB. *CALR* locus-specific amplification was then performed with 3µL of cleaned
1434 gene-specific amplified cDNA and SI-PCR and loci-specific Primers, using the PCR condition:
1435 98°C for 3min; 11 cycles of 98°C for 20sec, 60°C for 20sec, and 72°C for 2min; 72°C for 2min.
1436 A 0.7X SPRI cleanup was performed, and cDNA was eluted into 11µL Buffer EB. Finally, to
1437 construct the targeted amplicon library, loci-amplified cDNA was mixed with P5 Generic and
1438 RPIx indexing primers (**table S31**) and amplified with the PCR condition: 98°C for 3min; 5 cycles
1439 of 98°C for 15sec, 60°C for 20sec, and 72°C for 1min; 72°C for 1min. The constructed library was
1440 cleaned via 0.8X SPRI cleanup and eluted into 12µL Buffer EB.

1441 At the cDNA amplification stage of the Chromium Next GEM Single Cell Multiome protocol,
1442 supernatant from the 0.6X size selection was retained and was used to generate the hashing
1443 libraries as per HTO protocol (*21*) with the following modification. For the hashing library
1444 construction step, the PCR reaction was prepared with 0.65µL of 10uM SI-PCR primer, 0.65µL of
1445 10uM TruSeq DNA D7xx_s primer (**table S31**), 11.25µL cleaned supernatant and 12.5 µL KAPA
1446 HiFi HotStart Ready Mix (Roche, Basel, Switzerland). Hashing, gene expression and genotyping
1447 libraries were pooled and sequenced together on a NovaSeq (Illumina) with cycle settings: 28
1448 cycles for Read 1, 90 cycles for Read 2, 10 cycles for i7 sample index and 10 cycles for i5 sample
1449 index. The ATAC library was sequenced separately on a NovaSeq, with cycle settings: 50 cycles
1450 for Read 1 and Read 2, 8 cycles for i7 sample index and 24 cycles for i5 sample index.

1451

1452 **Data preprocessing, alignment and cell type identification for GoT-ATAC**

1453 For single-nuclei GoT-ATAC data from IFN01, IFN03, IFN07 and IFN13 patient $CD34^+$
1454 samples, 10x data were processed using Cell Ranger (v6.1.1 and v6.1.2). Multi-omic nuclear data
1455 for snATAC-seq and snRNA-seq were processed together with Cell Ranger Arc (v2.0.0). snRNA-
1456 seq data was also combined with cell hashing data (HTO) and run using the Cell Ranger Multi
1457 pipeline (v1). The reads were aligned to the human reference genome GRCh38. The downstream
1458 analysis of the processed data was performed using Seurat (v4.1.0) (*126*) and Signac (v1.5.0) (*135*)
1459 packages. For the ATAC analysis, we called peaks on individual samples using MACS2 peak
1460 caller (*136*). Gene annotations from EnsDb.Hsapiens.v86 and motifs annotations from Cis-BP
1461 (*137*) for TF binding motifs were utilized. Cells with blacklist ratio >0.02, TSS enrichment <2 and
1462 nucleosome signal >4 were filtered out. For the RNA data, cells with UMI > or < 3 standard
1463 deviations from the mean UMI or mitochondrial gene percentage > 25%, were filtered (**fig. S7A-**
1464 **D**). The nuclei hashing data processing was performed as for the GoT-IM data (**fig. S7E**). As
1465 nuclear hashing is known to be noisier than cell hashing (*135*), the nuclear hashing data was used
1466 in combination with cell clustering data, as the cells cluster based on treatment status. After the
1467 cells were segregated analytically based on time-point, the datasets were integrated as described
1468 for the GoT-IM data. snRNA-seq data were integrated where they underwent batch correction with
1469 canonical correlation analysis (CCA) within Seurat and the principles of nearest neighbor (*127*).
1470 Recommended settings were used for the integration (30 canonical correlation vectors for
1471 canonical correlation analysis in the FindIntegrationAnchors function and 30 principal
1472 components for the anchor weighting procedure in IntegrateData function). Principal component
1473 analysis and cell type assignments were performed as described in GoT-IM. Integration via the
1474 ATAC-seq data was performed by normalizing the merged counts using first term frequency

1475 inverse document frequency (TFIDF) normalization with RunTFDIF followed by linear
1476 dimensional reduction using latent semantic indexing (LSI). The first 2:30 dimensions were
1477 retained, and batch-correction was performed with runHarmony (Harmony, v0.1.0) which
1478 iteratively learns cell-specific linear correction function to account for batch effect. Pseudotime
1479 analysis was performed by constructing cell lineage trajectory with Monocle 3 (*138-140*). We used
1480 as.cell_data_set function from SeuratWrappers package to convert Seurat object to CellDataSet
1481 object used by Monocle 3. IronThrone-GoT protocol was used to determine mutation calling
1482 within the GoT-ATAC assay, as described for GoT-IM. A requirement of at least four reads
1483 supporting a UMI was implemented for GoT-ATAC. To capture genotyping reads within the
1484 snRNA-seq data, we called *CALR* variants using the gene expression BAM derived from the
1485 standard Multiome workflow. BAMQL (*141*) and the CIGAR string of the BAM file were used to
1486 parse reads containing the expected wildtype and mutant sequences. Cells expressing at least one
1487 mutant UMI were categorized as mutant and cells with just wildtype UMI were assigned as
1488 wildtype. Genotyping assignments were then appended to calls made by IronThrone.

1489

1490 **Identification of distal regulatory elements with gene-peak cis-association**

1491 For each GoT-ATAC sample, we examined all ATAC peaks within ± 500kb of all annotated TSS
1492 to identify regulatory networks of genes using LinkPeaks function (*72*). Pearson correlation
1493 between gene expression and accessibility of the peaks located in the window was calculated after
1494 correcting for bias arising from GC content, overall accessibility and peak size. Recommended
1495 settings were implemented (200 background peaks per peak with similar GC content and
1496 accessibility, P-value < 0.05 and min.cell = 10).

1497

1498 **Motif enrichment analysis in GoT-ATAC**

1499 Per-cell TF motif activity score (chromatin accessibility) was calculated by running chromVAR
1500 (v1.18.0) (*69*). We used the curated Cis-BP motif database (*137*) which contains 1141 human TF
1501 motif position frequency matrices (PFMs). The function matchMotifs was first called to identify
1502 which peaks contain which motifs (P-value = 5×10^{-5}). A set of background peaks that are similar
1503 to a peak in GC content and average accessibility was internally picked and used for normalizing
1504 the deviation scores. Deviation Z-scores, namely bias-corrected deviation z-scores in accessibility
1505 from the expected accessibility based on the average of all the cells, were then calculated for each
1506 TF motif and each cell.

1507 To perform differential motif enrichment analysis, within a sample and on the deviation z-score
1508 computed by chromVAR, we applied the function FindMarkers in Signac (Wilcoxon Rank Sum
1509 test), where the average difference in z-score between the groups was calculated. For integrated
1510 data, we combined the P-values (Fisher's method) and calculated weighted mean deviation score
1511 across individual samples. P-values were adjusted by the Benjamini-Hochberg method.

1512 To find over-enriched motifs for a group of genomic features, the FindMotifs function was used,
1513 accounting for accessibility and GC content bias by selecting 5000 accessible background peaks
1514 with similar GC content for each feature set. To identify motifs enriched in a singular genomic
1515 range, FIMO (v5.4.1) from MEME suite (*142*) was used to scan for Cis-BP TF motifs along the
1516 nucleotide sequence from human reference genome GRCh38 with a p-value threshold of 0.0001.
1517 We de-prioritized zinc fingers (ZNFs) in the list of motifs specific to genomic regions as each

1518 individual ZNF binds to three bp motif leading to more frequent matches and higher match scores
1519 (*143*). chromVAR was used to compute the synergy between pairs of TF motifs, where synergy is
1520 defined as the excess variability of chromatin accessibility for peaks sharing both motifs compared
1521 to a random subsample of the same size of peaks with one motif. High synergy usually indicated
1522 a cooperative binding relationship between pairs of TFs. The function getAnnotationSynergy was
1523 called to calculate synergy scores (*69*).

1524

1525 **Retrospective flow cytometry data analysis**

1526 Retrospective flow cytometry data analysis was performed in accordance with relevant guidelines,
1527 regulations and approval by the Institutional Review Board at Weill Cornell Medicine (IRB
1528 #1007011151). Patient flow cytometry data selected corresponded to patients with
1529 myeloproliferative neoplasms and which had the same antibody panel analyzed by flow cytometry.
1530 Patients with a diagnosis of ET or polycythemia vera with no increase in myelofibrosis or blast
1531 counts were included in the study. The antibody panel chosen for evaluation was a modified
1532 version of the EuroFlow AML/MDS tube #4 (*144, 145*) that consisted of the following antibody-
1533 fluorophore pairs, in addition to forward scattering and side scattering pulse area and width
1534 measurements (FSC-A, FSC-H, SSC-A, and SSC-H): cytoplasmic TdT/FITC (clone HT-6,
1535 Agilent/Dako, cat. F7139), CD56/PE (clone C5.9, Cytognos, cat. CYT-56PE), CD34/PerCP-Cy5.5
1536 (clone 8G12, BD Biosciences, cat. 347213), CD117/PE-Cy7 (clone 104D2D1, Beckman
1537 Coulter/Immunotech, cat. IM3698), CD7/APC (clone GP40 [Leu-9], Invitrogen, cat. 17-0079-42),
1538 Fixable Viability Stain 700 (BD Biosciences, cat. 564997), CD19/APC-H7, HLA-DR/Pacific Blue
1539 (clone SJ25C1, BD Biosciences, cat. 643078), and CD45/V500 (clone 2D1, BD Biosciences, cat.
1540 347213). Data was collected using BD LSR II flow cytometers, with approximately 500,000 events
1541 collected per antibody panel per sample to generate the raw data FCS files.

1542 Custom software was developed using python, FlowKit (*146*) and umap-learn (*128*) to detect the
1543 antibody panels that were used to generate each raw data FCS file and to determine the unused
1544 flow cytometer channels that should be disregarded using the self-contained metadata for each file.
1545 Subsamples from each FCS file were combined to make an "ensemble FCS file" that could be used
1546 to create the UMAP embedding that could be applied to each of the individual files. Each
1547 subsample consisted of the same number of randomly selected flow cytometer events such that the
1548 combined total number of events was approximately 250,000 for each unique antibody panel. The
1549 various channels were normalized and processed using UMAP to calculate the normalization
1550 constants and UMAP embedding that were then applied to all FCS files of the given antibody
1551 panel. Of note, the UMAP calculations included the forward scatter height (FSC-H), side scatter
1552 height (SSC-H) and each of the defined fluorescence channels. The normalization factors and
1553 UMAP embedding were then applied to all the individual files. Modified FCS files were created
1554 that included the UMAPs as additional channels for subsequent evaluation and gating using
1555 FlowJo software (v10.8.1, FlowJo LLC, Ashland, Oregon, USA).

1556 Using FlowJo, appropriate gates based on the UMAP plot were determined using the ensemble
1557 FCS file. Additional standard gating was also performed using the original data channels (gating
1558 using the other channels is essential to determine the identities of the various cell clusters within
1559 the UMAP plots). UMAP gates were based on data after gating out doublets and non-viable cells
1560 via standard gating approaches. Once the UMAP gates were determined to adequate satisfaction
1561 (sufficient segregation of cell subpopulations and verified to encompass cells of the same or similar

type), they were then applied to all the FCS files of the given antibody panel. The FCS files were divided into untreated/only aspirin treated cohort (n = 33), an interferon-treated cohort (n = 9), a hydroxyurea-treated cohort (n = 10). The ratios and absolute numbers of cells, as well as other summary statistics were then calculated, and the values exported as CSV files. Statistics included numbers of $CD34^+$ blasts; $CD19^+$, $cTDT^+$, $CD34^+$ lymphoid progenitors; $CD19^+$ lymphocytes; CD19-negative lymphocytes/NK cells; and monocytes. Relevant distributions of cells for each cohort are plotted, and the Wilcoxon p-statistic was calculated for various compared distributions.

Multiplexed Immunofluorescence

Multiplexed immunofluorescence (mIF) was performed using the Opal system (Akoya Biosciences) by staining 4 micron-thick Bouin-fixed, paraffin-embedded whole-tissue sections from decalcified human bone marrow core biopsy specimens in a Bond RX automated tissue stainer (Leica Biosystems, Buffalo Grove, IL), as described previously (*147, 148*). Briefly, tissue sections were first deparaffinized prior to EDTA-based antigen retrieval (Leica ER2 solution, 20min). A cyclical staining protocol was then performed, with horseradish peroxidase-mediated deposition of tyramide-Opal fluorophore constructs (Akoya Biosciences) in each cycle, with intervening application of heat, citrate-based epitope retrieval solution (Leica ER1), and Bond Wash Solution (Leica) to execute stripping of primary/secondary antibody complexes between staining cycles. Finally, 4', 6-diamidino-2-phenylindole (Spectral DAPI, Akoya Biosciences) was applied per provided protocols to label nuclei. The following panel of primary antibody/fluorophore pairs was applied to all cases, in a sequential order as shown: 1) Opal 480/anti-mutant CALR (1:120, CAL2, Dianova), 2) Opal 520/anti-CD38 (1:50, 38C03 (SPC32), Invitrogen), 3) Opal 570/anti-CD117 (1:100, D3W6Y, Cell Signaling), 4) Opal 620/anti-TdT (1:8, SEN28, Invitrogen), 5) Opal 690/anti-CD34 (1:100, QBEND/10, Invitrogen), 6) Opal 780/anti-Ki67 (Ready-to-use, MM1, Leica). Slides were cover-slipped using ProLong™ Diamond Antifade Mountant (Invitrogen). Whole slide scans were subsequently obtained at 20X magnification using the Vectra Polaris Automated Quantitative Pathology Imaging System (Akoya Biosciences) to generate a collection of tiled images, which were subsequently spectrally unmixed in InForm (v2.4.8, Akoya Biosciences). Unmixed tiles were finally fused together in HALO (v3.3.2541.231, Indica Labs) to generate a multi-layered TIFF image file for each sample, which was used in downstream analyses.

Image Analysis with PathML

Vectra whole-slide images (WSIs) were digitized using digital whole-slide scanners and stored in tiff format. WSIs of bone marrow sections were captured (n = 9 samples). Each sample was stained based on 8 cell markers including DAPI, mutant-specific CALR, CD38, CD117, TdT, CD34, Ki67, and auto-fluorescence. The image contrast was enhanced using histogram equalization in Fiji. To analyze the Fiji-preprocessed WSIs, PathML, a toolkit for computational image analysis (*149*), was applied to images. Images were loaded and divided into equal-sized tiles on which we ran our preprocessing pipeline. This pipeline starts with coercing the tile shape into the standard x,y,c format followed by segmentation. Nuclear and cellular segmentation were performed using the Mesmer (*150*) deep learning segmentation model implemented in PathML with DAPI and autofluorescence used as nuclear and cell membrane markers, respectively. Subsequently, we used the 'QuantifyMIF' function from PathML to convert the segmented images into count matrix

1606 which includes the intensity of each marker in each segmented cell along with cell coordinates,
1607 size, and eccentricity. To remove the noise from the count matrix data, any cell with raw intensity
1608 less than 50 for DAPI and auto-fluorescence markers was excluded from the analysis. Next, the
1609 thresholds were obtained to find the positive and negative expression level for each cell marker.
1610 The thresholds were manually set for each marker based on examination by a board-certified
1611 hematopathologist.

1612

1613 **CUT&RUN Assay**

1614 UT7 cell lines expressing MPL (thrombopoietin receptor) and either the mutant *CALR* (type 1,
1615 L367Tfs*46) or wildtype *CALR* transgene (*93*) were seeded in 10cm plates in DMEM
1616 supplemented with 10% FBS (Thomas Scientific) and 5 ng/ml GM-CSF (Miltenyi-Biotec). Cells
1617 were treated with 0.1µg/ml Recombinant Human IFN-alpha2a (RC217-14) or PBS-1X control for
1618 24hrs. After treatment, cells were washed 1x with PBS and collected for use with the CUTANA™
1619 CUT&RUN assay (EpiCypher) according to the manufacturer's protocol. 0.5µg of anti-human
1620 rabbit monoclonal PU.1 antibody (ab76543) and IgG antibody (ab172730) were used in the assay.

1621 CUT&RUN data were down-sampled to have same number of reads across all conditions within
1622 the sample replicate to account for difference in sequencing depth. Among the down-sampled
1623 reads, low-quality reads were filtered out using Trimmomatic (*151*), resulting reads were aligned
1624 with hg38 genome with Bowtie2 (*152*), and PCR duplicates were removed with SAMtools (*153*)
1625 with a previously described workflow (*154*). Aligned reads were then used for peak calling with
1626 MACS3 (*136*) with a q-value threshold of 0.01 and reads from IgG antibody as the control. SPI1
1627 over-enrichment in the called peaks was confirmed with Simple Enrichment Analysis (SEA,
1628 v5.5.5) (*155*). Overlapping peaks between replicates of the same condition were kept for further
1629 processing. The peaks were processed with multiBamSummary function from deepTools (*156*) to
1630 obtain counts matrix per sample for downstream analysis.

1631 Differential peak enrichment analysis was run between conditions (MUT vs WT and IFNα-treated
1632 vs control) using DESEQ2 (*157*) for distal PU.1 peaks. Differential peaks in each condition were
1633 centered around SPI1 motif and motif enrichment was performed for regions +/- 250 bp from SPI1
1634 motif using HOMER (v.4.1.1) (*96*). Differential ranking between each motif two conditions was
1635 calculated (**Fig. 6H, right, fig. S12B, D**).

1636

1637 **Single-cell Differentiation Assay**

1638 One day before sorting HSCs, flat-bottom 96-well plates were coated with 60µL 0.2% gelatine
1639 (Sigma) per well for 1 hour and then removed. Low passage murine MS5 stroma cells were plated
1640 at a density of 1500 cells/well in 100µL Myelocult H5100 medium (Stem Cell Technologies), 1%
1641 Penicillin-Streptomycin (Pen/Strep, 10,000 U/mL, Gibco) and 1% glutamine (Gibco). On the day
1642 of the assay, the medium was changed to lympho-myeloid media consisting on 100µL/well
1643 Myelocult H5100 medium, 1% Pen/Strep and 1% glutamine supplemented with the following
1644 cytokines: IL-2 10ng/mL, IL-6 20ng/mL, IL-7 20ng/mL, SCF 100ng/mL, TPO 50ng/mL, G-CSF
1645 20ng/mL, FLT3L 10ng/mL and GM-CSF 20ng/mL (all from Bio-Techne). Cryopreserved bone
1646 marrow mononuclear cells (n = 2 baseline and 3 IFNα-treated samples) were thawed and $CD34^+$
1647 cells were isolated using the EasySep™ Human CD34 Positive Selection Kit II (StemCell
1648 Technologies #17856) following manufacturer's protocol. $CD34^+$ isolated cells were then stained

1649 with FITC CD45RA (1:50), APC-Cy7 CD34 (1:200), APC CD90 (1:50), Pe-Cy7 FLT3 (1:100),
1650 PerCP-Cy5.5 HLA-DR (1:100), and BV786 CD41 (1:100) (antibody details in **table S31**). $CD34^+$
1651 $CD90^+$ cells were index-sorted by FACS directly into 96-well plates with pre-plated MS5 stromal
1652 cells. Eight days after sorting, 70µL of media were removed from the top of the plate without
1653 disturbing the colonies, and 170µL of IMDM medium (Gibco) with 10% BIT 9500 (StemCell
1654 Technologies), 1% Pen/Strep, 1% glutamine, supplemented with IL-2 10ng/mL, IL-3 20ng/mL,
1655 IL-6 10ng/mL, IL-7 10ng/mL, SCF 100ng/mL, TPO 50ng/mL, G-CSF 10ng/mL, FLT3L
1656 10ng/mL, SDF1 5ng/mL and 2-ME (1.8µL per 50mL), were added. Colonies were analyzed under
1657 the microscope 16-18 days after sorting and all visible colonies were detached by pipetting from
1658 the stromal cell layer and transferred into a 96-well U-bottom plate using a plate filter (Pall
1659 AcroPrep), to prevent the carryover of MS5 cells. Cells were stained for 1 hour at 4ºC with FITC
1660 CD66b (1:100), PE CD16 (1:100), PerCP-Cy5.5 CD184 (1:100), Pe-Cy7 CD83 (1:100), APC
1661 CD14 (1:100), V500 CD45 (1:100), BV650 CD71 (1:100), and BV711 CD33 (1:100) (antibody
1662 details in **table S31**) with 50µL/well antibody mix and washed afterwards with 200µL PBS and
1663 2.5% FBS. Immunophenotype of the colonies was assessed in a BD LSRFortessa Analyzer. Flow
1664 cytometric analysis was performed using FlowJo and OMIQ. To generate differentiation plots,
1665 OMIQ was used to gate live cells and calculate UMAP dimensional reduction based on expression
1666 of CD14, CD34, CD45, CD71, CD33, CD16, and CD66b after integrating cells across every
1667 colony using recommended settings. A total of 177 colonies were included in the analysis from 5
1668 samples (after filtering for colonies with <350 live cells). GEMM colonies showed $CD71^+$, $CD14^+$,
1669 and $CD66b^+$ populations. GM colonies showed both $CD14^+$ and $CD66^+$ populations (at least 1%
1670 each). Neutrophil-only colonies showed <1% $CD14^+$ cells and at least 95% $CD66b^+$ cells. To
1671 increase the stringency of the neutrophil-only assignment, a minimum of 4000 events was required
1672 for this assignment. The remainder of the colonies were labeled as early myeloid (EM) colonies
1673 showing a large $CD33^+$ population (>40%) that lacked either CD14 or CD66b expression.

1674

1675 **Western Blot**

1676 1x10^6 K562 cells were seeded in triplicate in a 10cm plate in RPMI 10% FBS 1% Pen/Strep.
1677 Recombinant Human IFN-alpha2a (RC217-14) was diluted in PBS and added to treatment
1678 condition plates at a concentration of 2000U/ml. Corresponding control plates were treated with
1679 equal volumes of PBS. Cells were kept in media with or without IFNα for 24hrs or 48hrs, after
1680 which cells were collected and cell count and viability was recorded. Cells were then centrifuged
1681 at 300g for 5min at 4°C. Pellet was resuspended in cold PBS and centrifuged at 300g for 5min at
1682 4°C. Dry cell pellets were frozen at -80°C until ready for use. Cell pellets were lysed in RIPA
1683 Buffer (ThermoFisher #89901) with Protease Inhibitor (ThermoFisher #78420) and Phosphatase
1684 Inhibitor (ThermoFisher #78429) for 15min on a shaker at 4°C. Total protein was quantified using
1685 colorimetric BioRad DC Protein Assay (#5000113). Samples were run on a Novex Tris-Glycine
1686 Mini Protein Gel (ThermoFisher) according to manufacturer's protocol and transferred via
1687 standard wet transfer protocol. After blocking with 5% milk for 1hr at room temperature, blot was
1688 stained with anti-human mouse PU.1 monoclonal antibody (1:1000) (CST #89136) and anti-
1689 human rabbit Vinculin monoclonal antibody (1:10000) (ab129002) diluted in Intercept T20
1690 Antibody Diluent (LI-COR) overnight at 4°C. After washing with TBS-T (1X TBS, 0.1% Tween
1691 20) buffer, blot was stained with secondary antibodies including anti-mouse IRDye 800CW Goat
1692 anti-Mouse IgG Secondary Antibody (1:5000) AND IRDye 680RD Goat anti-Rabbit IgG

1693 Secondary Antibody (1:5000) for 1hr at room temperature (antibody details in **table S31**). Blot
1694 was then imaged using LI-COR machine and absorbance quantified using LI-COR software.

1695

1696 **Lentiviral Constructs for Overexpression Experiments**

1697 Lentiviral overexpression (OE) vectors and their corresponding control vectors were designed and
1698 obtained from VectorBuilder. All constructs included a lentivirus backbone (pLV) with gene-
1699 specific inserts, a fluorophore and an antibiotic resistance insert. The RFX3-OE insert consisted
1700 of human RFX3 ORF (NM_001377999.1) driven by the human phosphoglycerate kinase (hPGK)
1701 high-expression promoter, with CMV-mCherry-T2A-Puro for selection. The SPI1-OE and
1702 CEBPA-OE inserts consisted of the human SPI1 ORF (NM_001080547.2) and human CEBPA
1703 ORF (NM_001287424.2) respectively, driven by the hPGK promoter, with CMV-EGFP-T2A-
1704 Puro for selection. The control vectors contained the hPGK promoter driving an empty ORF
1705 stuffer, followed by CMV-mCherry-T2A-Puro or CMV-EGFP-T2A-Puro. The plasmid vectors
1706 were generated and amplified by VectorBuilder.

1707

1708 **Lentivirus Production**

1709 HEK-293T cells were seeded at a density of $2x10^6$ cells in DMEM, 10% FBS and 1% Pen/Strep
1710 in a 10cm plate. After 24 hours, media was changed to DMEM and 10% FBS. 9µg OE or control
1711 plasmid was added to 1mL Opti-MEM (ThermoFisher) containing 3µg pMD2.G plasmid and 8µg
1712 psPAX2 plasmid and incubated with Lipofectamine 2000 (ThermoFisher) in 1mL of Opti-MEM
1713 for 15min at room temperature. Mixture was then added dropwise to the cells and incubated at
1714 37°C for 24 hours. Media containing virus was collected over the next 48 hours. Lentivirus was
1715 then concentrated using Lenti-X Concentrator (Clontech #631231) according to manufacturer's
1716 protocol. Viral titer was determined using the qPCR Lentivirus Titer Kit (Applied Biological
1717 Materials LV900).

1718

1719 **Lentiviral RFX3 Overexpression of $CD34^+$ Cells**

1720 Frozen umbilical cord blood mononuclear cells were purchased from the NYC Blood Center. After
1721 cells were thawed rapidly at 37°C, red blood cell lysis was performed using ACK Lysis Buffer
1722 (ThermoFisher) on ice for 7min. Cells were then centrifuged at 300g for 5min at 4°C. Supernatant
1723 was discarded, and cell pellet was resuspended in cold MACS buffer (PBS-1X with 0.5% BSA).
1724 Cells were centrifuged at 300g for 5min at 4°C, and resuspended in cold MACs buffer at a
1725 concentration of 1x10^7 cells/mL. $CD34^+$ cells were then isolated with the EasySep™ Human
1726 CD34 Positive Selection Kit II (StemCell Technologies #17856) according to manufacturer's
1727 protocol. After isolation, cells were counted and plated in 96-well round-bottom plates (Falcon) in
1728 StemSpan™ SFEM II media (StemCell Technologies) with StemSpan™ $CD34^+$ Expansion
1729 Supplement (StemCell Technologies) and 1% Pen/Strep. After 24 hours in culture, cells were spun
1730 down and resuspended in minimal media consisting of StemSpan StemSpan™ SFEM II media
1731 with StemSpan™ $CD34^+$ Expansion Supplement, 1% Pen/Strep, 10µM prostaglandin E2
1732 (StemCell Technologies #72192) and 100ng/µl poloxamer 407 (Millipore Sigma P2164030). Cells
1733 were split into 2 technical replicates each for untransduced condition, mCherry-control vector
1734 transduction, and RFX3-OE vector transduction. Lentivirus or PBS control was added at an MOI
1735 of 100 directly into the well. Cells were then spinoculated at 300g, 32°C for 1 hour. After the spin,

1736 cells were incubated in same lentivirus-containing media for 24 hours at 37°C before resuspension
1737 in fresh media consisting of StemSpan™ SFEM II media with StemSpan™ $CD34^+$ Expansion
1738 Supplement and 1% Pen/Strep. After 48 hours of incubation, cells were stained with CD34-APC
1739 antibody (1:50) (**table S31**). Cells were then FACS isolated for the $CD34^+$ population in the
1740 untransduced condition and the $CD34^+$ $mCherry^+$ populations in the RFX3-OE and mCherry-
1741 control conditions. Three independent transduction experiments were completed with new units of
1742 umbilical cord blood cells.

1743 Untransduced, mCherry-Control, and RFX3-OE $CD34^+$ cells were stained with Cell Hashing
1744 antibodies (HTO TotalSeq-A, BioLegend) for 30 min at 4°C. Cells were then washed with FACs
1745 Buffer three times, pooled, and counted for loading. scRNA-sequencing was then performed using
1746 the 10x 3' v3.1 platform according to manufacturer's protocol. HTO demultiplexing and
1747 downstream analyses such as differential gene expression and gene set enrichment were performed
1748 as in GoT-IM for $CD34^+$ bone marrow samples. scRNA-seq experiment was completed on one
1749 replicate of three independent transduction experiments.

1750 The FACS-sorted cells were also used for colony-forming unit (CFU) assays. MethoCult total
1751 media were prepared using MethoCult™ H4034 Optimum (StemCell Technologies # 04044)
1752 supplemented with 10ng/ml human FLT3L and IL-6 (Miltenyi-Biotec) and 1% Pen/Strep. 250
1753 cells per group (Untransduced, mCherry-Control, and RFX3-OE) were added to 3mL MethoCult
1754 total and vortexed thoroughly. Tubes were then left at room temperature until bubbles rose to the
1755 surface. 1.25mL of MethoCult with cell suspension was transferred per well of a 6-well plate (2
1756 replicates per group) via blunt-edge 16g needle. Plate was incubated at 37°C for 14 days after
1757 which colonies were counted and identified by morphology. CFU assay was completed on all three
1758 of the independent transduction experiments.

1759

1760 **Lentiviral Transduction of K562 Cells**

1761 K562 cells were seeded at density of $3x10^5$ cells/mL in 24-well tissue-culture treated plates
1762 (Falcon) in 500µL of K562 media (RPMI with 10% FBS and 1% Pen/Strep) in triplicate for each
1763 of the following conditions: untransduced, mCherry-Control, RFX3-OE, EGFP-control, SPI1-OE,
1764 and CEBPA-OE. Concentrated lentivirus (or PBS-1X control for untransduced condition) was
1765 added directly to each well at MOI of 20, shaken gently and incubated at 37°C for 24 hours. After
1766 24 hours in lentivirus-containing media, plates were spun at 300g for 5min at room temperature,
1767 and supernatant media was replaced with fresh K562 media. Cells were then incubated at 37°C for
1768 72 hours to allow for vector expression. Post-72 hours, cells were pooled per condition and washed
1769 with FACS buffer (PBS-1X with 2% FBS). mCherry+ or EGFP+ cells per condition were then
1770 FACS-isolated and plated in K562 media in tissue-culture treated T25 flasks and allowed to
1771 recover for 48 hours before use in subsequent experiments. Two independent transduction
1772 experiment replicates of mCherry-Control, RFX3-OE and SPI1-OE and three independent
1773 replicates of EGFP-control and CEBPA-OE were performed.

1774

1775 ***In vitro* IFNα Treatments of SPI1-OE and CEBPA-OE Cells**

1776 $5x10^6$ untransduced, EGFP-control and SPI-OE K562 cells were seeded in 24-well TC-treated
1777 plates in 1mL of K562 media (RPMI with 10% FBS and 1% Pen/Strep). Recombinant Human
1778 IFN-alpha2a (RC217-14) was diluted in PBS-1X and added to treatment condition plates at a

1779 concentration of 2000U/mL. Equal volume of PBS-1X was added to untreated controls. After
1780 gentle shaking, cells were incubated at 37°C for 24 hours. Post-incubation, cell suspension was
1781 collected and spun at 350g for 5min at 4°C. Supernatant was aspirated and cell pellet was washed
1782 with 1mL cold PBS. Cells were spun again at 350g for 5min at 4°C. Supernatant was aspirated and
1783 dry cell pellets were frozen at -80°C until RNA was extracted.

1784

1785 **RNA extraction and RT-QPCR**

1786 Total RNA was prepared using the RNeasy Plus Micro or RNeasy Micro kit (Qiagen, #74034/
1787 74004) according to the manufacturer's instruction. RT-QPCR assays were performed using a
1788 QuantStudio™ 5 Real-Time PCR System (Applied Biosystems). One-step qRT-PCR assays were
1789 performed using the Power SYBR™ Green RNA-to-CT™ 1-Step Kit (Thermo Fisher Scientific,
1790 #4389986) according to manufacturer's instructions. The thermal cycling conditions comprised a
1791 reverse transcription step at 48°C for 30min, an initial denaturation (enzyme activation) step at
1792 95°C for 10min and 40 cycles at 95°C for 15s and 60°C for 1min. Transcripts of the TBP gene
1793 encoding the TATA box-binding protein (a component of the DNA-binding protein complex
1794 TFIID) were quantified as an endogenous RNA control. Quantitative values were obtained from
1795 the cycle number (Ct value), according to the manufacturer's manuals (Applied Biosystems) and
1796 $2^{-\Delta CT}$ values were calculated relative to TBP. Sequences of primers used for QPCR are listed in
1797 **table S31**.

1798

1799 **Statistics and reproducibility**

1800 Linear mixed modeling (LMM) was implemented using the lme4 R package (v.1.2-1). In all cases,
1801 LMMs were generated with/without cell mutational status, treatment status or cell types, as
1802 specified in the figure legends. This allowed inclusion of random effects to account for biological
1803 variation. We included patient sample as random effects in our statistical comparisons. P-values
1804 were calculated by analysis of variance with likelihood ratio test using the Stats R package (v.3.5.1)
1805 between two models (with or without the fixed variable of interest). P-value adjustments were
1806 done with Benjamini-Hochberg FDR-correction unless specified otherwise.

1807 For all box plots presented, the box represents the interquartile range; upper and lower whiskers
1808 represent the largest and smallest values within 1.5 times the interquartile range above the 75th or
1809 below the 25th percentile, respectively; the central line represents the median. Dots represent
1810 outlier values or data value distributions. For all violin plots, the violin represents the kernel
1811 probability density of the data and dots represent the observed values.
1812

1813 **Supplementary Figures**

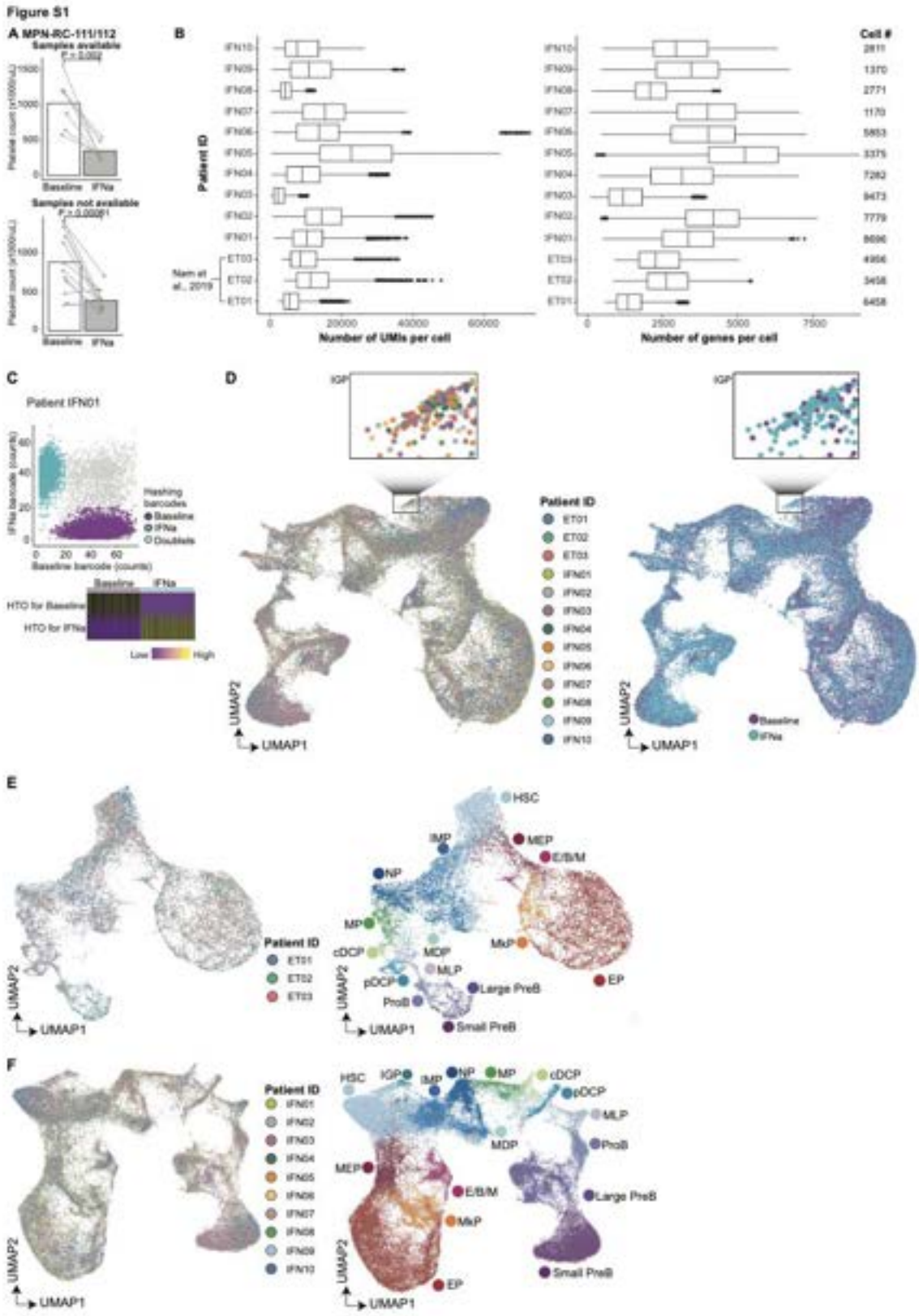

Fig. S1 (related to Fig. 1): Genotyping of Transcriptomes integrated with

1816 **immunophenotyping (GoT-IM) profiles thousands of CD34$^+$ cells at baseline and following**
1817 **treatment with IFNα. A.** Change in platelet frequency at baseline and one year upon IFNα
1818 treatment for samples (IFN01-IFN13) included in the study (top) and samples that were not
1819 available (bottom) from MPN-RC-111/112 trial. Patient samples with both baseline and year 1
1820 were included. P-values from likelihood ratio test of LMM with/without treatment status
1821 (methods). **B.** Box plots showing number of UMIs (left panel), and genes (right panel) detected
1822 per cell in sorted CD34$^+$ hematopoietic progenitors from each patient after filtering based on
1823 quality control (QC) metrics (**methods**). **C.** Top: Time-point assignment (data demultiplexing)
1824 using time-point specifying barcodes. Cells in which both barcodes are detected are considered as
1825 doublets and excluded. Representative patient sample IFN01 (n = 8,696 cells) shown. Bottom:
1826 Heatmap showing HTO expression level for baseline and IFNα-treated cells from IFN01. **D.**
1827 Uniform Manifold Approximation and Projection (UMAP) of sorted CD34$^+$ progenitors (n =
1828 65,452 cells, samples from this study and Nam et al., 2019) highlighted by patient ID (n = 13
1829 individuals, left) and treatment status (right) after integration with zoomed in view of the region
1830 with IGP cluster. **E.** Integrated UMAP of sorted CD34$^+$ progenitors from Nam et al., 2019 (n =
1831 14,872 cells) highlighted by patient ID (n = 3 individuals, left) and cell type clusters (right). **F.**
1832 Integrated UMAP of sorted CD34$^+$ progenitors of ET patients from the MPN-RC-111/112 trials
1833 (n = 50,580 cells) highlighted by patient ID (n = 10 individuals, left) and cell type clusters (right).

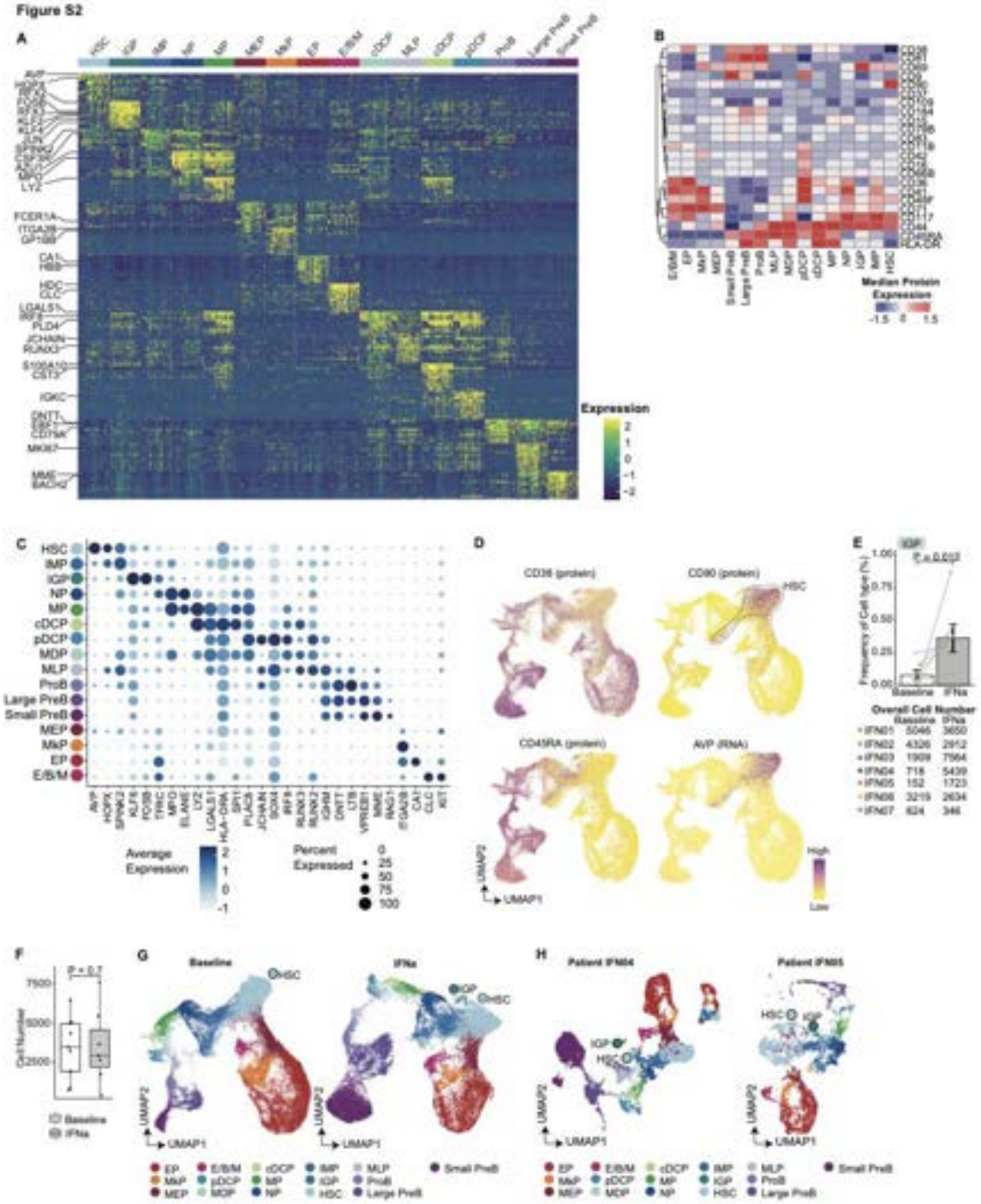

Fig. S2 (related to Fig. 1): GoT-IM of baseline and IFNα-treated samples identifies HSPC populations. A. Heatmap of top 15 differentially expressed genes for each progenitor cell type. Cells of each progenitor type were down-sampled to the same number (n = 100 cells per cluster) for visualization. **B.** Heatmap showing median scaled expression of canonical HSPC protein markers from a representative patient IFN03. **C.** Dot plot showing expression levels of cell type specific gene markers in each progenitor subset. **D.** UMAP of sorted CD34^{+} HSPCs (n = 65,452

1841 cells) highlighting CD38, CD90 and CD45RA protein expression and *AVP* RNA expression. **E.**
1842 Bar plot showing normalized IGP frequency from paired samples (n = 7 individuals) at baseline
1843 and IFNα treatment. P-value from likelihood ratio test of LMM with/without treatment status
1844 (**methods**). **F.** Box plot showing the cell frequency at baseline and upon IFNα treatment per sample
1845 (right). For IFN02, IFN04 and IFN05, the time-point powered with greater number of cells was
1846 selected. P-value from likelihood ratio test of LMM with/without treatment status (**methods**). **G.**
1847 UMAP of sorted $CD34^+$ HSPCs overlaid with cell type assignment after separate integration for
1848 baseline (left, n = 33,877 cells) and IFNα-treated (right, n = 31,575 cells) samples. **H.** UMAP of
1849 $CD34^+$ HSPCs overlaid with cell type assignment from representative samples IFN04 (n = 7,282
1850 cells, left) and IFN05 (n = 3, 375 cells, right).
1851
1852

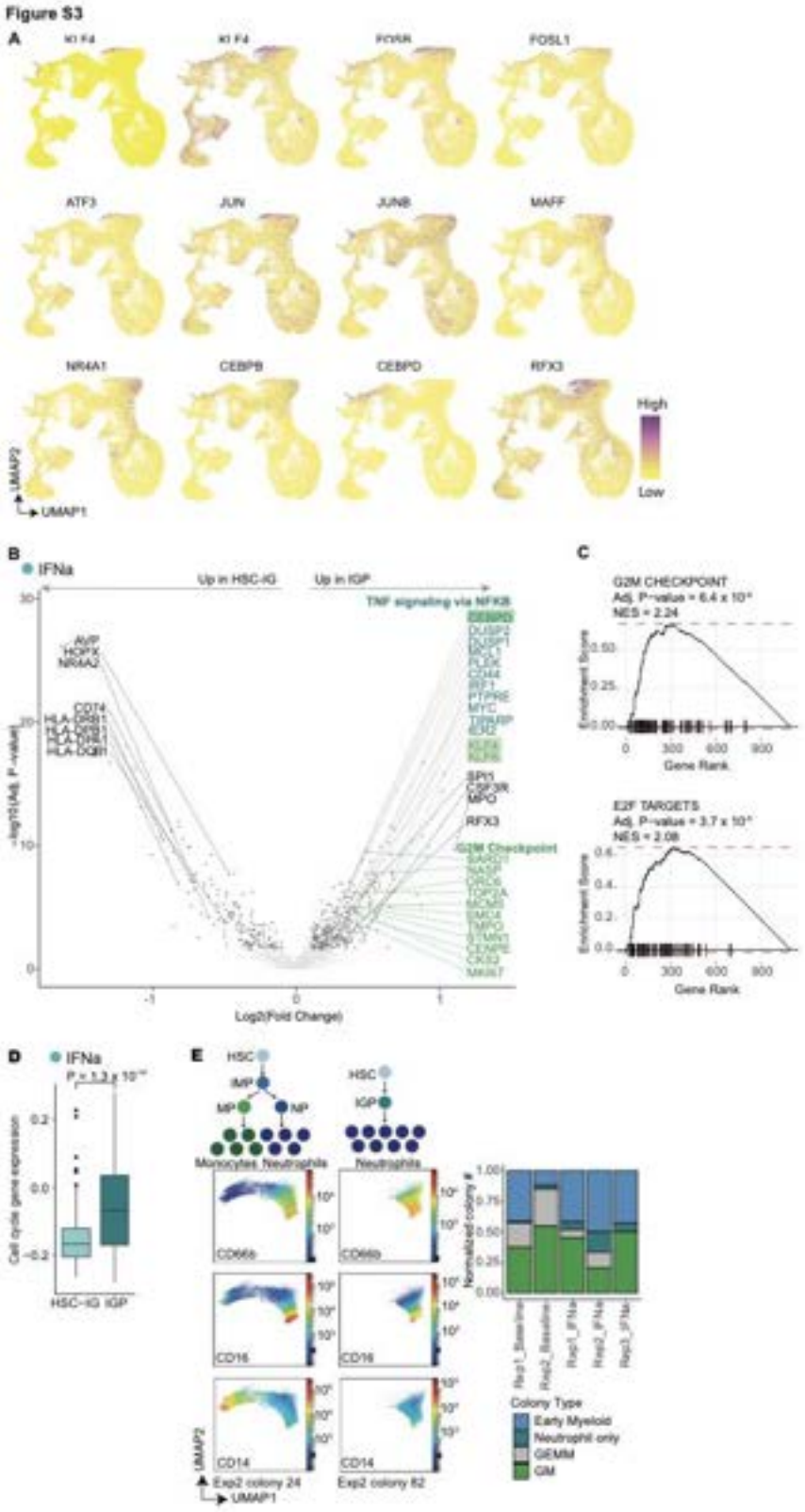

1853 **Fig. S3 (related to Fig. 1): IFNα induces a novel inflammatory granulocytic progenitor state.**

1854 **A.** UMAP showing gene expression levels of differentially upregulated TFs in IGPs compared to
1855 IMPs**. B.** Left: Volcano plot of differentially expressed genes between IFNα-treated IGPs and
1856 HSC-IGs. P-values from likelihood ratio test of linear mixed modeling with/without cluster
1857 identity as a fixed effect variable (**methods**). Genes in blue represent genes enriched in the TNFα
1858 signaling via NF-κB and those in green enriched in the G2M Checkpoint pathway (box
1859 representation is same as **Fig. 1E). C.** Pre-ranked gene set enrichment analysis using the MSigDB
1860 Hallmark collection of G2M Checkpoint and E2F Targets gene set. **D.** Cell cycle gene expression
1861 in IFNα-treated HSC-IGs vs IFNα-treated IGPs. P-value from likelihood ratio test of LMM
1862 with/without cluster identity. **E.** Schematic showing proposed model of HSC vs HSC-IG
1863 differentiation (top-left). UMAPs generated from flow-cytometric data showing representative
1864 colonies from single-cell differentiation assay from baseline and IFNα-treated BM HSCs
1865 **(methods)** depicting differentiation trajectories (bottom-left). Normalized frequency of colonies
1866 including early myeloid (EM), granulocytic (G), mixed granulocytic-monocytic (GM), mixed
1867 granulocytic, monocytic, early myeloid (GEMM) across single-cell differentiation assays from
1868 sorted baseline (n=2) and IFNα-treated (n=3) samples **(methods)** (right).
1869

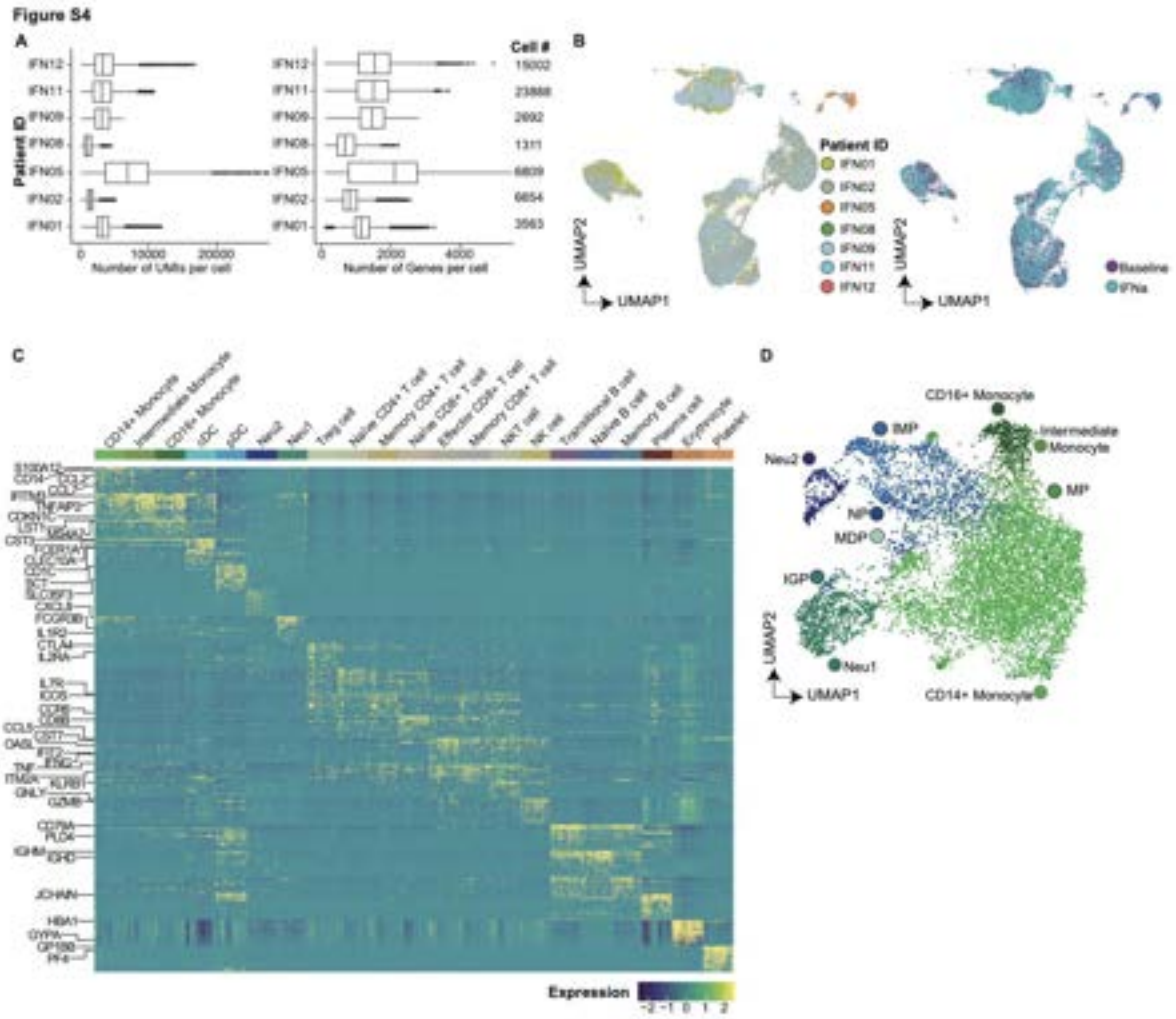

Fig. S4 (related to Fig. 2): Genotyping of Transcriptomes integrated with immunophenotyping (GoT-IM) profiles thousands of CD34⁻ cells at baseline and following treatment with IFNα. A. Box plots showing number of UMIs (left panel), and genes (right panel) detected per cell in sorted CD34⁻ mature immune cells from each patient after filtering based on quality control (QC) metrics (**methods**). **B.** UMAP of sorted CD34⁻ immune cells (n = 59,912 cells) highlighted by patient ID (n = 7 individuals, left) and treatment status (right) after integration. **C.** Heatmap of top 15 differentially expressed genes for each immune cell type. Cells from each group was down-sampled to the same number (n = 75 cells per cluster) for visualization. **D.** Integrated UMAP of sorted CD34⁺ progenitors and CD34⁻ mature immune cells from representative samples (n = 4 individuals, IFN09-IFN12) highlighted by cell type assignment.

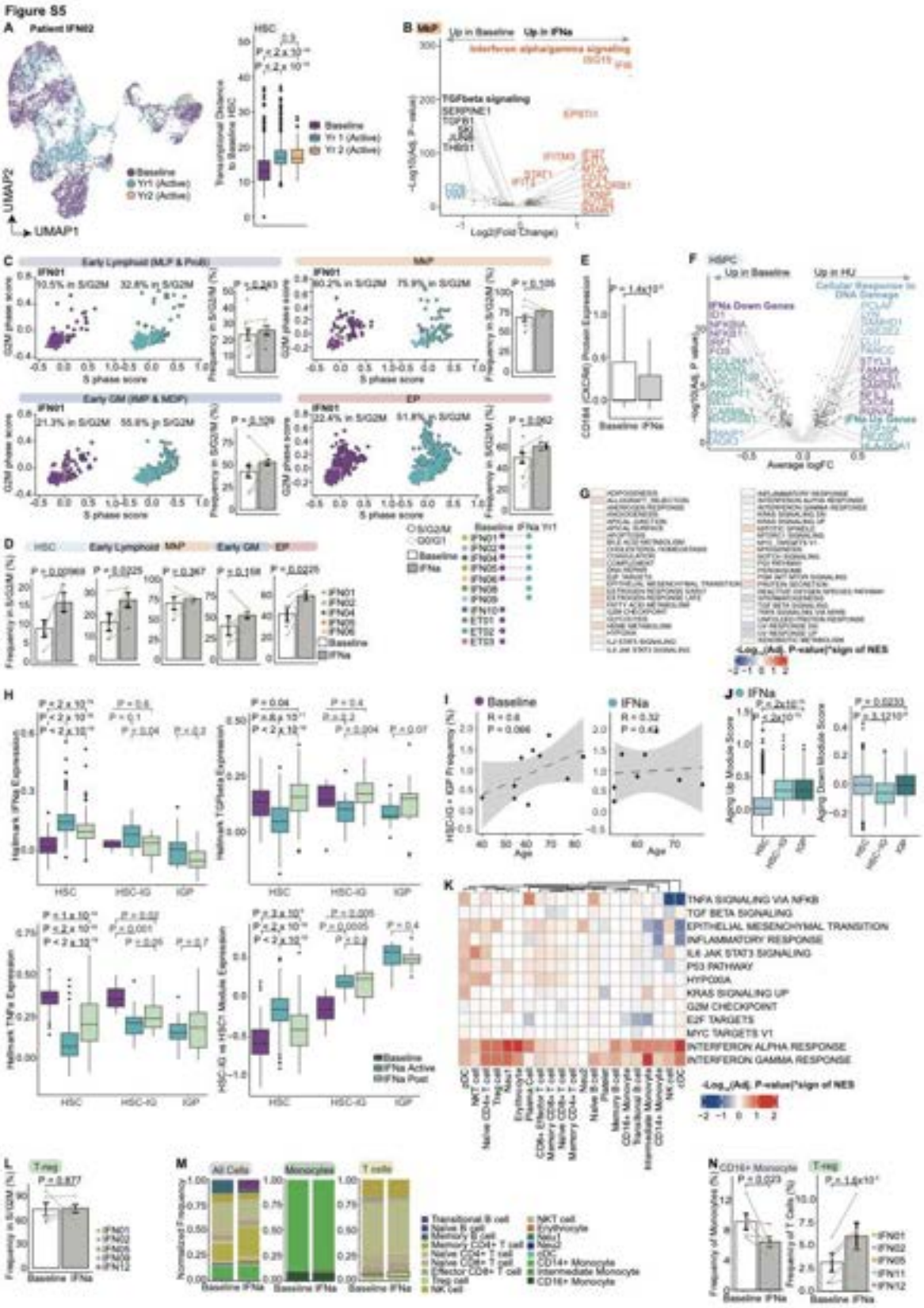

1881 **Fig. S5 (related to Fig. 3). IFNα induces HSC cell cycle entry. A.** UMAP of CD34^{+} cells from

1882 patient IFN02 highlighting treatment status (n = 4,326 baseline cells, 2,912 IFNα-treated cells at
1883 year 1 and 541 IFNα-treated cells at year 2, left). Box plot showing transcriptional distance
1884 measurements between HSCs from each time-point and HSCs at baseline (right). Transcriptional
1885 distance corresponds to Euclidean distance of the first thirty principal components. P-values from
1886 Wilcoxon rank sum test, two-sided. **B.** Volcano plot showing differentially expressed genes
1887 between baseline and IFNα-treated MkPs. P-values from likelihood ratio test of linear mixed
1888 modeling (LMM) with/without treatment status (**methods**). Genes in black are enriched in the
1889 TGFβ signaling and those in orange enriched in the IFNα/γ response. Enrichment is based on pre-
1890 ranked gene set enrichment analysis (GSEA) using the MSigDB Hallmark collection. **C.** Cell cycle
1891 status of progenitor cells. For each cell type, left subpanel: Cell cycle gene expression in progenitor
1892 cells (representative patient IFN01, see **table S2** for cell numbers). Right subpanel: Frequencies
1893 of cells in G2/M/S phase as assessed in left subpanel (n = 11 baseline and 9 treated samples). P-
1894 values were derived from likelihood ratio test of LMM with/without treatment status. **D.**
1895 Frequencies of cells in G2/M/S phase in HSCs and progenitor cells at baseline and upon IFNα
1896 treatment (n = 12 paired samples from 6 individuals). P-values were derived from likelihood ratio
1897 test of LMM with/without treatment status. **E.** *CXCR4* (CD184) protein expression in stem and
1898 early progenitor subsets (HSCs, IMPs, MLPs, MEPs and MDPs) at baseline and under IFNα
1899 treatment. P value from likelihood ratio test LMM with/without treatment status. **F.** Volcano plot
1900 showing DE genes between baseline and HU treated HSPCs highlighting genes in cellular response
1901 to DNA damage (light-blue) the MSigDB GOBP collection, IFNα^{UP} genes (teal) and IFNα^{DN}
1902 genes (purple) from. P-values from likelihood ratio test of LMM with/without treatment status. **G.**
1903 Heatmap showing results of the pre-ranked gene set enrichment analysis comparing baseline and
1904 HU treated HSPCs. Values show the sign of the normalized enrichment score (NES) multiplied by
1905 -log10(Adjusted P-value). **H.** Gene expression of IFNα response signature, TGFβ pathway and
1906 TNFα signaling from the MSigDB Hallmark collection and HSC-IG vs HSC1 (**Fig. 1G**) signature
1907 at baseline, during and post-IFNα-treatment in HSCs (HSC1 and HSC2 subclusters from **Fig. 1G**),
1908 HSC-IGs and IGPs from a representative sample IFN05. **I.** Scatterplot showing correlation
1909 between patients' age and their normalized HSC-IG and IGP frequency at baseline (left) and upon
1910 IFNα treatment (right). **J.** Boxplots showing module gene expression of previously identified
1911 aging-specific upregulated genes (left) and downregulated (right) genes (*56*) in IFNα-treated HSCs
1912 (HSC1 and HSC2 subsets from **Fig. 1G**), HSC-IGs and IGPs. P-values from likelihood ratio test
1913 of LMM with/without cluster identity (**methods**). (*56*) in IFNα-treated HSCs (HSC1 and HSC2
1914 subsets from **Fig. 1G**), HSC-IGs and IGPs. P-values from likelihood ratio test of LMM
1915 with/without cluster identity (**methods**). **K.** Heatmap showing results of the pre-ranked gene set
1916 enrichment analysis comparing baseline and during IFNα treatment across CD34$^-$ mature cells.
1917 Values show the sign of the normalized enrichment score (NES) multiplied by -log10(Adjusted P-
1918 value). **L.** Frequency of regulatory T cells in G2/M/S phase as assessed based on cell cycle gene
1919 expression at baseline and upon IFNα treatment. P-values were derived from likelihood ratio test
1920 of LMM with/without treatment status. **M.** Normalized frequency of cell types within all CD34$^-$
1921 mature immune cells (left), monocytes (middle) and T cells (right) at baseline and active IFNα
1922 treatment. Cells from each treatment status and individual were down-sampled to the same number
1923 (n = 500 cells per treatment status per sample, 10 baseline and IFNα-treated paired samples from
1924 5 individuals). For IFN02 and IFN05, treated time-point powered with greater number of cells was
1925 selected. **N.** Normalized frequency of CD16$^+$ monocytes and regulatory T (Treg) cells at baseline
1926 and upon IFNα treatment (n = 10 samples from 5 individuals). For IFN02 and IFN05, the treated

1927 time-point powered with greater number of cells was selected. P-values from likelihood ratio test
1928 of LMM with/without treatment status.
1929

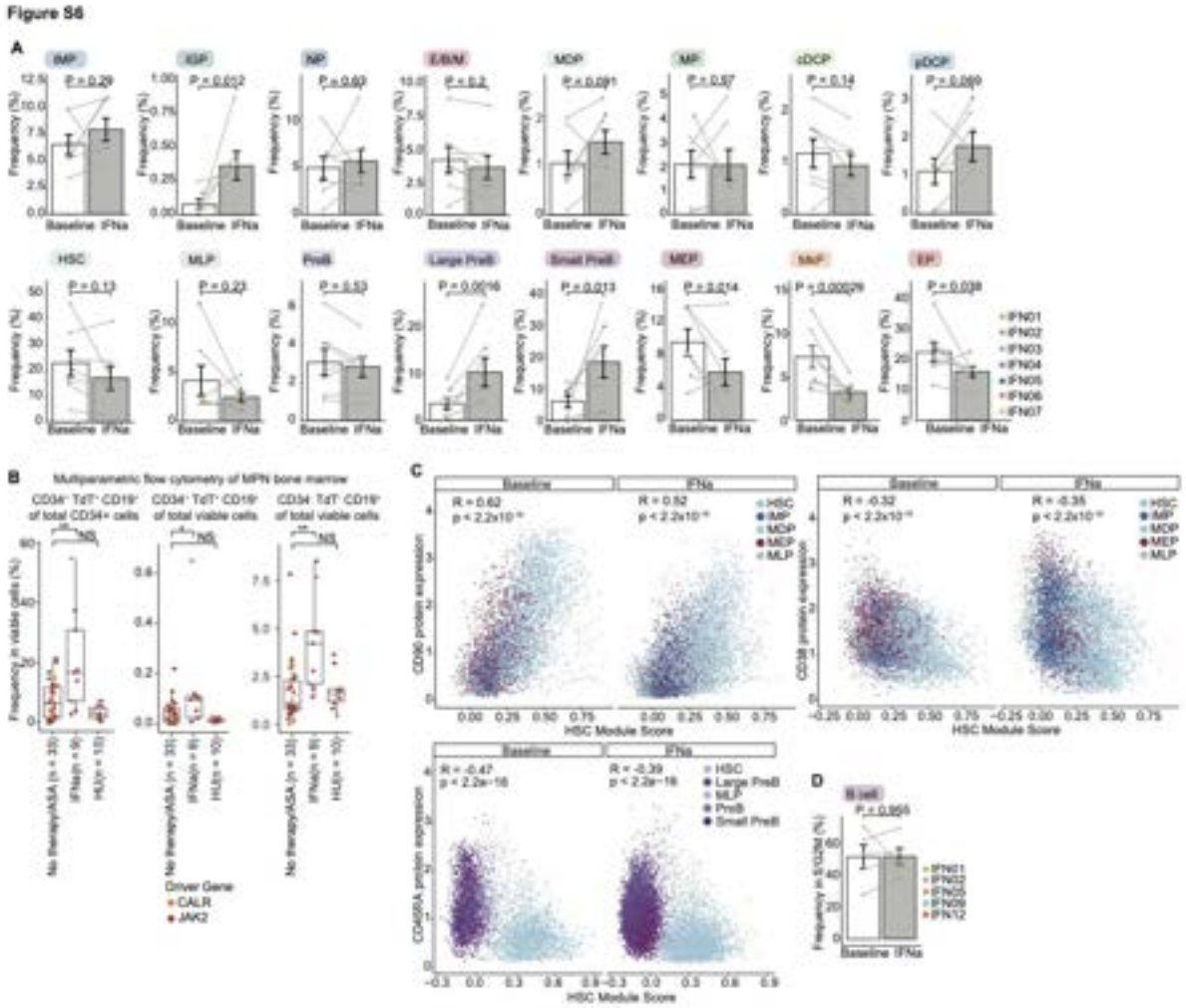

Fig. S6 (related to Fig. 4). IFNα induces lymphoid differentiation. A. Bar plot showing normalized cell type frequencies at baseline and during IFNα treatment (n = 14 paired samples from 7 individuals). For IFN02, IFN04 and IFN05, the time-point powered with greater number of cells was selected. P-values from likelihood ratio test of linear-mixed modeling (LMM) with/without treatment status (**methods**). **B.** Box plots showing cell frequencies of B-lymphoid progenitors and B cells from bone marrow of patients with early stage MPN treated with IFNα and HU treatment (n = 9 and 10 respectively) and without treatment (n = 33 samples), as determined by multiparametric flow cytometry. P-values from Wilcoxon rank sum test, two-sided. **C.** Scatter plot showing correlation between HSC module expression (based on differentially expressed genes in HSC cluster, **fig. S2A**) and protein expression of canonical stem/progenitor markers i.e., CD90 (top-left), CD38 (top-right) and CD45RA (bottom) in stem and progenitor subsets. P-value from F-test, Pearson correlation. Shading denotes 95% confidence interval. **D.** Frequency of B cells in G2/M/S phase as assessed based on cell cycle gene expression at baseline and upon IFNα treatment. P-values were derived from likelihood ratio test of LMM with/without treatment status.

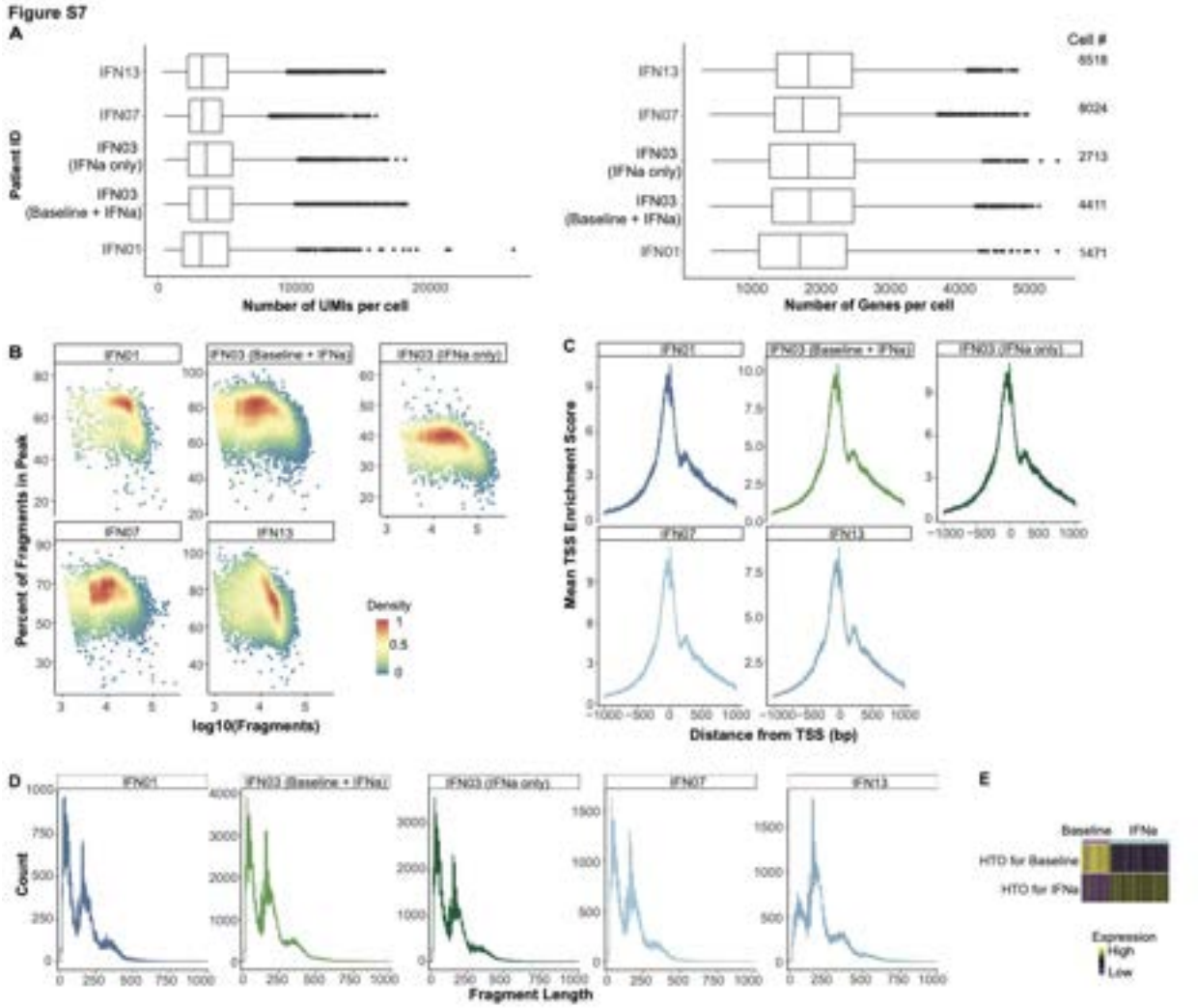

Fig. S7 (related to Fig. 5). GoT-ATAC captures genotyping, snRNA-seq and snATAC-seq data for CD34$^+$ HSPCs. A. Box plots showing number of UMIs (left) and genes (right) detected per cell in sorted CD34$^+$ hematopoietic stem and progenitors from each patient after filtering based on quality control (QC) metrics (**methods**) from GoT-ATAC experiments. **B.** Density plot comparing percentage of snATAC fragments within peaks to the total number of fragments detected per sample (n = 7 samples from 4 individuals, additional IFN03 IFNα-treated cells also sequenced separately). **C.** Distribution of mean TSS enrichment score at each position relative to the TSS per sample. **D.** Average distribution of fragment length per sample. **E.** Heatmap showing HTO expression level for baseline and IFNα-treated cells from representative IFN01 (n = 1471 cells).

Figure S8

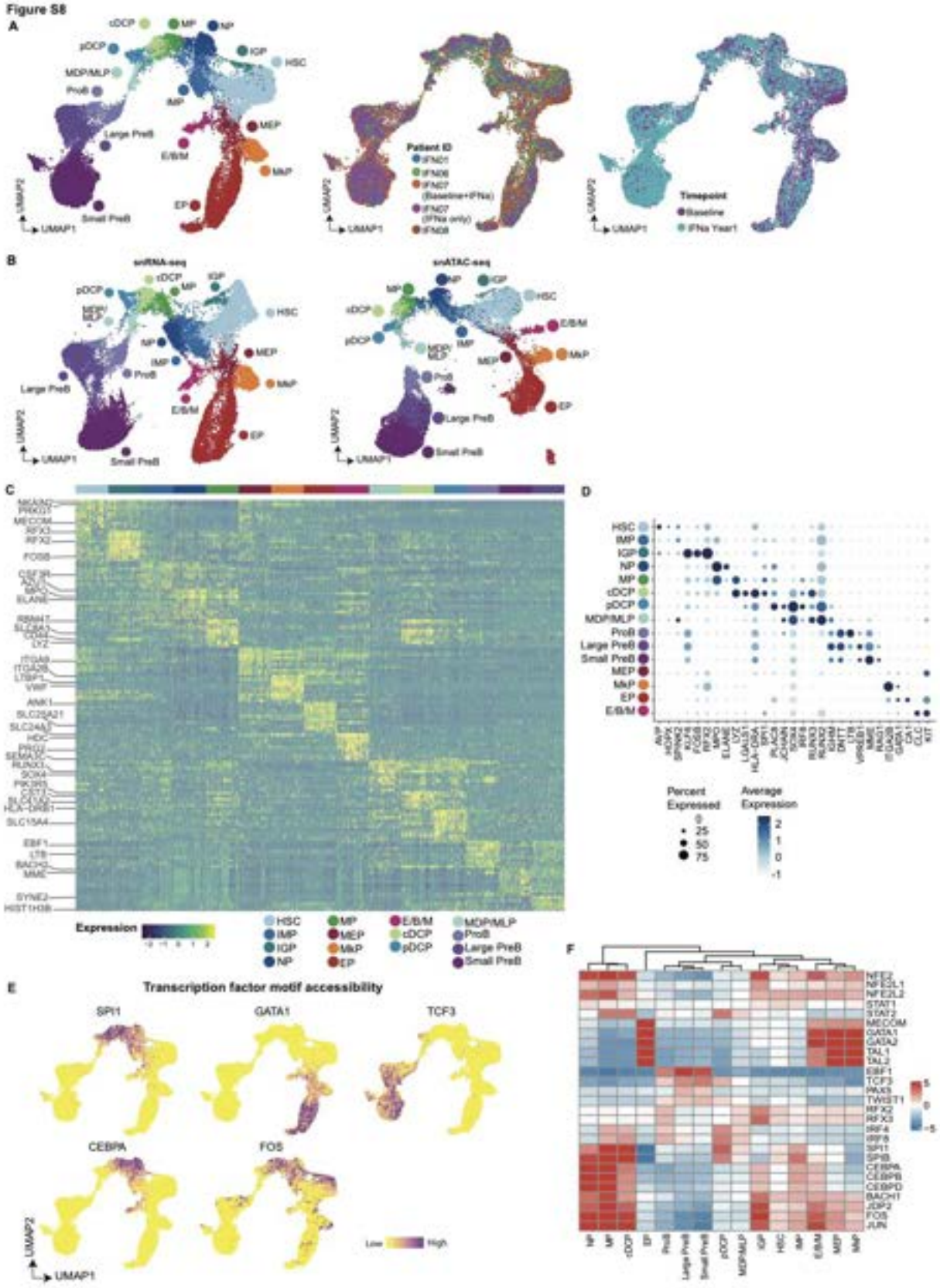

1959

1960 **Fig. S8 (related to Fig. 5). GoT-ATAC identifies the novel inflammatory granulocytic**
1961 **progenitor population. A.** UMAP of sorted $CD34^+$ stem and progenitors (n = 23,137 cells, 7
1962 samples from 4 individuals), with cell type (left), patient ID (middle) and treatment status (right)
1963 using weighted-nearest neighbor (WNN) analysis of snRNA-seq and snATAC-seq data
1964 (**methods**). **B.** UMAP of $CD34^+$ cells based on snRNA-seq (left) and snATAC-seq (right) data,
1965 overlaid with cell type assignment. **C.** Heatmap of top 15 differentially expressed genes for each
1966 HSPC type. Cells of each progenitor type were down-sampled to the same number (n = 100 cells
1967 per cluster). **D.** Dot plot showing expression levels of cell type-specific gene markers in each
1968 progenitor subset. **E.** UMAP based on weighted nearest neighbor (WNN) analysis (n = 23,137
1969 cells) highlighting TF motif accessibility. TF accessibility scores added with
1970 AddChromatinModule function in Signac. **F.** Heatmap showing cell type specific TF accessibility
1971 scores.

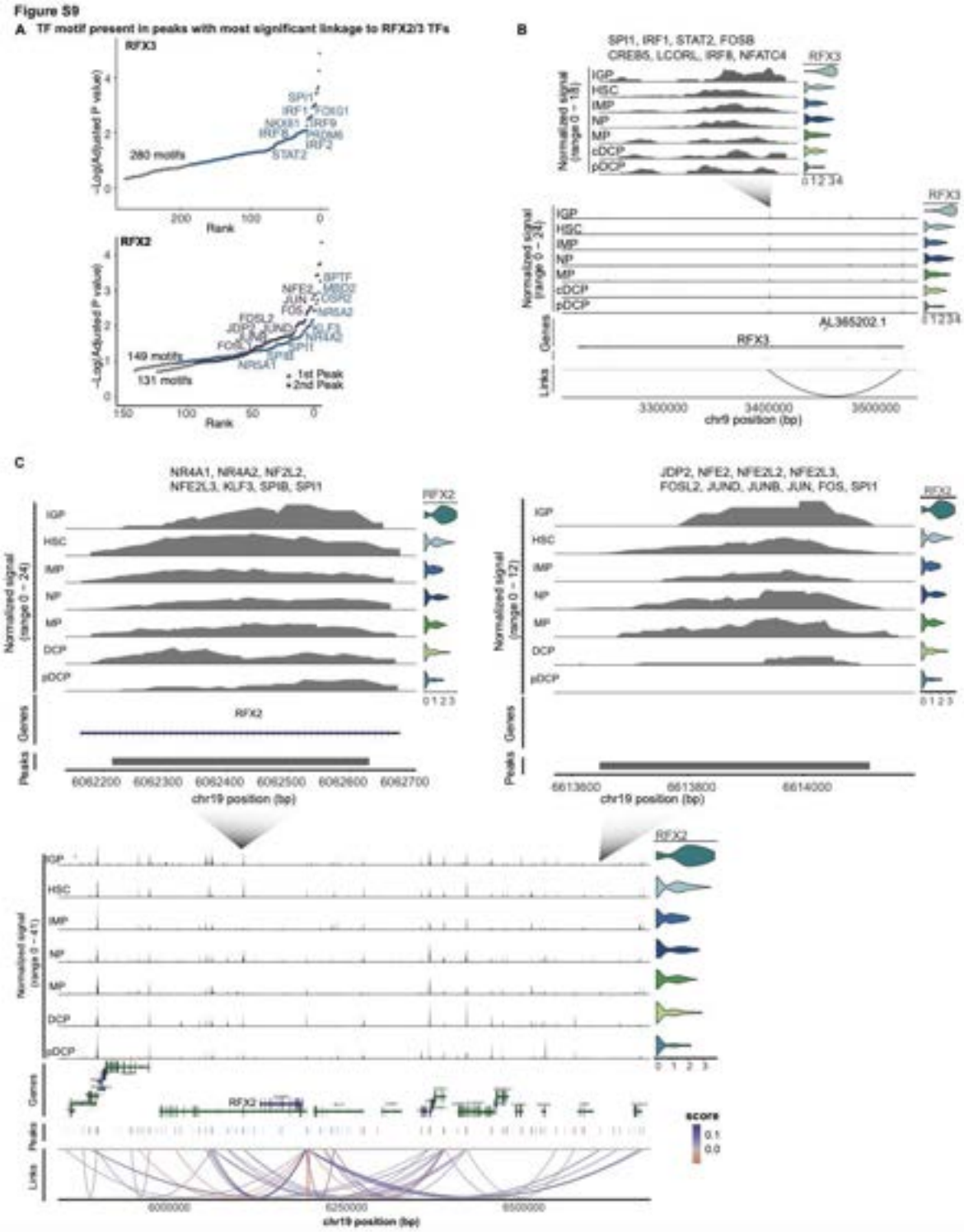

Fig. S9 (related to Fig. 5). Transcription factor activities in inflammatory granulocytic progenitors. A. Ranked transcription factor (TF) motifs in the most significant individual positive regulatory peak of RFX3 (top) and RFX2 (bottom, 1st peak: upstream of TSS, 2nd peak: downstream of TSS) identified using motif scanning with FIMO for a representative sample (IFN03, **methods)**. **B.** Chromatin accessibility track (left) of the regulatory region of *RFX3*

1978 (representative example from IFN03). Violin plots (right) display gene expression level of *RFX3*.
1979 **C.** Chromatin accessibility tracks of regulatory regions of *RFX2* (representative example from
1980 IFN03, bottom) and distal region enriched with the two most significant positively regulating loci
1981 (top-left, top-right). Violin plots display gene expression level of *RFX2*.
1982

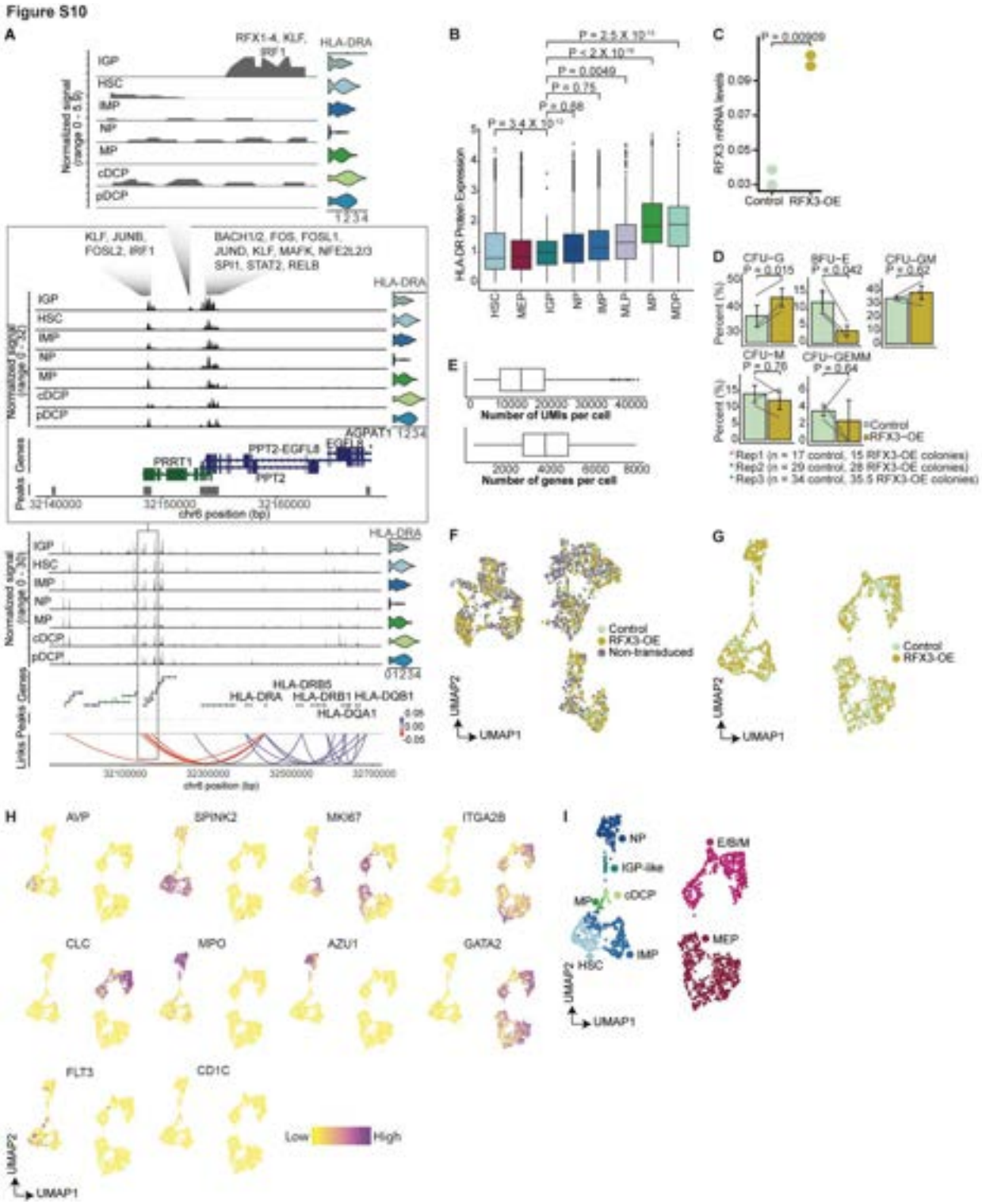

Fig. S10 (related to Fig. 5). RFX3 overexpression induces an IGP-like cell state. A. Chromatin accessibility tracks of regulatory regions of *HLA-DRA1* (bottom), distal region enriched with negative regulatory loci (inset), and IGP-specific regulatory locus (top, representative example

1989 from IFN07). Violin plots display gene expression level of *HLA-DRA1*. **B.** Box plots showing
1990 normalized expression of HLA-DR protein expression. P-values from likelihood ratio tests of
1991 linear-mixed modeling (LMM) with/without cell type identity. **C.** RFX3 overexpression lentiviral
1992 vector validated in K562 cells by assessing *RFX3* mRNA levels by RT-QPCR (n = 2 independent
1993 experiments). mRNA levels correspond to RFX3 Ct values normalized to TBP Ct values. P-value
1994 from t-test. **D.** Normalized frequency of erythroid (BFU-E), granulocytic (CFU-G), granulo-
1995 monocytic (CFU-GM), monocytic (CFU-M) and myeloid (CFU-GEMM) colonies grown from
1996 RFX3-OE $CD34^+$ umbilical cord blood (UCB) cells in methylcellulose-based CFU assays
1997 compared to control $CD34^+$ UCB cells. P-value from likelihood ratio test linear-mixed modeling
1998 (LMM) with/without RFX3 overexpression. **E.** Box plots showing number of UMIs (top) and
1999 genes (bottom) detected per cell in sorted $CD34^+$ UCB cells after filtering based on quality control
2000 (QC) metrics (**methods**) from GoT-IM experiments. **F.** UMAP of sorted $CD34^+$ UCB cells (n =
2001 2,609 cells) highlighted by three transduction statuses. **G.** UMAP of RFX3-OE and mCherry
2002 (control) subsets (n = 1,520 cells) highlighted by their status. **H.** UMAP of RFX3-OE and control
2003 subset showing gene expression levels of cell type specific gene markers for HSPCs. **I.** UMAP of
2004 RFX3-OE and control subset, highlighting cell type assignments.
2005

Figure S11

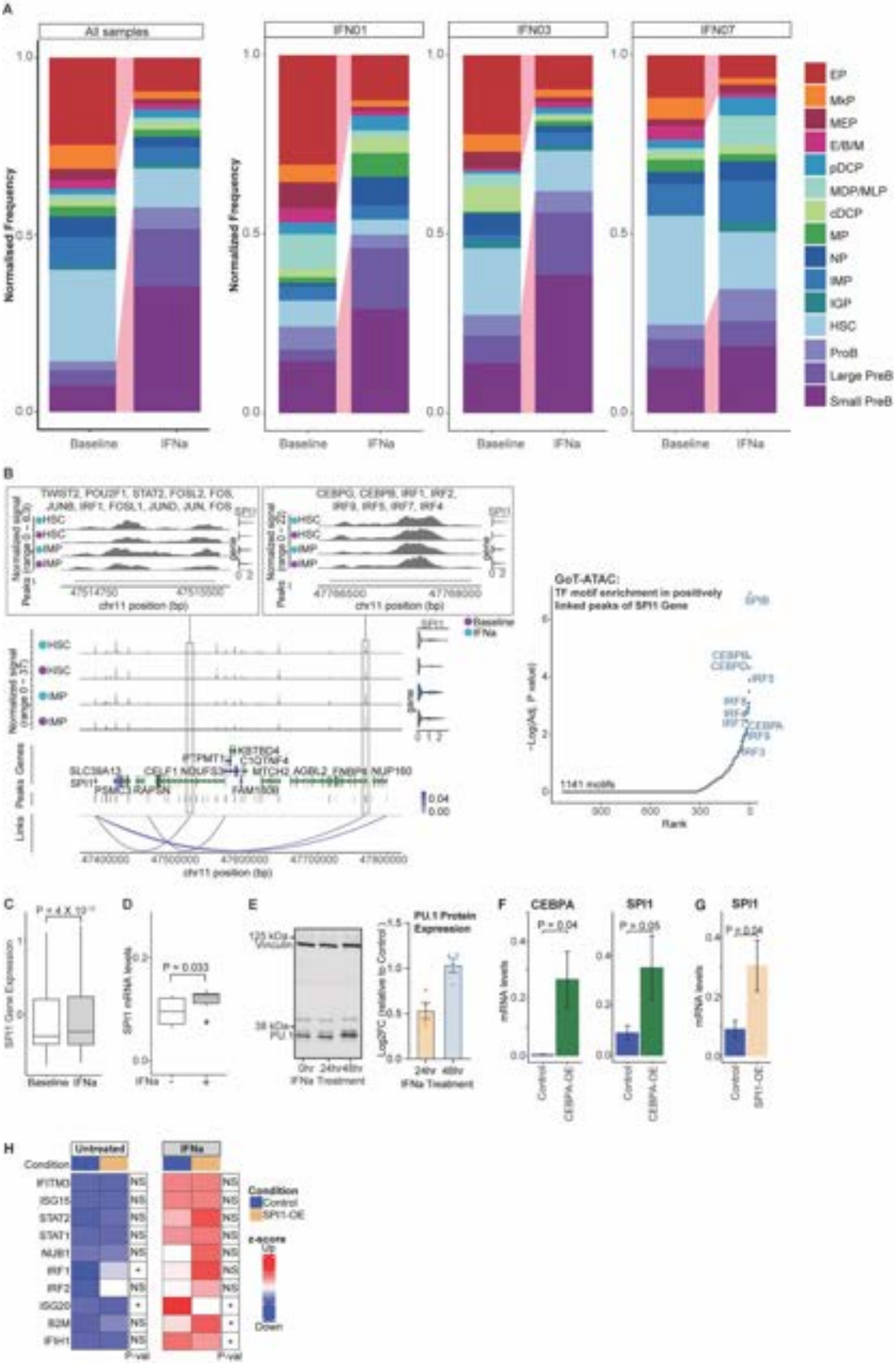

2006

2007 **Fig. S11 (related to Fig. 5). PU.1 is the master regulator of IFNα-mediated lymphoid**
2008 **differentiation and remodeling of hematopoiesis. A.** Left: Normalized cell frequencies of
2009 progenitor subsets at baseline and after IFNα treatment from all GoT-ATAC samples (n = 4
2010 individuals). Cells from each treatment status and individual were down-sampled to the same
2011 number (n = 100 cells per treatment status per sample). Right: Cell frequency distribution as in left
2012 panel for patients IFN01, IFN03 and IFN07. **B.** Chromatin accessibility tracks of regulatory
2013 regions of *SPI1* (representative example from IFN07, bottom-left), distal region enriched with the
2014 two most significant positively regulating loci (top-left). Violin plots display gene expression level
2015 of *SPI1*. Ranked TF motif enrichment of all positive regulatory peaks of the SPI1 gene, relative to
2016 background peaks using the hypergeometric test across three samples IFN01, IFN03 and IFN07
2017 (right, see **methods**). **C.** SPI1 gene expression in stem and early progenitors (HSCs, IMPs, MLPs,
2018 MEPs and MDPs) at baseline and upon IFNα treatment. P-value from likelihood ratio test linear-
2019 mixed modeling (LMM) with/without treatment status. **D.** *SPI1* mRNA levels in K562 cells treated
2020 with IFNα *in vitro* for 24 hours (assessed by RT-QPCR, n=6 independent experiments). mRNA
2021 levels correspond to SPI1 Ct values normalized to TBP Ct values. P-values from likelihood ratio
2022 test of LMM with/without treatment status. **E.** Representative western blot showing PU.1 protein
2023 levels in K562 cells treated with IFNα *in vitro* across for 0, 24 and 48 hours with vinculin as
2024 loading control (left). Log-fold change analysis of quantified PU.1 protein levels based on
2025 luminescence intensity of western blot bands across three replicates (right) (**methods**). **F.** *CEBPA*
2026 and *SPI1* mRNA levels in K562 cells upon expression of control or CEBPA-OE lentiviral vectors
2027 (assessed by RT-QPCR, n=3 independent experiments). mRNA levels correspond to Ct values of
2028 gene target normalized to TBP Ct values ($2^{-\Delta\Delta Ct}$). P-values from likelihood ratio test of LMM
2029 with/without CEBPA overexpression. **G.** *SPI1* mRNA levels in K562 cells upon expression of
2030 control or SPI1-OE lentiviral vectors (assessed by RT-QPCR, n=2-3 independent experiments).
2031 mRNA levels correspond to Ct values of gene target normalized to TBP Ct values ($2^{-\Delta Ct}$). P-values
2032 from likelihood ratio test of LMM with/without SPI1overexpression. **H.** Heatmap depicting scaled
2033 mRNA levels($2^{-\Delta Ct}$) of IFN-related genes in K562 cells upon expression of control or SPI1-OE
2034 lentiviral vectors at baseline and after 24-hour IFNα treatment (assessed by RT-QPCR, n = 4-7
2035 independent experiments). Scaled across all data points for each gene. P-values from likelihood
2036 ratio tests of LMM with/without SPI1 overexpression status.
2037

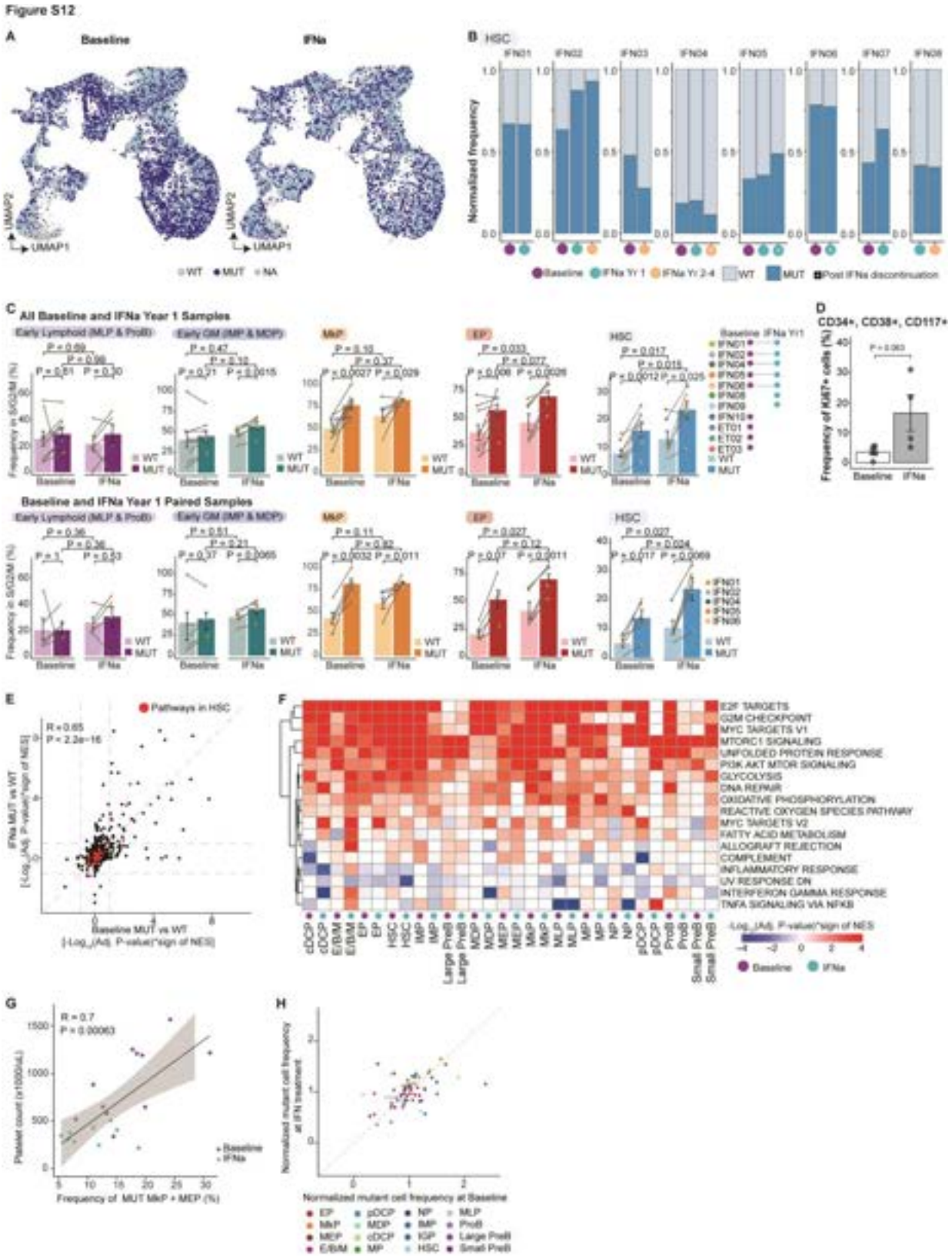

Fig. S12 (related to Fig. 6). *CALR* mutations modify the effects of IFNα signaling. A. UMAP of sorted CD34^{+} stem and progenitors at baseline and after IFNα treatment from GoT-IM

2041 experiments with *CALR* mutation status highlighted. Cells from each sample were down-sampled
2042 to the same number for each mutation status (n = 1,000 cells from each mutation status per sample).
2043 **B.** Normalized frequencies of CALR-mutated (MUT) and wildtype (WT) HSCs at each time-point
2044 (n= 8 individuals with at least 2 time-points). **C.** Bar plots showing frequencies of MUT and WT
2045 cells in G2/M/S phase as assessed in **Fig. 3C** for all $CD34^+$ GoT-IM samples (n = 11 baseline and
2046 9 IFNα year 1 samples, top) and paired $CD34^+$ GoT-IM samples (n = 12 samples from 6
2047 individuals, bottom). P-values were derived from likelihood ratio test of linear mixed modeling
2048 (LMM) with/without treatment status. **D.** Frequencies of $Ki67^+$ myeloid cells before and after
2049 IFNα treatment. P-values from Wilcoxon rank sum test, two-sided. **E.** Scatter plot showing
2050 pathways from pre-ranked DE gene set enrichment analysis comparing mutated (MUT) versus
2051 wildtype (WT) cells at baseline and after IFNα treatment. Values show the sign of the normalized
2052 enrichment score (NES) multiplied by -log10(Adjusted P-value). Pathways in red are present in
2053 HSCs. P-value from F-test, Pearson correlation. Shading denotes 95% confidence interval. **F.**
2054 Heatmap showing results of the pre-ranked gene set enrichment analysis of genes DE between
2055 MUT and WT cells at baseline and after IFNα treatment. **G.** Platelet counts versus frequencies of
2056 MUT MEPs and MkPs. P-value from F-test, Pearson correlation. Shading denotes 95% confidence
2057 interval. **H.** Normalized mutant cell frequency at baseline versus after IFNα treatment for GoT-
2058 IM $CD34^+$ samples (cell type clusters with at least 10 genotyped cells were within each sample
2059 were used).
2060

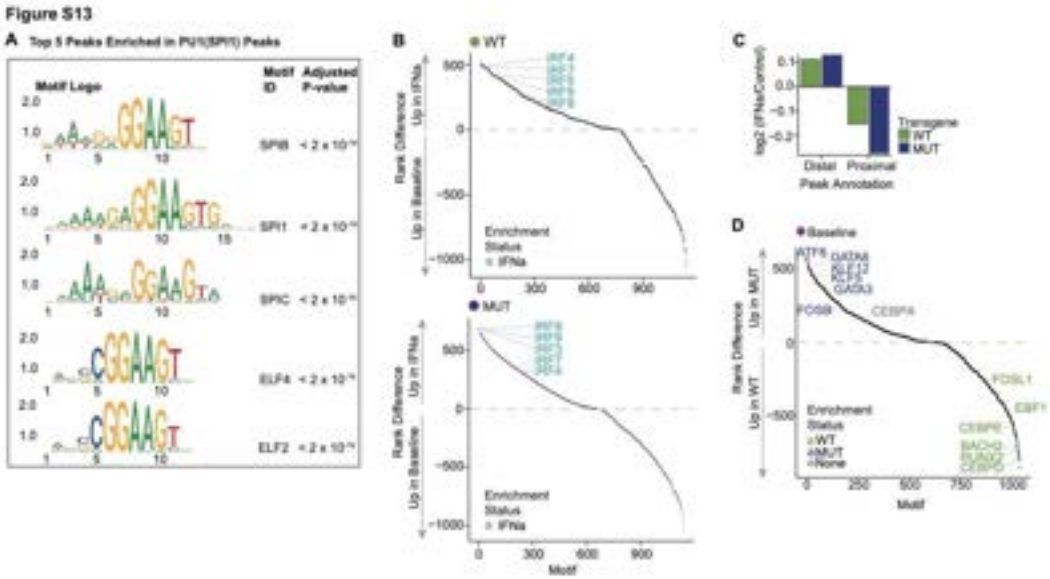

Fig. S13 (related to Fig. 6). *CALR* mutated cells display enhanced PU.1 binding activity at regulatory regions with distinct cooperating TF binding sites. A. Top five hits from Ranked transcription factor (TF) motif enrichment of peaks captured from CUT&RUN targeting PU.1 motif with SEA v5.5.5. **B.** Differential TF motif enrichment between baseline and IFNα-treated focusing on exclusive PU.1 peaks in WT (top) and MUT cells (bottom). Analyses with HOMER. Highlighted are IRF TFs (blue). **C.** Bar plot showing difference in the number of distal and proximal PU.1 peaks between control and IFNα-treated UT7-MPL cells. Peaks less than 500 bp from TSS were considered proximal. **D.** Differential TF motif enrichment between MUT and WT exclusive PU.1 peaks in baseline cells. TFs enriched in differentially accessible PU.1 peaks for MUT and WT cells are highlighted in blue and green respectively.

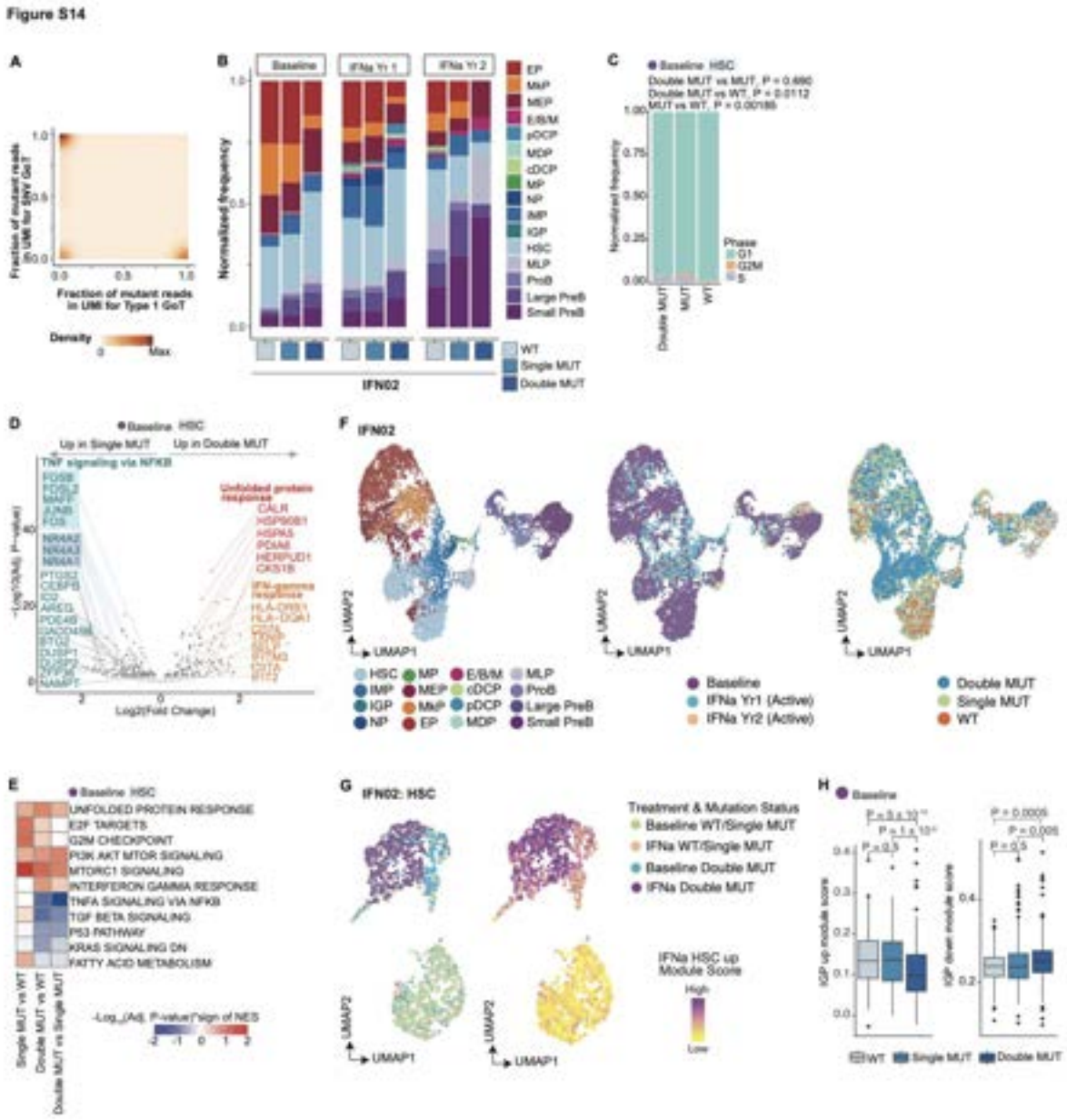

Fig. S14 (related to Fig. 6). IFNα perturbs clonal evolution via the IGP differentiation program. A. Relative density of proportion of Type 1-mutant reads versus SNV-mutant reads in UMIs captured via GoT, showing mutual exclusivity. **B.** Normalized frequencies of each progenitor subset among WT, single MUT (Type 1 *CALR*) and double MUT (Type 1 and SNV mutations in *CALR*) cell populations at each time-point for IFN02 (n = 7,779 cells). **C.** Bar plots showing normalized frequency of baseline HSCs in G1/G2/M/S phases as assessed in **Fig. 3C**. P-values from Fisher's exact test between mutation status and cell-cycle entry status (G2/M/S vs G1). **D.** Volcano plot showing genes differentially expressed (DE) between single mutant and double mutant HSCs at baseline (n = 890 genotyped HSCs). DE genes identified using logistic regression model (**methods**). Genes highlighted in blue are enriched in the TNFα signaling via NF-κB, red in the unfolded protein response, and orange in the IFNγ response (box representation

2088 is same as **Fig. 1E)**. **E.** Heatmap showing results of the pre-ranked gene set enrichment analysis
2089 of genes DE between HSC clones at baseline. Values correspond to the sign of the normalized
2090 enrichment score (NES) multiplied by the -log10(Adjusted P-value)**. F.** UMAP of IFN02 patient
2091 based on scRNA-seq data highlighting cell types (left), treatment status (middle) and mutation
2092 status (right). **G.** UMAP of HSCs from IFN02 (n = 1,879 cells) overlaid with treatment status and
2093 HSC clones (left) and module score for HSC-specific IFNα-induced upregulated genes (right). **H.**
2094 Box plots showing IGP-specific signature score in HSC clones at baseline in IFN02. Scores
2095 calculated using IGP-upregulated or downregulated genes (left and right panels, respectively,
2096 **methods**). P-values from Wilcoxon rank sum test, two-sided.
2097

2098 **Supplementary Tables**
2099

2100 **Table S1.** Summary of patients' clinical history, pathology and laboratory data, and mutation
2101 status.
2102 **Table S2.** Number of cells for each cell type in GoT-IM $CD34^+$ compartment.
2103 **Table S3.** Differential gene expression analyses for IGP versus IMP and treated IGP versus treated
2104 HSC1 via the linear mixed modeling framework.
2105 **Table S4.** Gene set enrichment analysis of genes differentially expressed between IGPs versus
2106 IMPs and treated IGPs versus treated HSC-IG.
2107 **Table S5.** RNA velocity analysis with scVelo between HSPC subpopulations. Cluster-to-cluster
2108 transition and connectivity scores calculated based on velocity graph based on pseudotime values.
2109 **Table S6.** Number of cells for each cell type in GoT-IM $CD34^-$ compartment.
2110 **Table S7.** Differential gene expression analyses for Neu1 versus Neu2 subsets via the linear mixed
2111 modeling framework. Gene set enrichment analysis of genes differentially expressed between
2112 Neu1 versus Neu2 subsets.
2113 **Table S8.** Differential gene expression analysis between baseline and IFNα-treated HSPC subsets.
2114 **Table S9.** Gene set enrichment analysis of genes differentially expressed between baseline and
2115 IFNα-treated HSPC subtypes.
2116 **Table S10.** Differential gene expression analysis between baseline and IFNα-treated $CD34^-$
2117 mature cells subsets.
2118 **Table S11.** Gene set enrichment analysis of genes differentially expressed between baseline and
2119 IFNα-treated $CD34^-$ mature cells subsets.
2120 **Table S12.** Clinical data multi-parametric flow cytometry data of bone marrow aspirates from
2121 patients with early-phase MPN with IFNα/HU and without treatment.
2122 **Table S13.** Number of cells identified for each cell type in each sample via GoT-ATAC.
2123 **Table S14.** Differential transcription factor motif enrichment analysis between IGPs and HSCs
2124 under IFNα treatment.
2125 **Table S15.** Motifs identified in peaks linked with RFX2/3 via motif scanning with FIMO.
2126 **Table S16.** Over-enrichment motif analysis for peaks linked with AP-1 genes and SPI1 gene.
2127 **Table S17.** Motifs identified in peaks linked with MHC class II genes.
2128 **Table S18.** Genes positively regulated by RFX2 and RFX3 using gene-peak cis-association.

2129 **Table S19.** Differential gene expression analyses for IGP-like vs IMP subsets in $CD34^+$ cells with
2130 RFX3 overexpression. Gene set enrichment analysis of genes differentially expressed between
2131 IGP-like vs IMP subsets.
2132 **Table S20.** Differential transcription factor motif enrichment analysis between baseline and IFNα-
2133 treated HSCs.
2134 **Table S21.** Differential gene expression analysis between *CALR*-mutated and wildtype cells at
2135 baseline in HSPC subsets.
2136 **Table S22.** Gene set enrichment analysis of genes differentially expressed between *CALR*-mutated
2137 and wildtype cells at baseline in HSPC subsets.
2138 **Table S23.** Differential gene expression analysis between *CALR*-mutated and wildtype cells after
2139 IFNα treatment in HSPC subsets.
2140 **Table S24.** Gene set enrichment analysis of genes differentially expressed between *CALR*-mutated
2141 and wildtype cells after IFNα treatment in HSPC subsets.
2142 **Table S25.** Differential transcription factor motif enrichment analysis between MUT vs WT stem
2143 and early progenitor cells at baseline and upon IFNα treatment.
2144 **Table S26.** Motifs identified in PU.1 bound peaks captured from CUT&RUN data of CALR-
2145 mutated versus WT UT-7 cells.
2146 **Table S27.** Differential TF motif enrichment in MUT and WT exclusive PU.1 peaks at baseline
2147 and upon IFNα treatment.
2148 **Table S28.** Differential TF motif enrichment in IFNα and Baseline exclusive PU.1 peaks for MUT
2149 and for WT.
2150 **Table S29.** Differential gene expression analysis between HSC clones from IFN02 at baseline.
2151 **Table S30.** Gene set enrichment analysis of genes differentially expressed between HSC clones
2152 from IFN02.
2153 **Table S31.** List of antibodies used for FACS, CITE-seq, and Cell Hashing and primer sequences
2154 used in GoT-IM, GoT-ATAC, and RT-PCR.